國立臺灣大學工學院應用力學研究所
博士論文
Graduate Institute of Applied Mechanics
College of Engineering
National Taiwan University
doctoral dissertation

矽鍺錫量子井雷射及電致吸收光調變器
SiGeSn-based Quantum-Well Lasers and Electroabsorption Modulators

張國恩
Guo-En Chang

指導教授：張家歐 博士
莊順連 博士
Advisor: Chia-Ou Chang, Ph.D.
Shun Lien Chuang, Ph.D.

中華民國 九十九年 六月
June, 2010

致謝

首先，我要感謝我的恩師，台灣大學應用力學所 張家歐教授，以及伊利諾大學香檳分校電機與電腦工程學系 莊順連教授。我很幸運能有二位論文指導教授，讓我能得到的比別人多更多。恩師在學術的殿堂中的諄諄教誨讓我體會對於學術研究該有的嚴謹，以及身為學者該有的熱忱及風骨，字字句句教導有如金玉良言，永銘於心。此外，在為人處事上更是常常提醒，教導及指正。恩師的身教及言教，讓身為學生的我，不但終生受用不盡，更是我永遠的楷模與典範

口試期間，承蒙本所 陳瑞琳教授，以及本校光電所 楊志忠教授，電子所 鄭鴻祥教授，材料所 陳敏璋教授，以及交通大學光電所 余沛慈教授於百忙之中撥空指導，並給予許多寶貴意見及建議，使得本文更加完備，僅致以誠摯之謝意。

此外感謝台大應力所動力實驗室的歷屆成員在我研究所求學期間的協助以及合作。也要感謝在伊利諾大學香檳分校莊順連教授的研究團隊在我參訪期間的幫助及建議。特別要感謝 張書維博士在我訪問伊利諾大學期間給予的建議及指導，張博士對學術研究的嚴謹態度，廣博的學問，以及樂於助人的心對初到伊利諾大學的我助益良多。也要感謝台大應力所籃球隊以及在伊利諾大學的球友們，課餘之時在籃球場上揮汗的時光更是我生命中珍貴的記憶。

最後感謝我的家人對我持續不斷的關心及付出，使我在研究所求學

期間能夠無後顧之憂，專心致力於課業之上。僅以本文獻給所有幫助過我的人。

國立臺灣大學
敦品・勵學・愛國・愛人

Acknowledgments

First and foremost, I would like to express my deepest gratitude to my dissertation advisors, Prof. Chia-Ou Chang at National Taiwan University and Prof. Shun Lien Chuang at University of Illinois at Urbana-Champaign, for their constant support and guidance during my graduate years. Their insightful knowledge, encouragement, and patience are very critical for my graduate studies. Besides, they gave lots of freedom to me to study my interesting topics and trained me as an independent researcher.

I would like to thank Prof. Chih-Chung Yang, Prof. Hung-Hsiang Cheng, Prof. Ruey-Lin Chern, and Prof. Miin-Jang Chen at National Taiwan university, and Prof. Peichen Yu at National Chiao Tung University to serve on my final exam committees. Their valuable comments and suggestions are highly appreciated.

I am also grateful to the group members and collaborators in Dynamics Lab at NTU and prof. Chuang's group at University of Illinois. Their many technical discussions with me stimulated many useful and interesting ideas. Especially, I am deeply indebted to thank to Dr. Shu-Wei Chang. He taught me many theories with his insightful knowledge and patience from the vary beginning stage. Besides, his advises and suggestions helped me very much when I am struggled. I would like to thank my friends, especially those play basketball with me in my free time. Those basketball games always make me relax from pressure and are very precious memories to me.

Last but not least, I would like to thank my family for their constant support and unconditional love. Without them, this work is not possible.

中文摘要

光電積體電路可以提供高速，低損耗，晶片型光子網路，可應用於通信系統以及晶片間的訊號傳輸。高性能的矽基雷射及光調變器是其中不可或缺的元件: 雷射用以產生同調性光源，而光調變器用來高速調變信號。 然而，因為矽是間接能隙材料，所以矽的發光效率非常低。再者，矽的線性電光效應以及電致吸收效應也很低，所以很難利用矽來達成高速調變。 所以在實現高性能矽基雷射及光調變器之前，這種高速光電積體電路還無法製作出來。 本文的主旨即在利用新穎的矽鍺錫材料系統來實現矽基雷射及光調變器。

矽鍺錫材料矽統是一種用來發展矽光技術的新平台。 隨著近年來低溫成長磊晶技術的進步，高品質的矽鍺錫合金已經可以合成了。 本文首先研究矽鍺錫材料系統的電子特性，光電特性，以及機械特性來探索這種新材料在光電領域的新應用。

在四族材料之中，鍺是一種可來製作矽基雷射及光調變器的高潛力材料。鍺是一種準直接能隙半導體材料，意味著將鍺變成直接能隙材料的可能性。 本文提出二個利用矽鍺錫材料系統來達成直接能隙材料的方法來增強其發光效率，進而發展矽基雷射: (1)具有張應變及n型摻雜的鍺/矽鍺錫量子井，發光波長在1550奈米附近，以及(2)應力平衡的鍺錫/矽鍺錫量子井，發光波長在中紅外線範圍。我們發展了一套完整理論來分析此二種雷射結構，包括電子能帶結構，載子分布，與極化

有關的光增益，與極化有關的光偈限因子，以及雷射閥值分析。分析的結果顯示我們所設計的雷射結構可以達成雷射輸出。 相對於矽的弱線性電光效應以及光電致吸收效應，鍺具有強健的弗朗茲-凱爾迪什效應以及量子史塔克效應，可用來製作電致吸收光調變器。本文提出及分析二種結構來製作可操作於1550奈米波長的電致吸收量子井光調變器:張應變鍺/矽鍺錫量子井以及無應力鍺錫/矽鍺錫量子井，分析結果顯示此二種結構的調變波長落在常用的1550奈米通訊波長。這些結構對於實現光電積體電路有很大的幫助。

關鍵字*:* 矽光技術，鍺錫合金，矽鍺錫合金，應力量子井雷射， 多重量子井電致吸收光調變器。

Abstract

Compact electronic-photonic integrated circuits are one of the promising technology to enable on-chip, low-power, high-speed optical networks for telecommunications and inter/intra-chip interconnections. High-performance Si-based lasers and modulators are critical to achieve the goal: the former generate coherent light while the later optically encode light signals at the optical transmitter end. However, the light-emitting efficiency in Si is very low due to its indirect bandgap in nature, and fast modulation in Si is challenging because of the lack of efficient linear electro-optical and electroabsorption effects. Thus, high-performance electronic-photonic integrated circuits are not possible until the realization of electrically-pumped Si-based lasers and high-speed modulators. This dissertation focuses on the research of using novel SiGeSn material system for efficient Si-based electrical-pumped lasers and electroabsorption modulators.

SiGeSn material system represents a new promising platform to develop Si photonics. With the significant advances in the growth of SiGeSn material system by low-temperature UHV-CVD, high-quality GeSn, SiSn, and SiGeSn alloys are able to be grown. To explore possible electronic and photonic devices based on the novel SiGeSn material system, we first study the fundamental properties of Si, Ge, and α-Sn as well as their compounds, in-

cluding the electronic, optical, and mechanical properties.

Among the group-IV semiconductors, Ge is a potential material for efficient electrically-pumped Si-based lasers and high-speed modulators. Ge is a quasi direct-bandgap semiconductor, suggesting the possibility of transforming it into a direct bandgap semiconductor for photonic active applications. We propose two approaches to crate direct-bandgap semiconductors based on the SiGeSn material system for developing Si-based lasers: tensile-strained, n-type doped Ge/SiGeSn quantum wells, and strain-balanced GeSn/SiGeSn multiple-quantum-well. We develop a theoretical model for laser analysis, including the strained electronic band structure, carrier occupation, polarization-dependent optical gain, polarization-dependent optical confinement factor, and threshold analysis. Our calculations indicate lasing action in the two designed lasers is possible.

While Si has no linear electro-optical and very weak electroabsorption effects for efficient, high-speed modulators, Ge is suitable for Si-based modulators because it possesses significant Franz-Keldysh and quantum-confined Stark effects. We propose and analyze two structures for electroabsorption waveguide modulators operating at 1550 nm wavelength based on the quantum-confined Stark effect: tensile-strain Ge/SiGeSn quantum wells and strain-free GeSn/SiGeSn quantum wells. A theoretical model for describing the quantum-confined Stark effect is present. With adequate design of the quantum-well materials and waveguide geometry, it is possible to achieve effective modulation at 1550 nm wavelength using the two designed electroabsorption modulators for electronic-photonic integrated circuits.

Keywords: **Si photonics, GeSn alloys, SiGeSn alloys, strained QW lasers, MQW electroabsorption modulators.**

國立臺灣大學

Contents

List of Figures

List of Tables

Chapter 1

Introduction

1.1 Overview of silicon microelectronics and its bottleneck

Since the invention of transistor and integrated circuit, silicon-based electronics has achieved a considerable success and significantly changed human's daily life. In 1965, Gordon Moore predicted that the number of transistors would double every two years. With the rapid developments of photolithography and semiconductor fabrication technologies, the number of transistors in a single chip has grown exponentially from 30 transistors in a device in 1965 to today's ultra-large scale integration circuit (ULSI) containing more than 1 billion of transistors in a small silicon chip with the size as large as fingernails, as shown in Fig. 1.1. However, as the device feature size is able to scale down below 100 nm in recent years, some important issues about the evolution of Si-microelectronics have been raised. One of the most important concerns is the limitation of interconnections for the operating speed of microelectronic devices. Figure 1.2 shows the schematic view of a complementary metal oxide semiconductor (CMOS) chip with its metal interconnections. The metal wires are used to locally or globally connect the CMOS

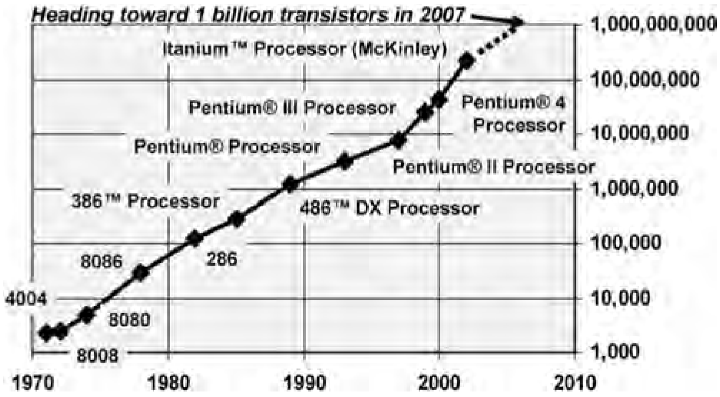

Figure 1.1: Number of transistors in a single CPU as a function of time [1].

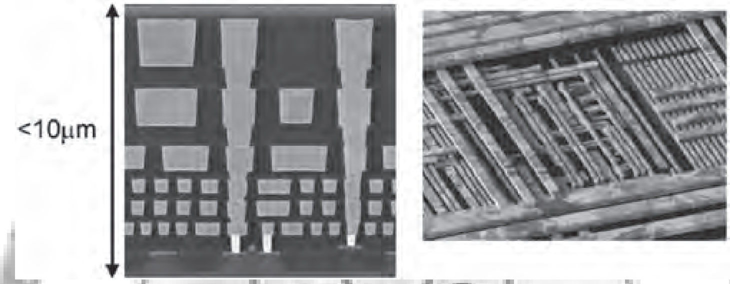

Figure 1.2: Schematic structure of the back-end structure for electrical interconnections [1].

devices at different levels, and their propagation speed is mainly limited by RC delays. However, as the device feature size scales down, the reduced dimension of metal wires significantly increases the resistance R as well as the RC delay, and the gain of propagation speed from size reduction is becoming less and less. Figure 1.3 shows the calculated gate and wire delays as a function of device feature size for the current Al/SiO$_2$ and Cu/low-dielectric-material electrical interconnections [1]. Clearly, while the gate delay decreases with the shorter gate width, the RC delays of the metal interconnections significantly increase as the device feature size is below 250 nm. As a result, the theoretical maximum bandwidth of copper-based interconnections is 8 GHz. In addition, the increasing resistance due to the dimension reduction of metal wires also leads to considerable heat dissipation. Limited by the two important issues, metal interconnections becomes not ideal for on-chip, ultrahigh-speed data transportation when the feature size shrinks

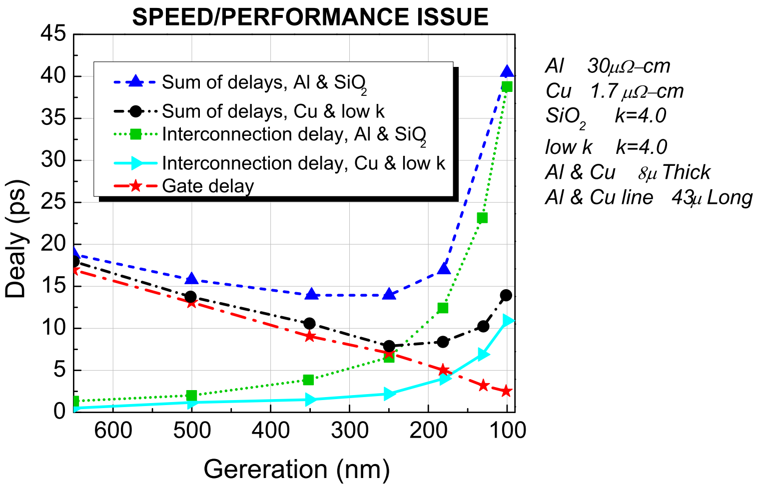

Figure 1.3: Calculated gate delay and wire delay as a function of the device feature size, showing increasing delays of metal interconnections when the device feature size is smaller than 200 nm (Reproduced from [1]).

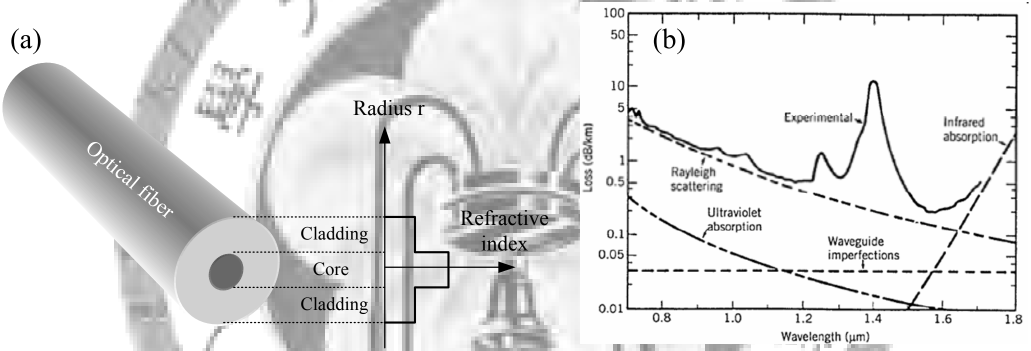

Figure 1.4: (a) Structure of a step index optical fiber. (b) Loss spectrum for silica optical fibers.

to nanometer-scale. Thus, it is critical to develop new, high-speed, and low power dissipation interconnections for next generation information technology as data-transmission rates continue to rise.

1.2 Fiber-optic communications

Another important area in modern information technology is the fiber-optic communication. Since the invention of optical fibers, fiber-optical communications have achieved a revolutionary success for communication networks. The optical fibers used in optical

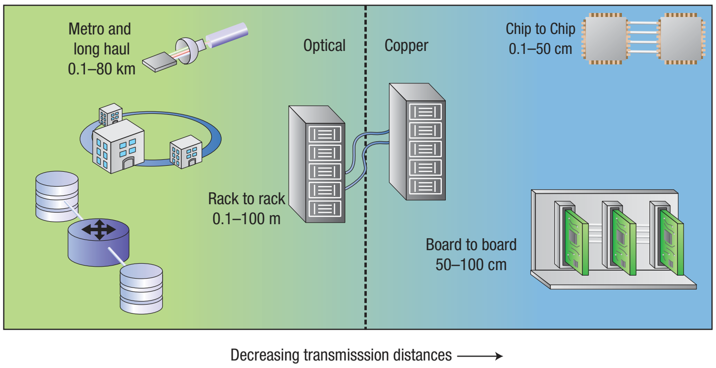

Figure 1.5: Today's communication technology as a function of distance [2].

communications are usually made of silica (SiO_2) with the core lightly doped. As a result, the fiber core has a higher refractive index than that of the cladding layer, as shown in Fig. 1.4. Thus, when light is sent into an optical fiber, the refractive index contrast between the core and cladding layer can lead a good optical confinement for the incident light to propagate in a long distance. Figure 1.4(b) shows the loss spectrum of silica optical fibers. There are two important windows for telecommunications. The first one is near 1300 nm, called the original band (O-band) with the least dispersion, while the second one is near 1550 nm, called the conventional band (C-band) with the least loss (0.21 dB/km). Based on the advantages of low-cost, lower power dissipation, and high transmission rates, the fiber-optic communications has been widely used in mid- and long-range data transportation. On the other hand, copper based interconnections are still dominant for short-distance data transportation nowadays. However, owing the limited bandwidth and heat dissipation issues as mentioned earlier, a new communication technology is needed to replace the current copper-based interconnections as data-transportation rates continue to rise, and optical interconnection is one of the most promising candidates.

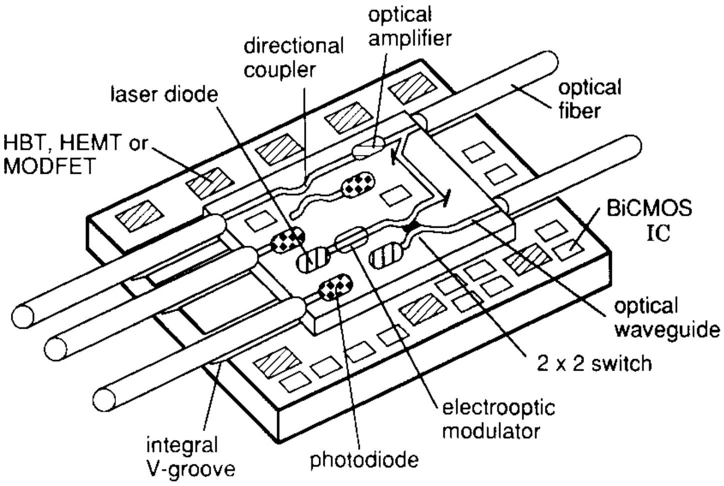

Figure 1.6: A silicon electronic-photonic superchip [3] .

1.3 Silicon photonics and its applications

In 1980's, the concept of integrated photonics has been proposed to develop high performance electronic-photonic integrated circuits. While most photonic devices are discrete components and large in size, the basic idea of integrated photonics is to miniaturize and integrate various photonic devices, such as lasers, modulators, and photodetectors, with various electronic devices on a single chip to dramatically enhance the performance and enrich the functionality of the chip, that is, electronic-photonic integrated circuits (EPICs). Several material systems have been proposed as potential platforms for developing electronic-photonic integrated circuits, such as $LiNbO_3$, InP, GaAs, silicon on insulator (SOI), and silicon (Si). However, except for Si and SOI, other platforms are too expensive to commercialize and not compatible with the well-developed Si CMOS technology. As a result, integrated photonics is likely to be Si-based or SOI-based, that is, *Si photonics*. Silicon-based photonics is a promising technology to take over the conventional copper-based electrical links. Photons are electrically neutral and massless particles which can propagate in a long distance with negligible heat dissipation and cross talk. By using photons instead of electrons as the information carriers, the two important bottle-

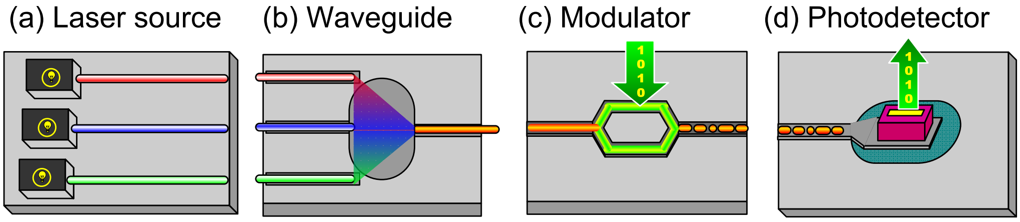

Figure 1.7: Fundamental building blocks for Si-based on-chip optical networks.

necks in the current electrical interconnections, that is, bandwidth and heat dissipation issues, can be solved. Besides, using different wavelengths of light to carry different signals on a single optical fiber allows for multiple-channel data-transportation to dramatically enhance the capacity, that is, wavelength-division multiplexing (WDM) technology.

However, while Si has been widely used in microelectronics, it is very difficult to use Si for various active photonic devices, such as modulators or lasers. This is due to the lack of appreciable electro-optic effect owing to its crystal symmetry, and low light-emitting efficiency owing to its indirect bandgap in nature. The main challenge in silicon photonics is to use either Si or other materials which can be monolithicly grown on silicon substrates to develop, miniature, and integrate various photonic devices on an single Si chip. After the various Si-based photonic devices are developed, Si-photonics can bring us terabit scale communication networks.

1.4 On-chip optical interconnections

To realize on-chip high-speed optical networks for inter-chip or intra-chip interconnections, high-performance Si-based photonic devices are necessary. Figure 1.7 shows a typical optical communication system, including four major parts: generation of light, propagation of light, modulation of light, and detection of light. For the generation of light, lasers are desirable to generate coherent light. Then, light channels can be optical waveguides or optical fibers. Subsequently, modulators are preferred to optically encode the light signals at the transmitted end. Finally, at the receiver end, photodetectors convert the encoded light signals to electrical signals. Thus, to construct on-chip, high-speed, and low-power optical networks, high-performance Si-based lasers, modulators, waveguides, and photodetectors have to be demonstrated first. So far, all components have been realized, except for efficient electrically-pumped Si-based lasers.

1.4.1 Si-based light sources

Silicon-based light sources can be either LEDs or lasers. To be useful for integrated photonics, a Si-based light source is desirable to at least satisfy the following requirements: (1) it can monolithicly grown on silicon substrates, (2) it emits light at wavelength around 1550 nm or 1300 nm, (3) it is compatible with the Si CMOS processing, and (4) it is desirable to be electrically pumped. Owing to the indirect bandgap in nature, the light emitting efficiency in Si is very low, so is Ge. As a result, achieving lasing action in group-IV semiconductors is very challenging and an efficient Si-based light emitters are the holy grail in silicon photonics. If a Si-based laser satisfied the above requirements can be realized, it will immediately produce high-performance electronic-photonic integrated circuits.

1.4.2 Si-based optical modulators

High-speed Si-based optical modulators are another important component for Si photonics. Although modulation of light can be achieved by direct modulation on lasers, the modulation speed is not fast and has significant chirps. As a result, using modulators to optically encode light signals is preferred because of their high-speed operation and low chirps. To achieve effective modulation in semiconductors, typical methods are to change the refractive indices or absorption coefficients by linear electro-optic and electroabsorption effects. However, it is challenging to achieve effective and fast modulation in Si because of the lack of appreciable linear electro-optic (Pockels) and electroabsorption effects in Si [4], [23]. Although Si modulators based on the free-carrier plasma dispersion effect have been recently demonstrated [6], [7], they require long device lengths or high-quality-factor resonators, and consume significant amounts of power. Thus, small, high-speed, and low-power optical modulators are still needed for high density electronic-photonic integrated circuits.

1.5 Outline of this dissertation

This dissertation focuses on the research of using the SiGeSn material system for new Si-based lasers and electroabsorption modulators. Chapter 2 briefly describes the fundamental physical properties of Si, Ge, and α-Sn as well as their compounds to seek their possible applications on electronics and photonics. In chapter 3, we propose to use tensile-strained, n-type doped Ge/$\mathrm{Si}_x\mathrm{Ge}_y\mathrm{Sn}_{1-x-y}$ quantum wells as a gain medium to develop an electrically-pumped Si-based laser for C-band applications. We develop a theoretical model for laser analysis, including the strained electronic band structure, carrier occupation, polarization-dependent optical gain, free-carrier absorption, polarization-dependent optical confinement factors, and threshold analysis. Chapter 4 presents and analyzes a strain-balanced $\mathrm{Ge}_z\mathrm{Sn}_{1-z}$/$\mathrm{Si}_x\mathrm{Ge}_y\mathrm{Sn}_z$ quantum well laser for mid-infrared applications. The use of direct-bandgap GeSn alloys can achieve population inversion for laser applications. In chapter 5, we propose and analyze a polarization-insensitive electroabsorption waveguide modulator using tensile-strained Ge/$\mathrm{Si}_x\mathrm{Ge}_y\mathrm{Sn}_{1-x-y}$ quantum wells based on the quantum-confined Stark effect (QCSE) for 1550 nm operation. We develop a theoretical model to describe the quantum-confined Stark effect in a quantum well. We will compare our theoretical results for the quantum-confinement Stark effect in Ge/SiGe QWs with the experimental data. Then, we present our design and analysis of a polarization-insensitive electroabsorption waveguide modulator using tensile-strained Ge/Si$_x$Ge$_y$Sn$_{1-x-y}$ QWs for 1550 nm operation. Chapter 6 proposes and analyzes an electroabsorption waveguide modulator employing strain-free Ge$_z$Sn$_{1-z}$/Si$_x$Ge$_y$Sn$_{1-x-y}$ QWs for 1550 nm operation. Chapter 7 briefly summaries the major results of this dissertation and suggests possible future works.

Bibliography

[1] L. Pavesi, “Will silicon be the photonic material of the third millenium?” J. Phys.: Condens. Matter **15**, R1169–R1196 (2003).

[2] A. Alduino and M. Paniccia, “Interconnects: wiring electronics with light,” Nature Photon. **1**, 153–155 (2007).

[3] R. Soref, “Silicon-based optoelectronics,” Pro. IEEE **81**, 1687–1706 (1993).

[4] R. Soref and B. Bennett, “Electrooptical effects in silicon,” IEEE J. Quantum Electron. **23**, 123–129 (1987).

[5] R. Soref and J. Larenzo, “All-silicon active and passive guided-wave components for $\lambda = 1.3$ and 1.6 $\mu\mathrm{m}$,” IEEE J. Quantum Electron. **22**, 873–879 (1986).

[6] A. Liu, R. Jones, L. Liao, D. Samara-Rubio, D. Rubin, O. Cohen, R. Nicolaescu, and M. Paniccia, “A high-speed silicon optical modulator based on a metal-oxide-semiconductor capacitor,” Nature **427**, 615–618 (2004).

[7] Q. Xu, B. Schmidt, S. Pradhan, and M. Lipson, “Micrometre-scale silicon electro-optic modulator,” Nature **435**, 325–327 (2005).

國立臺灣大學 · 敦品勵學 · 愛國愛人

Chapter 2

Fundamental physical properties of SiGeSn material system

This chapter describes fundamental physical properties of silicon (Si), germanium (Ge), and alpha-tin (α-Sn), including their electronic band structures, optical properties, and mechanical properties.

2.1 Electronic band structure

To explore new possibilities of using SiGeSn material systems for electronic and photonic applications, it is a good idea to look into the band structures of Si, Ge, and α-Sn first. Si and Ge crystalize in the diamond cubic structure. Figure 2.1 shows the band structures of single-crystal Si and Ge calculated by the nonlocal pseduopotential method [1]. Clearly, both of them are indirect bandgap materials, that is, the conduction band minimum and the valence band maximin are not at the same point in k-space. For Si, the valence band maximum is at Γ point with degenerate light-hole (LH) and heavy-hole (HH) bands. The lowest conduction band is at Δ point, which is about $0.85\pi/a$ along the $\langle 100 \rangle$ direction with a being the lattice constant. The energy gap for the Δ point is 1.1242 EA at 300 K. Due to the sixth equivalent $\langle 100 \rangle$ directions, there are six minima of the Δ-

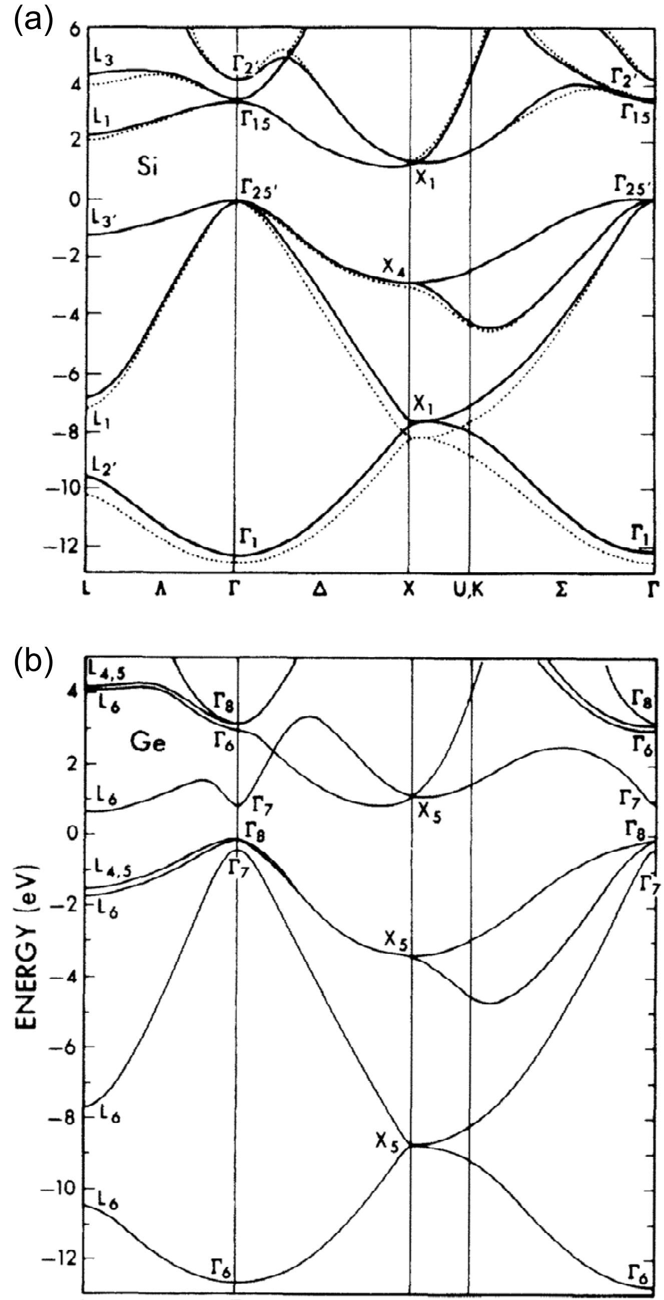

Figure 2.1: Band structures for (a) Si and (b) Ge calculated by nonlocal pseudopotential method (solid line) and local pseudopotential method (dashed line) [1].

valley conduction band. The next conduction minima is at L-point $(\pi/a, \pi/a, \pi/a)$ with a bandgap of 1.65 EA, and the direct Γ-conduction band minimum is situated 4.185 EA above the valence band maximum.

For Ge, the valence band has its maximum at the Γ_8^+ point with degenerate LH and HH bands. The lowest conduction band edge is located at L-point along the $\langle 111 \rangle$ direction with a bandgap of 0.665 EA at 300 K. Although there are eight equivalent $\langle 111 \rangle$ conduction valleys, but only half of them are located in the first Brillouin zone. Thus, there are four the equivalent L-conduction valleys. The direct Γ-valley bandgap is 0.7985 EA and the X-valley bandgap is 1.16 EA, respectively. Ge is attractive for photonic applications because its direct bandgap is about 0.8 EA at room temperature, correspondingly to the most popular wavelength of 1550 nm widely used in telecommunications. Although Ge is still an indirect bandgap semiconductor, which prevents it from being a gain medium for light sources, significant progresses on passive devices, such as photodetectors, associated with its direct bandgap have been achieved [2, 3, 4]. In addition, owing to the small energy difference between the direct and indirect conduction band edges of Ge, possibilities of transferring Ge into a direct bandgap semiconductor via bandgap engineering have been proposed, such as GeSn alloys [5] and tensile-strained Ge [6].

For Sn, there are two major allotropes, α-Sn (gray-tin) and β-tin (white-tin). Above 13.2 °C, tin exists in the metallic β-form. Below 13.2 °C, tin exists in the gray α-form, a semiconductor with diamond cubic crystal structure similar to silicon and germanium. Figure 2.2 shows the band structure of α-Sn. One unique property of α-Sn is that its *S*-like Γ_7^- band edge is situated below the *P*-like Γ_8^+ band edge by 0.413 EA. Thus, if one defines that the valence band is the Γ_8^+ band as those in Si and Ge, the direct bandgap of α-Sn is *negative*. Meanwhile, the next conduction band is located at L_6 point above the Γ_8^+ band

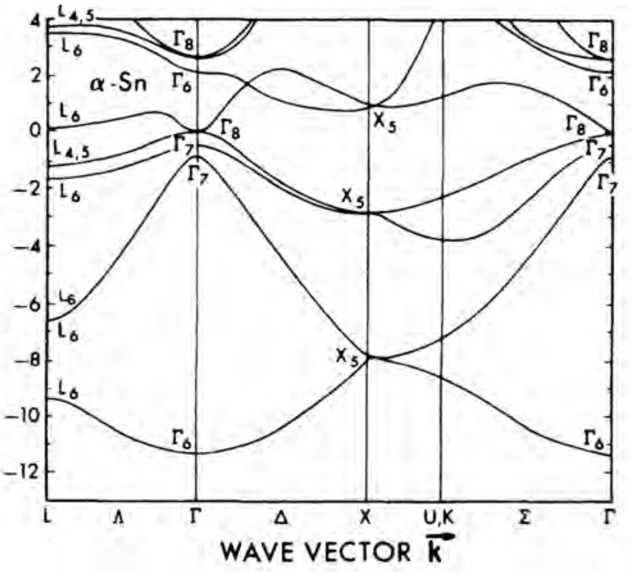

Figure 2.2: Band structure for α-Sn calculated by the nonlocal pseudopotential method [1].

edge by 0.094 EA and the bandgap of the X-valley conduction band is 0.9 EA. Thus, by incorporating α-Sn into Si or Ge, the direct bandgap of Si or Ge decreases very rapidly and can be possibly smaller than the indirect bandgaps. Thus, direct-bandgap GeSn and SiSn alloys are possible to achieve for new photonic applications.

2.2 Lattice constant and direct bandgap

A bandgap versus lattice constant diagram in compound semiconductors is very important and fundamental when one seeks their possible applications. Figure 2.3 depicts the direct bandgaps of Si, Ge, and α-Sn as well as their possible binary and ternary compounds, compared with those of typical III-V semiconductors. The lattice constants of Si and Ge at room temperature are 5.4307 Å and 5.6573 Å, respectively. Nevertheless, the lattice constant of α-Sn is 6.4892 Å, which is much larger than those of Si and Ge. Thus, the lattice constant of ternary SiGeSn alloys can possibly range from 5.4307 Å to 6.4892 Å, which can almost cover those of all III-V semiconductors. This wide range

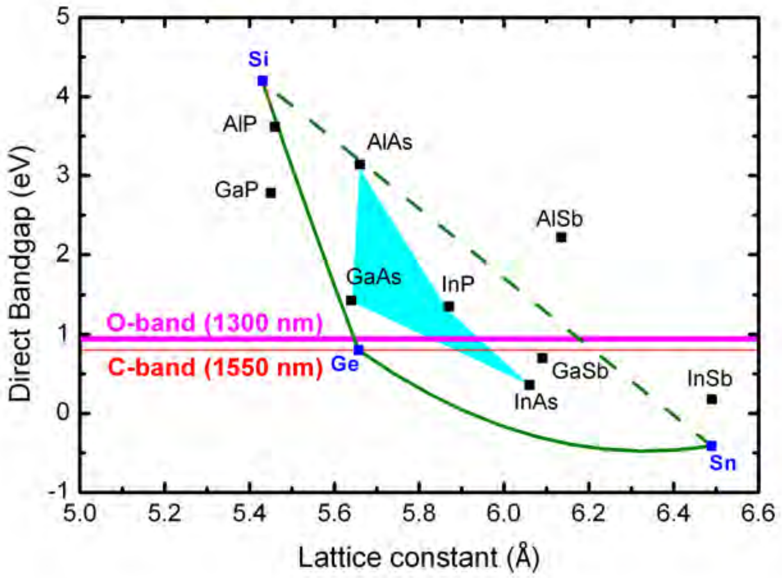

Figure 2.3: Direct bandgaps of Si, Ge, α-Sn, and their compounds as a function of the lattice constants, compared with those of III-V semiconductors. The energy bowing effects for SiGe and GeSn alloys are included. Because of insufficient experimental data for SiSn alloys, a dashed line is shown for illustration.

of lattice constant of ternary SiGeSn alloys are very useful in twofold. (1) It provides additional flexibility in stain and bandgap engineering for group-IV semiconductors in contrast to the conventional SiGe material system. Thus, some ideas which cannot be realized based on the conventional SiGe material system now become possible using the novel SiGeSn material system, for example, growing tensile-strained Ge quantum wells on SiGeSn layers. (2) It can serve as a virtual substrate for group-IV or III-V semiconductors to grow upon silicon substrates for new electronic and photonic devices. Integrating III-V semiconductors on silicon is also an important research area. As the scaling down of the minimum feature size in CMOS technology is approaching its physical limitation and the gain from size reduction is becoming less and less, III-V on silicon is a possible solution as a means of continuing scaling and reducing power consumption [7]. However, owing to the huge difference in lattice constant between Si and III-V compounds, as shown in Fig. 2.3, a compliant buffer layer is required to growing III-V system on silicon. Here the novel SiGeSn material system has the potential to serve the purpose [2] and the direct integration of GaAs on silicon substrates via a GeSn buffer layer [9], and InGaP/InGaAs layers on a silicon substrate via a SiGeSn buffer layer for high-efficiency, low-cost solar cells have been reported [10]. Thus, the ternary SiGeSn is very promising for a new buffer technology for electronic and photonic applications. Besides, Fig. 2.3 also suggests that the ternary SiGeSn has a widely tunable direct bandgap. Although so far the compositions of Sn and Si are still limited in the ternary SiGeSn alloy, Ge-rich SiGeSn layers have been experimentally shown for its tunable direct bandgap of 0.4−1.4 EA, covering the two important telecom windows of 1300 nm and 1550 nm. Thus the SiGeSn material system is promising to replace the current InGaAsP/InGaAlAs material system for the development of various photonic devices for telecommunications, such as lasers, modulators, and detectors. Indeed, GeSn photodetectors have been demonstrated for their advantageous performance for full spectral range telecommunication applications [11] over the conventional Ge photodetectors.

2.3 Refractive index

Refractive indices are one important and fundamental optical constant for designing various semiconductor photonic devices, such as waveguides and optical cavities. For Si, its refractive index n at room temperature can be described by the Herzberger-type dispersion formula [10]

$$n = A + BL + CL^2 + D\lambda^2 + E\lambda^4, \tag{2.1}$$

where $L = 1/(\lambda - 0.028)$ with λ being the wavelength in micrometers. In the wavelength range of $1.12 - 588\ \mu\text{m}$, those parameters are

$$\begin{aligned}
A &= 3.41906, \\
B &= 1.23172 \times 10^{-1}, \\
C &= 2.65456 \times 10^{-2}, \\
D &= -2.66511 \times 10^{-8}, \\
E &= 5.45852 \times 10^{-14}.
\end{aligned} \tag{2.2}$$

For Ge, its refractive index n at temperature T can be described by the Sellmeier-type equation [11]

$$n^2 = A + B\lambda^2/(\lambda^2 - C) + D\lambda^2/(\lambda^2 - E). \tag{2.3}$$

In the spectral range of $2 - 40\ \mu\text{m}$, those parameters are given as follows

$$\begin{aligned}
A &= -6.040 \times 10^{-3}T + 11.05128, \\
B &= 9.295 \times 10^{-1}T + 4.00536, \\
C &= -5.292 \times 10^{-4}T + 0.59999034, \\
D &= 4.151 \times 10^{-4}T + 0.09145, \\
E &= 1.51408T + 3426.5.
\end{aligned} \tag{2.4}$$

However, for α-Sn, there is no sufficient experimental data to rule out the refractive index and only few data are available in the literature [14]. Figure 2.4 shows the refractive index spectra for Si, Ge, and α-Sn at room temperature. In the near infrared spectral wavelength of $0.7 - 5\ \mu\text{m}$, α-Sn has a large refractive index around 4.5−5, which is higher than those

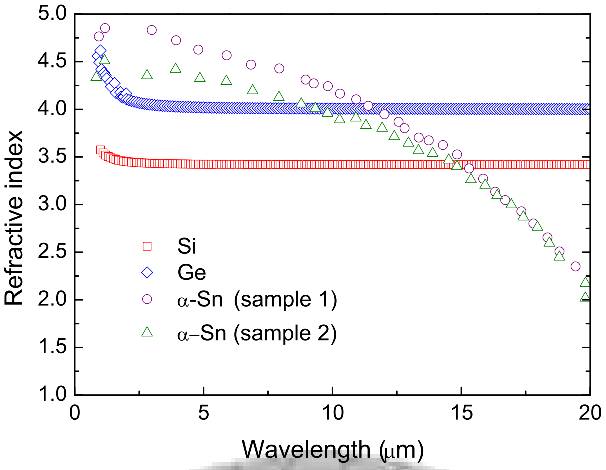

Figure 2.4: Refractive indices of Si, Ge, and α-Sn as a function of wavelength. The data for α-Sn are reproduced from [14].

of Si (∼3.4) and Ge (4.2−4.4). As a result, SiGeSn alloys with a high α-Sn composition will result in a high refractive index. This is an important issue for SiGeSn-based photonic devices.

2.4 Mechanical properties

In recent years, strain effects on the band structure of semiconductors have been intensively studied to the improved performance of electronic and photonic devices. By growing epitaxial layers pseduomorghically on a lattice-mismatched (virtual) substrate, the in-plane lattice constant of the epitaxial layer will be either expanded or compressed to equal to that of the (virtual) substrate. In this way, strain due to lattice mismatch can be introduced into semiconductors. With the rapid development of semiconductor growth technologies, such as molecular beam epitaxy (MBE) and metal-organic chemical vapor deposition (MOCVD), growing highly strained epitaxial layers becomes possible and photonic devices using strained semiconductors exhibits superb performance than unstrained ones. For example, strained quantum-well lasers have been shown to have a

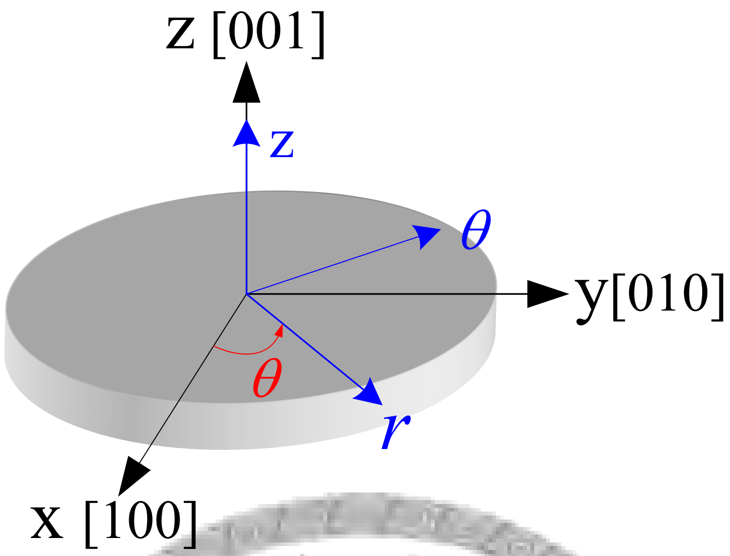

Figure 2.5: Coordinate systems for a (001)-oriented cubic semiconductor for analyzing the mechanical properties.

Table 2.1: Stiffness matrix elements for Si, Ge, and α-Sn.

	Si	Ge	α-Sn
C_{11} (GPa)	165.77	128.53	69.00
C_{12} (GPa)	63.93	48.26	29.30
C_{44} (GPa)	79.62	68.30	36.20

lower threshold current density than that of unstrained ones [1]. However, according to the Matthews and Blakeslee model [16], once the accumulated strain energy density is greater than the elastic energy of dislocations in a strained semiconductor system, the epitaxial layer cannot maintain pseudomorphical and strain-misfit dislocations occur. The strain-misfit dislocations represent unwanted defects which significantly affect the performance of photonic devices. Thus mechanical properties of semiconductors play a very important role when one needs to grow strained semiconductor systems.

To be compatible with the well-developed Si CMOS technology, integrated photonic devices are likely to be fabricated on (001)-oriented silicon substrates. Thus, we investigate the mechanical properties of (001)-oriented Si, Ge, and α-Sn here. Let's consider a (001)-oriented cubic semiconductor referring to a Cartesian coordinate system xyz and a cylindrical coordinate system $r\theta z$, as shown in Fig. 2.5, where the x, y, and z axes point to the [100], [010], and [001] directions, respectively, and θ is the angle measured from the x axis to the x' axis. The stiffness matrix with respect to the xyz coordinate system is

$$\mathbf{C}_{(001)} = \begin{bmatrix} C_{11} & C_{12} & C_{12} & 0 & 0 & 0 \\ C_{12} & C_{11} & C_{12} & 0 & 0 & 0 \\ C_{12} & C_{12} & C_{11} & 0 & 0 & 0 \\ 0 & 0 & 0 & C_{44} & 0 & 0 \\ 0 & 0 & 0 & 0 & C_{44} & 0 \\ 0 & 0 & 0 & 0 & 0 & C_{44} \end{bmatrix}. \tag{2.5}$$

The stiffness matrix elements for Si, Ge, and α-Sn are given in Table 2.1. Since cubic semiconductors are mechanically anisotropic, it would be interesting to study the direction-dependent mechanical properties in the (001) plane. The stiffness matrix referring to the $r\theta z$ cylindrical coordinate system is obtainable from that referring to the xyz Cartesian coordinate system using the tensor transformation equation

$$C'_{ijkl} = a_{im}a_{jn}a_{ko}a_{lp}C_{mnop}, \tag{2.6}$$

where a_{im} is the direction cosine between the new and old coordinate systems, and the engineering notations have been used

$$11 \to 1,\;\; 22 \to 2,\;\; 33 \to 3,\;\; 23 \to 4,\;\; 31 \to 5\;\;, 12 \to 6. \tag{2.7}$$

As a result, the stiffness matrix associated with the $r\theta z$ cylindrical coordinate system is

$$\mathbf{C}_{(001,\theta)} = \begin{bmatrix} C'_{11} & C'_{12} & C'_{13} & 0 & 0 & C'_{16} \\ C'_{12} & C'_{11} & C'_{13} & 0 & 0 & C'_{26} \\ C'_{13} & C'_{13} & C'_{33} & 0 & 0 & 0 \\ 0 & 0 & 0 & C'_{44} & 0 & 0 \\ 0 & 0 & 0 & 0 & C'_{44} & 0 \\ C'_{16} & C'_{26} & 0 & 0 & 0 & C'_{66} \end{bmatrix}. \tag{2.8}$$

The non-zero matrix elements are

$$C'_{12} = \frac{1}{4}\left[C_{11} + 3C_{12} - 2C_{44} - (C_{11} - C_{12} - 2C_{44})\cos 4\theta\right], \tag{2.9}$$

$$C'_{13} = C_{12}, \tag{2.10}$$

$$C'_{16} = -\frac{1}{4}\left(C_{11} - C_{12} - 2C_{44}\right)\sin 4\theta, \tag{2.11}$$

$$C'_{26} = \frac{1}{4}\left(C_{11} - C_{12} - 2C_{44}\right)\sin 4\theta, \tag{2.12}$$

$$C'_{33} = C_{11}, \tag{2.13}$$

$$C'_{44} = C_{44}, \tag{2.14}$$

$$C'_{66} = \frac{1}{4}\left[C_{11} - C_{12} + 2C_{44} - (C_{11} - C_{12} - 2C_{44})\cos 4\theta\right]. \tag{2.15}$$

Note that the non-zero stiffness matrix elements with respect to the $r\theta z$ cylindrical coordinate system depend on the θ variable, implying that a (001)-oriented cubic semiconductor is mechanically anisotropic in the (001) plane. However, the stiffness matrix is not an intuitive quantity to describe the stiffness of a material, but the elastic and shear moduli. To obtain the directional elastic and shear moduli, we can first find the compliance matrix associated with the $r\theta z$ cylindrical coordinate system from the stiffness matrix by

$\mathbf{S} = \mathbf{C}^{-1}$

$$\mathbf{S}_{(001,\theta)} = \mathbf{C}_{(001,\theta)}^{-1} = \begin{bmatrix} S'_{11} & S'_{12} & S'_{13} & 0 & 0 & S'_{16} \\ S'_{12} & S'_{11} & S'_{13} & 0 & 0 & S'_{26} \\ S'_{13} & S'_{13} & S'_{33} & 0 & 0 & 0 \\ 0 & 0 & 0 & S'_{44} & 0 & 0 \\ 0 & 0 & 0 & 0 & S'_{44} & 0 \\ S'_{16} & S'_{26} & 0 & 0 & 0 & S'_{66} \end{bmatrix}. \tag{2.16}$$

The corresponding compliance matrix elements are

$$S'_{11} = \frac{1}{8}\left[6S_{11} + 2S_{12} + S_{44} + (2S_{11} - 2S_{12} - S_{44})\cos 4\theta\right], \tag{2.17}$$

$$S'_{12} = \frac{1}{8}\left[2S_{11} + 6S_{12} - S_{44} - (2S_{11} - 2S_{12} - S_{44})\cos 4\theta\right], \tag{2.18}$$

$$S'_{13} = S_{12}, \tag{2.19}$$

$$S'_{16} = -\frac{1}{4}(2S_{11} - 2S_{12} - S_{44})\sin 4\theta, \tag{2.20}$$

$$S'_{26} = \frac{1}{4}(2S_{11} - 2S_{12} - S_{44})\sin 4\theta, \tag{2.21}$$

$$S'_{33} = S_{11}, \tag{2.22}$$

$$S'_{44} = S_{44}, \tag{2.23}$$

$$S'_{66} = \frac{1}{2}\left[2S_{11} - 2S_{12} + S_{44} - (2S_{11} - 2S_{12} - S_{44})\cos 4\theta\right], \tag{2.24}$$

and the relationships between the stiffness and compliance matrix elements are

$$S_{11} = \frac{C_{11} + C_{12}}{(C_{11} - C_{12})(C_{11} + 2C_{12})}, \tag{2.25}$$

$$S_{12} = \frac{-C_{12}}{(C_{11} - C_{12})(C_{11} + 2C_{12})}, \tag{2.26}$$

$$S_{44} = 1/C_{44}. \tag{2.27}$$

Then the in-plane elastic modulus E_{in} and shear modulus G_{in} can be obtained from the compliance matrix elements

$$E_{\text{in}}(\theta) = (S'_{11})^{-1} = \left[S_{11} - \frac{1}{4}(1 - \cos 4\theta)\left(S_{11} - S_{12} - \frac{S_{44}}{2}\right)\right]^{-1}, \tag{2.28}$$

$$G_{\text{in}}(\theta) = (S'_{66})^{-1} = \left[S_{44} + (1 - \cos 4\theta)\left(S_{11} - S_{12} - \frac{S_{44}}{2}\right)\right]^{-1}, \tag{2.29}$$

and the out-of-plane elastic modulus E_{out} and shear modulus G_{out} are

$$E_{\text{out}}(\theta) = S_{11}^{-1}, \tag{2.30}$$

$$G_{\text{out}}(\theta) = S_{44}^{-1}. \tag{2.31}$$

Figure 2.6 shows the directional elastic and shear moduli in the (001) plane for Si, Ge, and α-Sn. First, both the elastic and shear moduli for Si, Ge, and α-Sn are direction-dependent, indicating that Si, Ge, and α-Sn are mechanically anisotropic in the (001) plane. Among the three semiconductors, Si has the largest elastic and shear moduli, indicating that Si is the "*stiffest*" material among the three semiconductors. Owing to the high stiffness, silicon has become the most commonly used material for MEMS manufacturing. Then, the elastic and shear moduli of Ge are 20.9% and 16.25% smaller than those of Si. Nevertheless, the elastic and shear moduli of α-Sn are much smaller than those of Si by 68.21% and 62.5%, respectively, implying that α-Sn is a very "*soft*" material. Thus, incorporating α-Sn into Si or Ge can effectively reduce their stiffness for strain engineering.

When a cubic epitaxial layer is pseudomorphically grown on a lattice-mismatched (001)-oriented substrate and the crystal growth direction is along the z direction, the strain

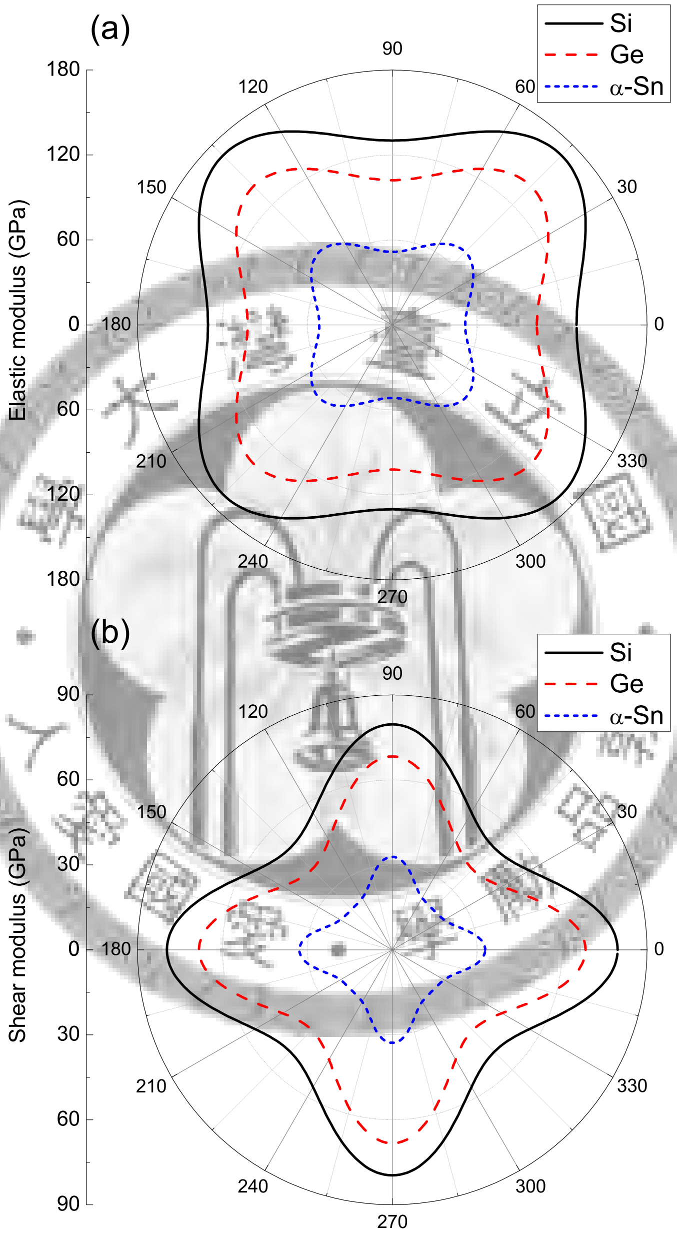

Figure 2.6: Directional (a) elastic and (b) shear moduli for Si, Ge, and α-Sn in the (001) plane as a function of θ.

Table 2.2: Proportional constant for strain energy density of Si, Ge, and α-Sn.

	Si	Ge	α-Sn
$C_{11}+C_{12}-2\frac{C_{12}^2}{C_{11}}$ (GPa)	180.39	141.49	73.41

field induced by the lattice mismatch is

$$\varepsilon_{xx}=\varepsilon_{yy}=\varepsilon=\frac{a_0-a}{a}, \tag{2.32}$$

$$\varepsilon_{zz}=-2\frac{C_{12}}{C_{11}}\varepsilon, \tag{2.33}$$

$$\varepsilon_{xy}=\varepsilon_{yz}=\varepsilon_{zx}=0, \tag{2.34}$$

where a and a_0 are the lattice constants of the epitaxial layer and the substrate, respectively. The corresponding strain energy density in the epitaxial layer is

$$\begin{aligned} v &= \frac{1}{2}\boldsymbol{\varepsilon}^{\mathrm{T}}\mathbf{C}\boldsymbol{\varepsilon} \\ &= \left(C_{11}+C_{12}-2\frac{C_{12}^2}{C_{11}}\right)\varepsilon^2. \end{aligned} \tag{2.35}$$

Clearly, the strain energy density is proportional to the in-plane strain squared. Table 2.2 tabulates the constant $C_{11}+C_{12}-2\frac{C_{12}^2}{C_{11}}$ for Si, Ge, and α-Sn. If Si, Ge, and α-Sn layers are subject to the same amount of in-plane strain, the accumulated strain energy density of α-Sn is the smallest among the three semiconductors (59.3% smaller than that of Si, and 48.15% smaller than that of Ge). Thus, Sn-containing group-IV semiconductors accumulate less strain energy than the conventional SiGe material system if they are subject to the same amount of strain, leading to a reduction of strain-misfit dislocations. Although the material quality of epitaxial layers is also highly related to crystal growth conditions and methods, the analysis from mechanical viewpoint can qualitatively explain the advantages of ternary SiGeSn alloys. Based on the compliance of α-Sn and the widely tunable lattice constant of SiGeSn alloys, the SiGeSn material system has the potential to develop a new buffer technology for the direct growth of strained or unstrained semiconductors on silicon. Indeed, high quality, low-defect, strain-relaxed GeSn and SiGeSn buffer layers on silicon have been experimentally demonstrated [2, 17]. Furthermore, due to the reduced stiffness, the SiGeSn alloys are expected to bear a higher strain than the conventional SiGe material system, and highly strained SiGeSn and GeSn have been reported [4], [19].

2.5 Summary

This section briefly introduces the fundamental physical properties of Si, Ge, and α-Sn, including the electronic, optical, and mechanical properties. Based on the understanding of those properties, possible applications of the ternary SiGeSn alloys have been indicated.

Bibliography

[1] J. R. Chelikowsky and M. L. Cohen, "Nonlocal pseudopotential calculations for the electronic structure of eleven diamond and zinc-blende semiconductors," Phys. Rev. B **14**, 556–582 (1976).

[2] L. Colace, G. Masini, G. Assanto, H.-C. Luan, K. Wada, and L. C. Kimerling, "Efficient high-speed near-infrared Ge photodetectors integrated on Si substrates," Appl. Phys. Lett. **76**, 1231–1233 (2000).

[3] Y. Kang, H.-D. Liu, M. Morse, M. J. Paniccia, M. Zadka, S. Litski, G. Sarid, A. Pauchard, Y.-H. Kuo, H.-W. Chen, W. S. Zaoui, J. E. Bowers, A. Beling, D. C. McIntosh, X. Zheng, and J. C. Campbell, "Monolithic germanium/silicon avalanche photodiodes with 340 GHz gain-bandwidth product," Nat. Photon. **3**, 59–63 (2009).

[4] S. Assefa, F. Xia, and Y. A. Vlasov, "Reinventing germanium avalanche photodetector for nanophotonic on-chip optical interconnects," Nature **464**, 80–84 (2010).

[5] G. He and H. A. Atwater, "Interband transition in $\mathrm{Sn}_x\mathrm{Ge}_{1-x}$ alloys," Phys. Rev. Lett. **79**, 1937–1940 (1997).

[6] J. Menéndez and J. Kouvetakis, "Type-I Ge/$\mathrm{Ge}_{1-x-y}\mathrm{Si}_x\mathrm{Sn}_y$ strained-layer heterostructures with a direct bangap," Appl. Phys. Lett. **85**, 1175–1177 (2004).

[7] M. Radosavljevic, B. Chu-Kung, S. Corcoran, G. Dewey, M. K. Hudait, J. M. Fastenau, J. Kavalieros, W. K. Liu, D. Lubyshev, M. Metz, K. Millard, N. Mukherjee, W. Rachmady, U. Shah, and R. Chau, "Advanced high-k gate dielectric for high-performance short-channel $\mathrm{In}_{0.7}\mathrm{Ga}_{0.3}\mathrm{As}$ quantum well field effect transistors on silicon substrate for low power logic applications," Int. Electron Devices Meet. p. 319 (2009).

[8] J. Xie, J. Tolle, V. R. D'Costa, A. V. G. Chizmeshya, J. Menéndez, and J. Kouvetakis, "Direct integration of active $\mathrm{Ge}_{1-x}(\mathrm{Si}_4\mathrm{Sn})_x$ semiconductors on Si(100)," Appl. Phys. Lett. **95**, 181909 (2009).

[9] R. Roucka, J. Tolle, C. Cook, A. V. G. Chizmeshya, J. Kouvetakis, V. D'Costa, J. Menéndez, Z. D. Chen, and S. Zollner, "Versatile buffer layer architectures based on $\mathrm{Ge}_{1-x}\mathrm{Sn}_x$ alloys," Appl. Phys. Lett. **86**, 191912 (2005).

[10] Y.-Y. Fang, J. Xie, J. Tolle, R. Roucka, V. R. D'Costa, A. V. G. Chizmeshya, J. Menéndez, and J. Kouvetakis, "Molecular-based synthetic approach to new group IV materials for high-efficiency, low-cost solar cells and Si-based optoelectronics," J. Am. Chem. Soc. **130**, 16095–16102 (2008).

[11] J. Mathews, R. Roucka, J. Xie, S.-Q. Yu, J. Menéndez, and J. Kouvetakis, "Extended performance GeSn/Si(100) p-i-n photodetectors for full spectral range telecommunication applications," Appl. Phys. Lett. **95**, 133506 (2009).

[12] D. F. Edwards, "Silicon (Si)," in *Handbook of Optical Constants of Solids,* , E. D. Palik, ed. (Academic, Orlando, Florida, 1985), pp. 547–569.

[13] R. F. Potter, "Germanium (Ge)," in *Handbook of Optical Constants of Solids,* , E. D. Palik, ed. (Academic, Orlando, Florida, 1985), pp. 465–478.

[14] R. E. Lindquist and A. W. Ewald, "Optical constants of single-crystal gray tin in the infrared," Phys. Rev. **135**, A191–A194 (1964).

[15] P. Thijs, L. Tiemeijer, P. Kuindersma, J. Binsma, and T. Van Dongen, "High-performance 1.5 μm wavelength InGaAs-InGaAsP strained quantum well lasers and amplifiers," IEEE J. Quantum Electron. **27**, 1426 –1439 (1991).

[16] J. W. Matthews and A. E. Blakeslee, "Defects in epitaxial multilayers : II. dislocation pile-ups, threading dislocations, slip lines and cracks," J. Crys. Growth **29**, 273 – 280 (1975).

[17] J. Kouvetakis, J. Menéndez, and A. V. G. Chizmeshya, "Tin-based group IV semiconductors: New platforms for opto- and microelectronics on silicon," Annu. Rev. Mater. Res. **36**, 497–554 (2006).

[18] J. Tolle, R. Roucka, A. V. G. Chizmeshya, J. Kouvetakis, V. R. D'Costa, and J. Menéndez, "Compliant tin-based buffers for the growth of defect-free strained heterostructures on silicon," Appl. Phys. Lett. **88**, 252112 (2006).

[19] R. Soref, J. Kouvetakis, J. Tolle, J. Menéndez, and V. D'Costa, "Advances in SiGeSn technology," J. Mat. Res. **22**, 3281–3291 (2007).

[20] O. Gurdal, P. Desjardins, J. R. A. Carlsson, N. Taylor, H. H. Radamson, J.-E. Sundgren, and J. E. Greene, "Low-temperature growth and critical epitaxial thicknesses

of fully strained metastable $\mathrm{Ge}_{1-x}\mathrm{Sn}_x$ ($x < 0.26$) alloys on Ge(001)2×1," J. Appl. Phys. **83**, 162–170 (1998).

Chapter 3

Tensile-strained, n-type doped Ge/SiGeSn quantum-well lasers at 1550 nm wavelength

In this chapter, we propose an n-doped, tensile-strained Ge-Si$_x$Ge$_y$Sn$_{1-x-y}$ multiple-quantum-well (MQW) laser at 1550 nm wavelength. First, we will introduce the background and physics of radiative recombination processes in direct- and indirect-bandgap semiconductors and point out the reason that Si and Ge are poor light emitters. Then we present our designed structure of n-type doped, tensile-strained Ge/Si$_x$Ge$_y$Sn$_{1-x-y}$ WAS as a gain medium to develop electrically-pumped Si-based lasers. We suggest the combination of using tensile strain and n-type doping in Ge WAS to achieve population inversion. The use of tensile strain can effectively reduce the energy difference between the direct and indirect conduction band edges of the Ge wells. By employing extrinsic electrons from n doping to fill the L-valley conduction subbands up to the onset of the Γ-valley conduction subband, injected electrons via bias current are allowed to populate the direct Γ-conduction subband to achieve population inversion. We show our theoretical model for the strained electronic band structure, polarization-dependent optical gain, free-carrier absorption, and polarization-dependent optical confinement factors. Even in

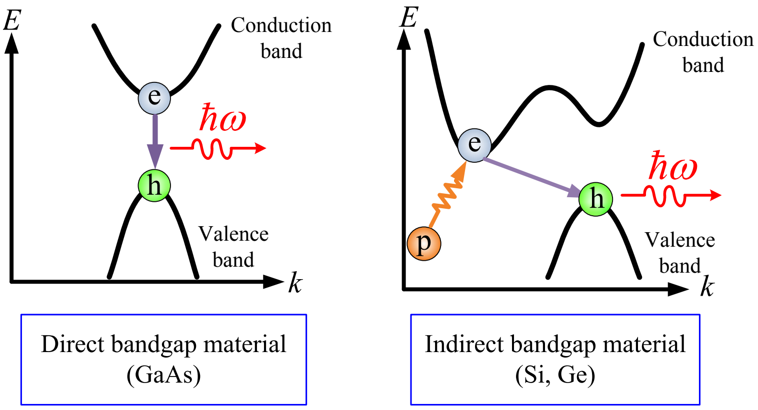

(a)

(b)

Figure 3.1: Radiative recombination processes in (a) direct bandgap and (b) indirect bandgap semiconductors.

the presence of the free-carrier loss, our calculations show that a significant net gain is achievable. We also present our waveguide design to calculate the optical confinement factors of various regions. Threshold analysis indicates that the threshold carrier density of this MQW laser is in an achievable range compared to those of typical III-V MQW lasers. The transparency and threshold current densities are also estimated with reasonable parameters.

3.1 Why cannot Si and Ge emit light?

An efficient silicon-based laser is *the missing component* for silicon-based integrated photonics. The main difficulty is that group-IV semiconductors, such as silicon (Si) and germanium (Ge), are indirect bandgap semiconductors. Figure 3.1 shows the radiative recombination processes in direct-bandgap and indirect-bandgap semiconductors. Electron-hole radiative recombination can only occur if it satisfies the Fermi's golden rule, that is, both energy and momentum have to be conserved [1]. In direct bandgap semiconductors such as GaAS, as shown in Fig 3.1(a), the conduction band minimum and valence band maximum are at the same point in *k*-space. Electrons in the conduction band can recombine with holes in the valence band and emit photons. However, for indirect bandgap semiconductors such as Si and Ge, as shown in Fig. 3.1(b), the conduction band minimum and valence band maximum are not at the same point in k-space. Injected electrons tend to populate the indirect-conduction band instead of the direct conduction band under carrier injection. As a result, the first-order band-edge electron-hole recombination process involving a single photon does not conserve momentum, because photons carry negligible momentum. Therefore, electron-hole radiative recombination can only occur with the assistance of a phonon to conserve momentum. However, such a three-particle interaction in group-IV semiconductors is very inefficient compared with direct transitions in III-V direct-bandgap semiconductors. As a result, group-IV semiconductors are usually poor light emitters. Thus, improving the light-emitting efficiency in group-IV semiconductors has become one challenging task in silicon photonics which has stimulated a significant research effort. Still, a silicon-based laser remains the last unrealized building block of silicon photonics. To be useful for telecommunications or as intra-chip interconnections, it is desirable for a silicon-based laser to satisfy the following key ingredients: (1) the silicon-based laser can be monolithicly grown on silicon substrates, which cost much less than any other semiconductor material; (2) it is compatible with complementary metal-oxide-semiconductor (CMOS) processing, which allows for the integration of the laser with other electronic or optoelectronic components; (3) it emits light around the telecommunication wavelengths of 1300 nm or 1550 nm; and (4) it is desirable to be electrically-pumped, so it requires no additional pump light source. Although lots of efforts have been made to improve the light radiation efficiency of group-IV semiconductors, for example, silicon Raman laser [2], porous silicon [3], and erbium-doped silicon [4], no solution was found that satisfied all the four key ingredients so far.

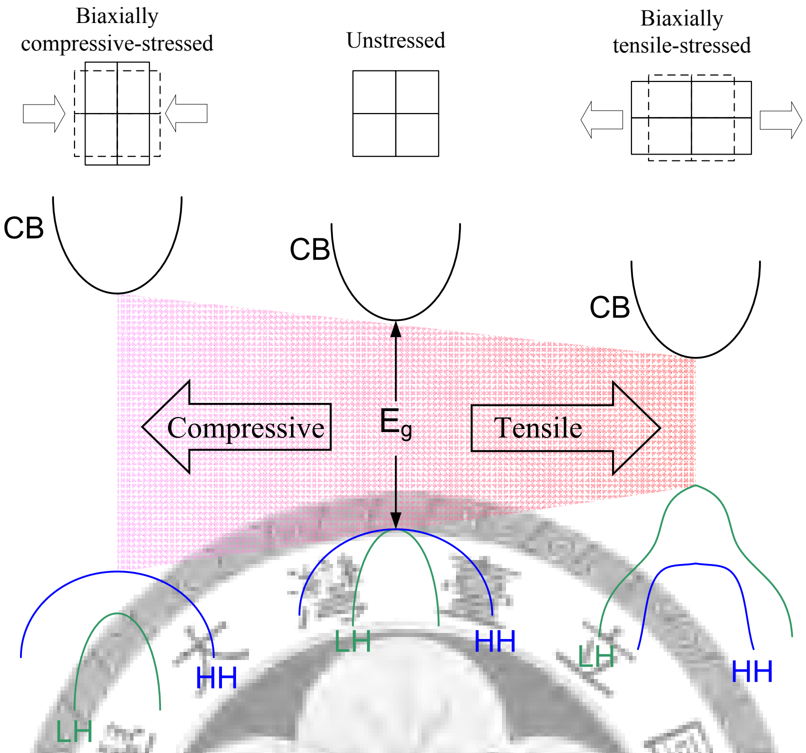

Figure 3.2: Strain effects on bandgap structure of semiconductors.

3.2 Tensile-strained Ge with a direct bandgap

In recent years, strain effects in semiconductors have been intensively investigated for electronic and photonic applications [5]. By introducing strain into semiconductors, bandgaps, effective masses, and carrier mobilities can be engineered to improve performances of electronic and photonic devices [6, 7]. Figure 3.2 shows the band structure in momentum space for a bulk cubic semiconductor under biaxially compressive-stressed, unstressed, and biaxially tensile-stressed conditions, respectively. In the absence of strain effects, light-hole (LH) and heavy-hole (HH) band edges are degenerate at the top of Γ-valence band. When a biaxially tensile stress is introduced into a semiconductor, the semiconductor is subject to an in-plane biaxial tensile strain of ε and an out-of-plane strain of $-2\frac{C_{12}}{C_{11}}\varepsilon$. In this way, the strain effect effectively lowers the conduction band edge and raises the valence band edge, leading to a reduced bandgap. In addition, the tensile strain also splits the HH and LH band edges and makes their dispersion relations

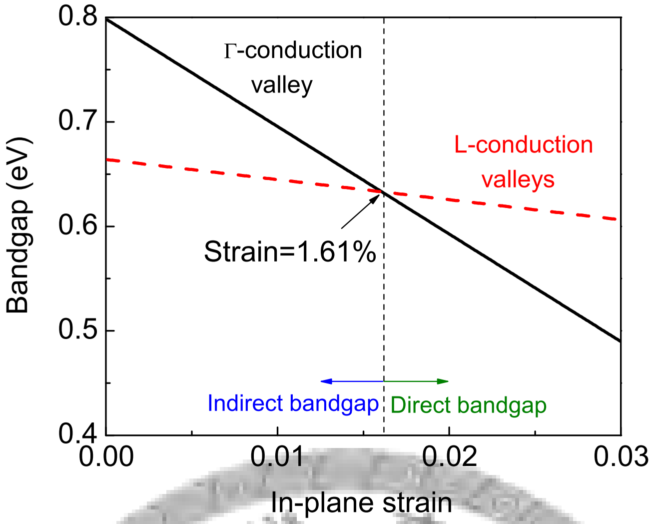

Figure 3.3: Γ- and L-conduction band edges of a biaxially tensile-stressed Ge as a function of in-plane strain. The indirect-to-direct-bandgap transition occurs at an in-plane tensile strain of 1.61%.

nonparabolic due to the valence-band-mixing-effect. As a result, the valence nonparabolicity implies the possibility of engineering hole effective mass and mobility. On the other hand, introducing a biaxially compressive stress into semiconductors raises the conduction band edge and lowers the valence band edge, indicating that the energy bandgap of semiconductors is increased.

Among the various approaches to improve the light-emitting efficiency in group-IV semiconductors, one possibility is to engineer the band structure and convert the group-IV semiconductors into direct-bandgap semiconductors. New idea to crate direct bandgap semiconductors based on the group-IV semiconductors is to grow tensile-strained Ge layers [10], [11]. Although Ge is an indirect bandgap semiconductor with its L-conduction valleys as the lowest conduction band, its direct conduction band edge is situated only 134.5 meV above the bottom of the L-valley conduction band. In addition, the deformation potential of the L-conduction valleys is about five times larger than that of the Γ-conduction valleys. This means the L-conduction band edge will shift much faster than the Γ-conduction band edge under strain effects. Therefore, introducing tensile strain into Ge can effective reduce the energy difference between the Γ- and L-conduction band edges to transfer Ge into a direct-bandgap semiconductor. Figure 3.3 shows the Γ- and L-conduction bandgaps of a biaxially tensile-stressed Ge as a function of in-plane strain. When the in-plane tensile strain is larger than 1.61%, the Γ-conduction band edge can be lower than the L-conduction band edge. Thus, tensile-strained Ge can become a direct-bandgap semiconductor as a gain medium for photonic active applications [11].

3.3 Tensile-strained, n-type doped Ge as a gain medium

Although tensile-strained Ge can become a direct-bandgap material, it is not easy to grow such highly tensile-strained Ge layers with low defect densities. In addition, the required tensile strain for transferring Ge into a direct-bandgap semiconductor also significantly reduces the direct bandgap. Thus, the emission wavelength will significant red shift away from the most popular telecommunication wavelength of 1550 nm. To reduce the required tensile strain for the indirect-to-direct-bandgap transition and maintain proper emission wavelengthes around 1550 nm simultaneously, another promising approach is to introduce n-type doping into Ge. It has been experimentally shown that n-doped Ge/Si superlattices exhibit very strong photoluminescence (PL) and electroluminescence (EL) signals [12], [13]. Besides, the combination of using tensile strain and n-type doping in bulk Ge as gain media has been proposed [14]. Our approach is to grow n-type doped, tensile-strained Ge WAS with SiGeSn barriers as a gain medium to develop electrically-pumped Si-based lasers.

Figure 3.4 shows the scheme of employing tensile strain and n doping in Ge quantum wells to achieve population inversion in the Γ-conduction band of the Ge well. Fig-

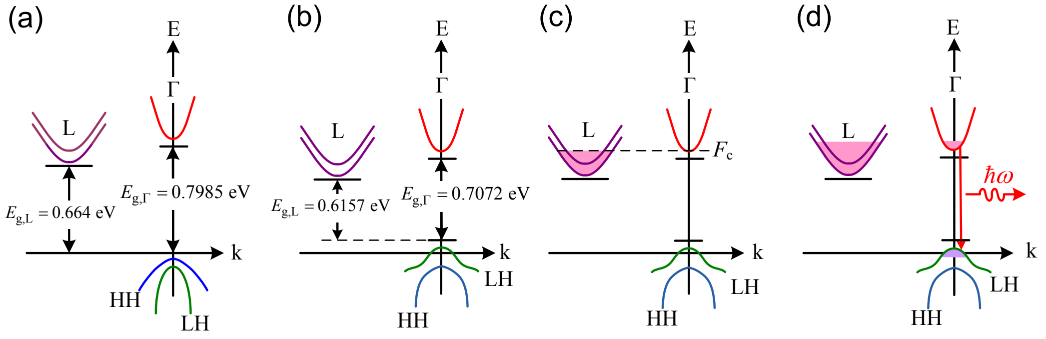

Figure 3.4: (a) Schematic subband structure of an unstrained Ge well. The energy difference between its direct- and indirect-conduction band edges is only 134.5 meV. (b) The introduction of a tensile strain of 0.514% can effectively reduce the energy difference to 91.5 meV. In the valence band, the light-hole (LH) band is the highest valance band due to the tensile strain. (c) Extrinsic electrons from n doping are employed to fill into the L-valley conduction subbands up to the onset of the Γ-valley conduction subband, and make up the remaining energy difference. (d) The injected electrons via bias current can populate the Γ-conduction subband to achieve population inversion and provide significant optical gain.

ure 3.4(a) shows the band structure of an unstrained Ge well. The energy difference between the direct- and indirect-conduction band edges of the Ge well is only 134.5 meV at room temperature. By introducing a tensile strain of 0.514% into the Ge well, the indirect and direct bandgaps are reduced to 0.6157 eV and 0.7072 eV, respectively, as shown in Fig. 3.4(b). The energy difference between the two conduction band edges is thus reduced to 91.5 meV. Then, by building in an electron concentration of $2.14 \times 10^{19}\mathrm{cm}^{-3}$ via n doping into the L-valley conduction subbands, the electron quasi-Fermi level in the conduction band, F_{c}, will rise to the bottom of the lowest Γ-valley conduction subband to compensate for the remaining energy difference of 91.5 meV, as shown in Fig. 3.4(c). Since the states of L-conduction subbands lower than the Γ-conduction subband are mostly occupied by extrinsic electrons, injected electrons by bias current will begin to populate the Γ-conduction subband and thus achieve population inversion. Therefore, electron-hole radiative recombination through the direct transition can bring significant optical gain, as shown in Fig. 3.3(d). By using quantum wells as a gain medium rather than bulk mate-

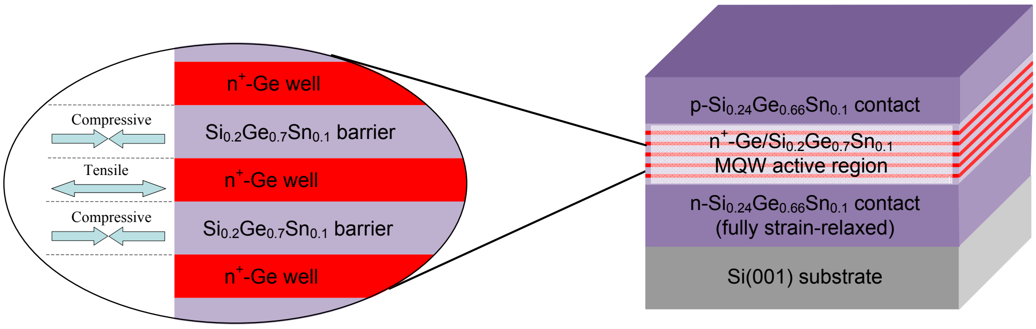

Figure 3.5: Diagram of our proposed n-doped, tensile-strained Ge/Si$_{0.2}$Ge$_{0.7}$Sn$_{0.1}$ MQW structure. The strain-compensated Ge/Si$_{0.2}$Ge$_{0.7}$Sn$_{0.1}$ MQW structure is grown on the silicon substrate via the strain-relaxed Si$_{0.24}$Ge$_{0.66}$Sn$_{0.1}$ buffer layer.

rials, there are several advantages: (1) the n doping requirement is moderate in contrast to that of the bulk counterparts, leading to less free-carrier absorption, (2) although the tensile strain reduces the direct bandgap of Ge, the transition energy (the sum of the direct bandgap and the quantized energies) can be maintained around 0.8 eV, making the emission wavelength around the most popular telecom wavelength of 1550 nm, (3) owing to the improved density of states of quantum-well structures than that of bulk materials, quantum-well structures can provide high material gain to readily overcome free-carrier loss due to the n-type doping and produce significant net optical gain.

3.4 Strain-balanced Ge–SiGeSn multiple quantum well structure

Figure 3.5 shows our proposed n$^+$-Ge/Si$_{0.2}$Ge$_{0.7}$Sn$_{0.1}$ MQW structure. A fully strain-relaxed Si$_{0.24}$Ge$_{0.66}$Sn$_{0.1}$ layer is grown on a (100)-oriented silicon substrate as the virtual substrate for the sequent growth of MQW. The buffer is also n-doped as the bottom contact. Then five pairs of n-doped Ge/Si$_{0.2}$Ge$_{0.7}$Sn$_{0.1}$ WAS, that is, five Ge wells and six Si$_{0.2}$Ge$_{0.7}$Sn$_{0.1}$ barriers, are grown on the n-contact. Finally, the whole structure is capped by a p-doped $\mathrm{Si}_{0.24}\mathrm{Ge}_{0.66}\mathrm{Sn}_{0.1}$ layer. Because the buffer layer is fully strain-relaxed, the in-plane lattice constants of the Ge wells and the $\mathrm{Si}_{0.2}\mathrm{Ge}_{0.7}\mathrm{Sn}_{0.1}$ barriers will be forced to follow that of the buffer layer. The strain field in the ith layer on the buffer layer due to the lattice-mismatch is

$$\varepsilon_{xx}^{i} = \varepsilon_{yy}^{i} = \varepsilon^{i} = \frac{a_0 - a_i}{a_i} \tag{3.1}$$

$$\varepsilon_{zz}^{i} = -2\frac{C_{12}^{(i)}}{C_{11}^{(i)}}\varepsilon^{i} \tag{3.2}$$

$$\varepsilon_{xy}^{i} = \varepsilon_{yz}^{i} = \varepsilon_{zx}^{i} = 0 \tag{3.3}$$

where a_i and a_0 are the lattice constants of the ith layer and the buffer layer, respectively; $C_{11}^{(i)}$ and $C_{12}^{(i)}$ are the stiffness matrix elements of the ith layer. The lattice constant of the Ge wells is smaller than that of the $\mathrm{Si}_{0.24}\mathrm{Ge}_{0.66}\mathrm{Sn}_{0.1}$ buffer layer, so the Ge wells are subjected to a in-plane tensile strain of 0.514%. On the other hand, since the $\mathrm{Si}_{0.2}\mathrm{Ge}_{0.7}\mathrm{Sn}_{0.1}$ barriers have a lattice constant larger than that of the buffer layer, they are subjected to a in-plane compressive strain of 0.154%. In this calculation, we set the width of the Ge quantum well to 70 Å. In order to balance the strain between the tensile-strained Ge wells and the compressive-strained $\mathrm{Si}_{0.2}\mathrm{Ge}_{0.7}\mathrm{Sn}_{0.1}$ barriers, the barrier width is set to 200 Å, so that the whole structure is approximately strain-balanced. Note that Ge layers with a tensile strain of 0.43% grown on a GeSn buffer layer on a silicon substrate [15] or a tensile strain of 0.68% grown on a GeSn buffer layer on a virtual germanium substrate have been experimentally demonstrated [16], so the tensile strain of 0.514% in our proposed Ge wells should be achievable.

3.5 Theoretical model for laser analysis

In this section, we develop a theoretical model for the tensile-strained, n-type doped Ge/SiGeSn quantum well structure, including the strained electronic band structure, carrier occupation, polarization-dependent optical gain, free-carrier absorption, polarization-dependent optical confinement factors, and threshold analysis.

3.5.1 Material parameters

To obtain most parameters for the $\mathrm{Ge}_z\mathrm{Sn}_{1-z}$ and $\mathrm{Si}_x\mathrm{Ge}_y\mathrm{Sn}_{1-x-y}$ material systems, linear interpolations among those of Si, Ge, and α-Sn are used. The linear interpolation formulae for any physical parameter P, except for the bandgaps, are given by

$$P(\mathrm{Ge}_z\mathrm{Sn}_{1-z}) = zP(\mathrm{Ge}) + (1-z)P(\mathrm{Sn}), \tag{3.4}$$

$$P(\mathrm{Si}_x\mathrm{Ge}_y\mathrm{Sn}_{1-x-y}) = xP(\mathrm{Si}) + yP(\mathrm{Ge}) + (1-x-y)P(\mathrm{Sn}). \tag{3.5}$$

The parameters used for this calculation are listed in table 3.1.

Generally, the linear interpolation formulae do not work well for bandgaps of binary or ternary compounds due to significant bowing effects. For Ge-rich $\mathrm{Ge}_z\mathrm{Sn}_{1-z}$ and $\mathrm{Si}_x\mathrm{Ge}_y\mathrm{Sn}_{1-x-y}$ material systems, the unstrained bandgaps can be described by the suggested quadratic polynomials [25, 26, 27]

$$E_{\mathrm{g},\eta}(\mathrm{Ge}_z\mathrm{Sn}_{1-z}) = zE_{\mathrm{g},\eta}(\mathrm{Ge}) + (1-z)E_{\mathrm{g},\eta}(\mathrm{Sn}) - b_\eta^{\mathrm{GeSn}}z(1-z), \tag{3.6}$$

Parameters	Silicon	Germanium	α-Tin
Lattice constants			
a (Å)	5.4307[a]	5.6573[a]	6.4892[a]
Effective masses			
m_{c} (m_0)	0.528[b]	0.038[a]	0.058[a]
$m_{\mathrm{t,L}}$ (m_0)	0.133[d]	0.0807[a]	0.075[e]
$m_{\mathrm{l,L}}$ (m_0)	1.659[d]	1.57[a]	1.478[e]
Luttinger's parameters			
γ_1	4.22[a]	13.38[a]	-14.97[c]
γ_2	0.39[a]	4.24[a]	-10.61[c]
γ_3	1.44[a]	5.69[a]	-8.52[c]
Average valence band energies			
$E_{\mathrm{v,av}}$ (eV)	-0.48[f]	0	0.69[f]
Bandgaps			
$E_{\mathrm{g,\Gamma}}$ (eV)	4.185[a]	0.7985[a]	-0.413[a]
$E_{\mathrm{g,L}}$ (eV)	1.65[a]	0.664[a]	0.092[a]
Δ (eV)	0.044[a]	0.29[a]	0.8[a]
Deformation potentials			
a_{c} (eV)	-10.06[g]	-8.24[h]	-6.00[g]
a_{L} (eV)	-0.66[h]	-1.54[h]	-2.14[e]
a_{v} (eV)	2.46[h]	1.24[h]	1.58[e]
b_{v} (eV)	-2.1[h]	-2.9[h]	-2.7[i]
Elastic constants			
C_{11} (GPa)	165.77[a]	128.53[a]	69.00[a]
C_{12} (GPa)	63.93[a]	48.26[a]	29.30[a]
C_{44} (GPa)	79.62[a]	68.30[a]	36.20[a]
Permittivities			
ϵ_{r}	11.9[a]	16.2[a]	24.0[a]
Optical energies			
E_{p} (eV)	21.6[a]	26.3[a]	24.0[a]

[a][17],[b][18],[c][19],[d][20], [e][21], [f][10],[g][22], [h][23],[i][24].

Table 3.1: Parameters of Silicon, Germanium, and α-Tin

Table 3.2: Bowing Parameters of SiGe, GeSn, and SiSn alloys for Γ- and L-valley bandgaps.

	SiGe	GeSn	SiSn
b_{L} (eV)	0.169	1.23	0.925
b_{Γ} (eV)	0.21	1.94	13.2

$$E_{\mathrm{g},\eta}(\mathrm{Si}_x\mathrm{Ge}_y\mathrm{Sn}_{1-x-y}) = xE_{\mathrm{g},\eta}(\mathrm{Si}) + yE_{\mathrm{g},\eta}(\mathrm{Ge}) + (1-x-y)E_{\mathrm{g},\eta}(\mathrm{Sn}) - b_\eta^{\mathrm{SiGe}}xy - b_\eta^{\mathrm{SiSn}}x(1-x-y) - b_\eta^{\mathrm{GeSn}}y(1-x-y), \tag{3.7}$$

where b_η^{SiGe}, b_η^{GeSn}, and b_η^{SiSn} are the bowing parameters for SiGe, GeSn, SiSn alloys, respectively; and $\eta(=\Gamma,\mathrm{L})$ refers to different conduction valleys. Those bowing parameters are listed in table 3.2 [25, 26, 27, 28]. Note that the huge bowing parameter of 13.2 eV for SiSn alloys is only valid for Ge-like SiGeSn alloys. Owing to the insufficient experiments of SiSn alloys, the bowing parameter of SiSn alloys for all compositions still remains an open question. Notably, SiGeSn alloys are capable of independently adjusting their energy bandgap and lattice constant. It has been shown that SiGeSn alloys lattice-matched to Ge has a tunable direct-bandgap ranging from 0.8 eV to 1.4 eV [26], which can provide adequate energy barriers for the Ge wells for the spatial confinement of electrons and holes in the Ge wells.

3.5.2 Band lineup

Model-solid theory is a commonly used method to estimate various band lineups in semiconductors [1], [23]. The main idea is to set up an absolute reference energy for all energy bands. By employing an average energy over the three uppermost valence bands, that is, heavy-hole (HH), light-hole (LH), and spin-orbit split-off (SO) bands, to refer as the absolute energy, various bands can be lined up. The model-solid theory can provide a

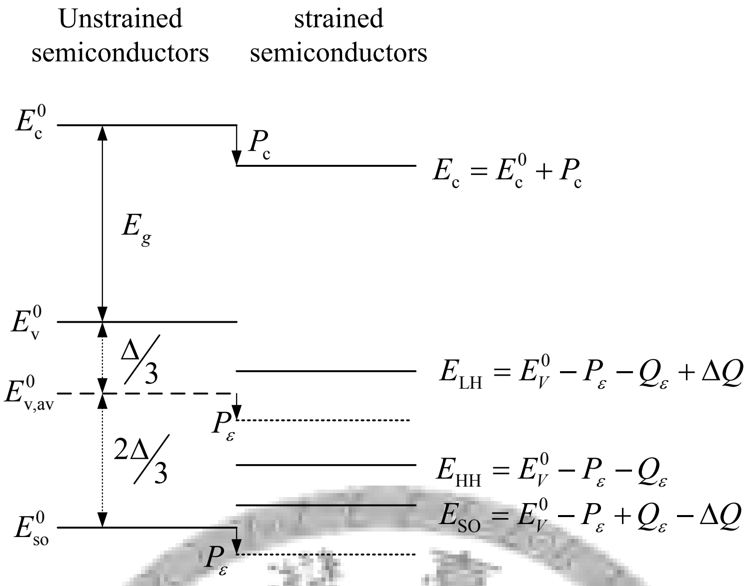

Figure 3.6: Band lineups in the model solid theory for unstrained and strained semiconductors.

simple way with adequate accuracy for estimating various band offsets in semiconductor compounds, especially strained or unstrained heterostructures, quantum wells, and superlattices. Let's consider a cubic-based semiconductor with spin-orbital (SO), light-hole, heavy-hole, and conduction bands, as shown in Fig 3.6. In the absence of strain effects, HH and LH band edges are degenerate. If we define the average valence band energy as $E^0_{\mathrm{v,av}}$, the energy position of the HH and LH band edges is

$$E^0_{\mathrm{v}} = E^0_{\mathrm{v,av}} + \frac{\Delta}{3}, \tag{3.8}$$

where Δ is the spin-orbit splitting energy. The spin-orbit split-off band edge energy E^0_{so} is

$$E^0_{\mathrm{so}} = E^0_{\mathrm{v}} - \Delta = E^0_{\mathrm{v,av}} - \frac{2\Delta}{3}. \tag{3.9}$$

The conduction band edge is obtained by adding an energy gap of E_{g} to the valence band edge

$$E_{\mathrm{c}}^{0} = E_{\mathrm{v}}^{0} + E_{\mathrm{g}}. \tag{3.10}$$

If the semiconductor is subject to a strain field $(\varepsilon_{xx}, \varepsilon_{yy}, \varepsilon_{zz})$. The energy shifts of the conduction band and the average valence band due to the strain effect are

$$\Delta E_{\mathrm{v,av}} = a_{\mathrm{v}}(\varepsilon_{xx} + \varepsilon_{yy} + \varepsilon_{zz}) \equiv -P_{\varepsilon}, \tag{3.11}$$

$$\Delta E_{\mathrm{c}} = a_{\mathrm{c}}(\varepsilon_{xx} + \varepsilon_{yy} + \varepsilon_{zz}) \equiv P_{\mathrm{c}}, \tag{3.12}$$

where a_{c} and a_{v} are the deformation potentials for the Γ-conduction and valence bands, respectively. In addition to the conduction band and average valence band shifts, the relative positions of SO, HH, and LH bands are also changed by the strain effect. Thus, the final energy positions of those bands are

$$E_{\mathrm{c}} = E_{\mathrm{v}}^{0} + E_{\mathrm{g}} + P_{\mathrm{c}}, \tag{3.13}$$

$$E_{\mathrm{HH}} = E_{\mathrm{v}}^{0} - P_{\varepsilon} - Q_{\varepsilon}, \tag{3.14}$$

$$E_{\mathrm{LH}} = E_{\mathrm{v}}^{0} - P_{\varepsilon} + Q_{\varepsilon} + \Delta Q, \tag{3.15}$$

$$E_{\mathrm{SO}} = E_{\mathrm{v}}^{0} - P_{\varepsilon} + Q_{\varepsilon} + \Delta Q, \tag{3.16}$$

$$P_{\varepsilon} = -a_{v}(\varepsilon_{xx} + \varepsilon_{yy} + \varepsilon_{zz}), \tag{3.17}$$

$$Q_{\varepsilon} = -\frac{b_{v}}{2}\left(\varepsilon_{xx} + \varepsilon_{yy} - 2\varepsilon_{zz}\right), \tag{3.18}$$

$$\Delta Q = \frac{1}{2}\left[\sqrt{(\Delta + Q)^{2} + 8Q_{\varepsilon}^{2}} - (\Delta + Q_{\varepsilon})\right], \tag{3.19}$$

where b_{v} is the deformation potential. In the model-solid theory, the bandgap E_{g} and the split-orbit splitting energy Δ are obtained experimentally.

3.5.3 Electronic band structure

Various subband energies and wavefunctions in a quantum well are obtainable by using the effective mass theory under the axial approximation [1]. If a QW is grown on a (001)-oriented substrate with the growth direction along the z direction, the Γ-conduction band can be characterized by a single-band effective-mass Hamiltonian of the envelope function [1]

$$H_{\mathrm{c}}\left(k_{\mathrm{t}}, k_z = -i\hbar\frac{\partial}{\partial z}\right) = -\frac{\hbar^2}{2}\frac{\partial}{\partial z}\frac{1}{m_{\mathrm{c}}}\frac{\partial}{\partial z} + \frac{\hbar^2 k_{\mathrm{t}}^2}{2m_{\mathrm{c}}} + V_{\mathrm{c}}(z) + V_{\mathrm{c},\varepsilon}(z), \tag{3.20}$$

$$V_{\mathrm{c},\varepsilon}(z) = a_c(\varepsilon_{xx} + \varepsilon_{yy} + \varepsilon_{zz}), \tag{3.21}$$

where k_{t} is magnitude of the wave vector perpendicular to the $[001]$ direction; $V_{\mathrm{c}}(z)$ is the unstrained potential energy; and $V_{\mathrm{c},\varepsilon}(z)$ is the potential energy shift due to the strain effect. With the Hamiltonian in Eq. (3.20), the Γ-conduction subband energies and wavefunctions can be obtained by solving the Schrödinger equation [1], [11]

$$H_{\mathrm{c}}\left(k_{\mathrm{t}}, k_z = -i\frac{\partial}{\partial z}\right)\phi_n(k_{\mathrm{t}}, z) = E_n(k_{\mathrm{t}})\phi_n(k_{\mathrm{t}}, z), \tag{3.22}$$

$$E_n(k_{\mathrm{t}}) \approx E_n(k_{\mathrm{t}} = 0) + \frac{\hbar^2 k_{\mathrm{t}}^2}{2m_{n,\mathrm{t}}}, \tag{3.23}$$

$$m_{n,\mathrm{t}} = \left[\int_{-\infty}^{\infty} dz \frac{\left|\phi_n\left(k_{\mathrm{t}} = 0, z\right)\right|^2}{m_{\mathrm{c}}}\right]^{-1}, \tag{3.24}$$

where $E_n(k_{\mathrm{t}})$ is the eigenenergy and $\phi_n(k_{\mathrm{t}})$ is the corresponding eigenfunction of the nth Γ-conduction subband, while $m_{n,\mathrm{t}}$ is the transverse electron effective mass of nth Γ-conduction subband in the plane of WAS. Usually, the eigenfunctions do not change significantly with the wavevector k_{t}, so that it is a good approximation to use $\phi_n(k_{\mathrm{t}} =$

$0, z)$ instead of $\phi_n(k_\mathrm{t}, z)$ later for the calculation of momentum matrix elements.

For group IV semiconductors, there are eight equivalent L-valley conduction bands, but only four of them are located in the first Brillouin zone. For a quantum well grown along the [001] direction, the four valleys are degenerated. Thus, only the band structure of a particular L-conduction valley is needed to be calculated, say the [111] L-valley conduction band. The Hamiltonian of the [111] L-valley conduction band under the effective-mass approximation can be written as [11]

$$\begin{aligned} H_\mathrm{L}^{[111]}(k_1, k_2, k_z = -i\hbar\frac{\partial}{\partial z}) &= -\frac{\hbar^2}{2}\frac{\partial}{\partial z}(\frac{1}{3m_\mathrm{l,L}} + \frac{2}{3m_\mathrm{t,L}})\frac{\partial}{\partial z} \\ &- i\frac{\sqrt{2}\hbar^2 k_1}{6} \times [\frac{\partial}{\partial z}(\frac{1}{m_\mathrm{t,L}} - \frac{1}{m_\mathrm{l,L}}) + (\frac{1}{m_\mathrm{t,L}} - \frac{1}{m_\mathrm{l,L}})\frac{\partial}{\partial z}] \\ &+ (\frac{2}{3m_\mathrm{l,L}} + \frac{1}{3m_\mathrm{t,L}})\frac{\hbar^2 k_1^2}{2} + \frac{\hbar^2 k_2^2}{2m_\mathrm{t,L}} + V^{[111]}(z) + V_\varepsilon^{[111]}(z), \end{aligned} \tag{3.25}$$

$$V_\varepsilon^{[111]} = a_\mathrm{L}(\varepsilon_{xx} + \varepsilon_{yy} + \varepsilon_{zz}), \tag{3.26}$$

$$k_1 = \frac{1}{\sqrt{2}}(k_x + k_y - \frac{2\pi}{a}), \tag{3.27}$$

$$k_2 = \frac{1}{\sqrt{2}}(-k_x + k_y), \tag{3.28}$$

where $m_\mathrm{l,L}$ and $m_\mathrm{t,L}$ are the longitude and transverse electron effective masses along the [111] direction, respectively; $V^{[111]}(z)$ is the unstrained potential energy; $V_\varepsilon^{[111]}$ is the energy shift due to the strain effect; k_1 and k_2 are the magnitudes of the wave vectors along the $[110]$ and $[\bar{1}10]$ directions relative to the minimum energy point of the [111] L-valley conduction band, respectively. The detailed derivation of the Hamiltonian for the [111] L-valley conduction band is described in appendix A. Similarly, the eigenenergy and eigenfunction of the *l*th L-valley conduction subband are obtainable by solving the

Schrödinger equation

$$H_{\mathrm{L}}^{[111]}\left(k_1, k_2, k_z = -i\frac{\partial}{\partial z}\right)\psi_l(k_1, k_2, z) = E_l^{\mathrm{L}}(k_1, k_2)\psi_l(k_1, k_2, z), \tag{3.29}$$

where $E_l^{\mathrm{L}}(k_1, k_2)$ and $\psi_l(k_1, k_2, z)$ are the eigenenergy and engenfunction of the lth L-valley conduction subbannd, respectively.

We adopt the "*J*=4" Luttinger-Kohn Hamiltonian under the axial approximation to calculate the Γ-valence band. The 4×4 block-diagonal Hamiltonian, including the strain effect, is

$$\mathbf{H}_{\mathrm{v,eff}}(k_{\mathrm{t}}, k_z = -i\frac{\partial}{\partial z}) = \begin{bmatrix} \mathbf{H}_{\mathrm{U}} & 0 \\ 0 & \mathbf{H}_{\mathrm{L}} \end{bmatrix}, \tag{3.30}$$

where $\mathbf{H}_{\mathrm{U}}$ and $\mathbf{H}_{\mathrm{L}}$ are the upper and lower blocks of the effective Hamiltonian given as follows

$$\mathbf{H}_{\mathrm{U}} = \begin{bmatrix} V_{\mathrm{v}}(z) - P - Q & -\tilde{R} \\ -\tilde{R}^{+} & V_{\mathrm{v}}(z) - P + Q + \Delta Q \end{bmatrix}, \tag{3.31}$$

$$\mathbf{H}_{\mathrm{L}} = \begin{bmatrix} V_{\mathrm{v}}(z) - P + Q + \Delta Q & -\tilde{R}^{+} \\ -\tilde{R} & V_{\mathrm{v}}(z) - P - Q \end{bmatrix}, \tag{3.32}$$

$$P = P_\varepsilon + \frac{\gamma_1 \hbar^2 k_{\mathrm{t}}^2}{2m_0} - \frac{\hbar^2}{2m_0}\frac{\partial}{\partial z}\gamma_1\frac{\partial}{\partial z}, \tag{3.33}$$

$$Q = Q_\varepsilon + \frac{\gamma_2 \hbar^2 k_{\mathrm{t}}^2}{2m_0} + \frac{\hbar^2}{2m_0}\frac{\partial}{\partial z}\gamma_2\frac{\partial}{\partial z,} \tag{3.34}$$

$$P_\varepsilon = -a_v(\varepsilon_{xx} + \varepsilon_{yy} + \varepsilon_{zz}), \tag{3.35}$$

$$Q_\varepsilon = -\frac{b_v}{2}\left(\varepsilon_{xx} + \varepsilon_{yy} - 2\varepsilon_{zz}\right), \tag{3.36}$$

$$\Delta Q = \frac{1}{2}\left[\sqrt{(\Delta+Q)^2+8Q_\varepsilon^2}-(\Delta+Q_\varepsilon)\right], \tag{3.37}$$

$$\tilde{R} = \frac{\sqrt{3}\hbar^2}{2m_0}\left[\left(\frac{\gamma_2+\gamma_3}{2}\right)k_\mathrm{t}^2 - k_\mathrm{t}\left(\frac{\partial}{\partial z}\gamma_3+\gamma_3\frac{\partial}{\partial z}\right)\right], \tag{3.38}$$

$$\tilde{R}^+ = \frac{\sqrt{3}\hbar^2}{2m_0}\left[\left(\frac{\gamma_2+\gamma_3}{2}\right)k_\mathrm{t}^2 + k_\mathrm{t}\left(\frac{\partial}{\partial z}\gamma_3+\gamma_3\frac{\partial}{\partial z}\right)\right], \tag{3.39}$$

where γ_1, γ_2, and γ_3 are the Luttinger's parameters. Since the effective Hamiltonian $\mathbf{H}_{\mathrm{v,eff}}$ is block-diagonal, the upper and lower Hamiltonians can be solved independently

$$H_\mathrm{U}\begin{bmatrix} g_m^{(1)}(k_\mathrm{t},z) \\ g_m^{(2)}(k_\mathrm{t},z) \end{bmatrix} = E_m^\mathrm{U}(k_\mathrm{t})\begin{bmatrix} g_m^{(1)}(k_\mathrm{t},z) \\ g_m^{(2)}(k_\mathrm{t},z) \end{bmatrix}, \tag{3.40}$$

$$H_\mathrm{L}\begin{bmatrix} g_m^{(3)}(k_\mathrm{t},z) \\ g_m^{(4)}(k_\mathrm{t},z) \end{bmatrix} = E_m^\mathrm{U}(k_\mathrm{t})\begin{bmatrix} g_m^{(3)}(k_\mathrm{t},z) \\ g_m^{(4)}(k_\mathrm{t},z) \end{bmatrix}, \tag{3.41}$$

where $E_m^\mathrm{U}(k_\mathrm{t})$ and $E_m^\mathrm{L}(k_\mathrm{t})$ are the eigenenergies, and $g_m^{(1)}(k_\mathrm{t},z)$, $g_m^{(2)}(k_\mathrm{t},z)$, $g_m^{(3)}(k_\mathrm{t},z)$, and $g_m^{(4)}(k_\mathrm{t},z)$ are the corresponding eigenfunctions for the mth subband in the valence band. Those eigenfunctions will be used for the calculation of the moment matrix elements later. The real eigenfunctions of the "*J=3/2*" Luttinger-Kohn Hamiltonian based on the basis of $|3/2,3/2\rangle$, $|3/2,1/2\rangle$, $|3/2,-1/2\rangle$, and $|3/2,-3/2\rangle$ with eigenenergies $E_m^\mathrm{U}(k_\mathrm{t})$ and $E_m^\mathrm{L}(k_\mathrm{t})$ are also obtainable by the unitary transformation from the eigenfunctions $g_m^{(1)}(k_\mathrm{t},z)$, $g_m^{(2)}(k_\mathrm{t},z)$, $g_m^{(3)}(k_\mathrm{t},z)$, and $g_m^{(4)}(k_\mathrm{t},z)$

$$\overline{\chi}_m^\mathrm{U}(k_\mathrm{t},z) = \begin{bmatrix} \frac{e^{i(3\pi/4-3\phi/2)}}{\sqrt{2}}g_m^{(1)}(k_\mathrm{t},z) \\ -\frac{e^{i(\pi/4-\phi/2)}}{\sqrt{2}}g_m^{(2)}(k_\mathrm{t},z) \\ 0 \\ 0 \end{bmatrix} \begin{array}{c} |3/2,3/2\rangle \\ |3/2,1/2\rangle \\ |3/2,-1/2\rangle \\ |3/2,-3/2\rangle \end{array} \tag{3.42}$$

$$\overline{\chi}^{\mathrm{L}}_m(k_\mathrm{t}, z) = \left[\begin{array}{c} 0 \\ 0 \\ \frac{e^{i(\phi/2-\pi/4)}}{\sqrt{2}} g_m^{(3)}(k_\mathrm{t}, z) \\ \frac{e^{i(3\phi/2-3\pi/4)}}{\sqrt{2}} g_m^{(4)}(k_\mathrm{t}, z) \end{array}\right] \begin{array}{c} |3/2, 3/2\rangle \\ |3/2, 1/2\rangle \\ |3/2, -1/2\rangle \\ |3/2, -3/2\rangle \end{array} \tag{3.43}$$

$$\phi = \arg(\mathbf{k}_\mathrm{t}) \tag{3.44}$$

where ϕ is the azimuthal angle of the wavevector $\mathbf{k}_\mathrm{t}$.

3.5.4 Carrier occupation in the conduction and valence bands

The quasi-Fermi levels F_c and F_v can be determined by the electron concentration n and hole concentration p, which satisfy the charge neutrality condition

$$p + N_\mathrm{D}^+ = n + N_\mathrm{A}^-, \tag{3.45}$$

where N_D^+ and N_A^- are the ionized donor and acceptor concentrations, respectively. Since the Ge wells are heavily n-doped, we assume $N_\mathrm{D}^+ \gg N_\mathrm{A}^-$. Further, the donors in the Ge wells are completely ionized at room temperature since the thermal energy $k_\mathrm{B}T = 25.853\ \mathrm{meV}$ is much larger the donor binding energy about 6.4 meV [29]. For a given injected carrier density N_inj, the electron quasi-Fermi level F_c in the conduction band can be determined by

$$\begin{aligned} n &= N_\mathrm{inj} + N_\mathrm{D}^+ \\ &= \sum_n \frac{k_\mathrm{B}T m_{n,\mathrm{t}}}{\hbar^2 \pi L_\mathrm{w}} \ln\left[\exp\left(\frac{F_\mathrm{c} - E_n}{k_\mathrm{B}T}\right) + 1\right] + \sum_l 8 \frac{1}{(2\pi)^2 L_\mathrm{w}} \int \mathrm{d}\mathbf{k}_\mathrm{t} f_{\mathrm{L},l}(\mathbf{k}_\mathrm{t}), \end{aligned} \tag{3.46}$$

$$f_{\mathrm{L},l}(\mathbf{k}_\mathrm{t}) = \left[\exp\left(\frac{E_l^\mathrm{L}(\mathbf{k}_\mathrm{t}) - F_\mathrm{c}}{k_\mathrm{B}T}\right) + 1\right]^{-1}, \tag{3.47}$$

where T is the temperature; L_w is the well width; $f_{\mathrm{L},l}(\mathbf{k}_\mathrm{t})$ is the Fermi occupation number of the l-th subband in a certain L-conduction valley; and E_l^L is the subband energy of the l-th subband in the L-conduction band. Notice that the factor of eight in the summation for the L conduction subbands in Eq. (3.45) comes from the spin degeneracy of two and four equivalent L-conduction valleys. Similarly, the quasi-Fermi level in the valence band, F_v, can be determined by using

$$p = N_\mathrm{inj} = \sum_{\sigma=\mathrm{U,L}} \sum_m \frac{1}{2\pi L_\mathrm{w}} \int \mathrm{d}k_\mathrm{t} k_\mathrm{t} \left[1 - f_m^\sigma(k_\mathrm{t})\right], \tag{3.48}$$

$$f_m^\sigma(k_\mathrm{t}) = \left[\exp\left(\frac{E_m^\sigma(k_\mathrm{t}) - F_\mathrm{v}}{k_\mathrm{B}T}\right) + 1\right]^{-1}, \tag{3.49}$$

where $f_m^\sigma(k_\mathrm{t})$ is the electron Fermi occupation number in the valence band. The two quasi-Fermi levels help determine the electron and hole distributions in the Γ- and L-conduction subbands as well as those in the valence subbands. For a given n-type doping concentration N_D and an injected carrier density N_inj, the two quasi-Fermi levels can be calculated self-consistently.

3.5.5 Momentum matrix elements and transverse electric and transverse magnetic polarized optical gain from direct transition

To calculate the transverse electric (TE) and transverse magnetic (TM) optical gain spectra, the TE and TM momentum matrix elements have to be determined first. Here the TE (TM) polarization refers to the case that the transverse electric field is polarized perpendicular (parallel) to the [001] direction. For quantum wells, the optical momentum matrix elements are polarization-dependent. By averaging the TE and TM momentum matrix elements in the plane of quantum wells, the average squared TE momentum matrix elements are given by

$$M_{nm}^{\mathrm{U,TE}}(k_\mathrm{t}) = \frac{3}{2}\left|\int_{-\infty}^{\infty} \mathrm{d}z\phi_n^*(z)M_\mathrm{b}g_m^{(1)}(k_\mathrm{t},z)\right|^2 + \frac{1}{2}\left|\int_{-\infty}^{\infty} \mathrm{d}z\phi_n^*(z)M_\mathrm{b}g_m^{(2)}(k_\mathrm{t},z)\right|^2, \tag{3.50}$$

$$M_{nm}^{\mathrm{L,TE}}(k_\mathrm{t}) = \frac{3}{2}\left|\int_{-\infty}^{\infty} \mathrm{d}z\phi_n^*(z)M_\mathrm{b}g_m^{(4)}(k_\mathrm{t},z)\right|^2 + \frac{1}{2}\left|\int_{-\infty}^{\infty} \mathrm{d}z\phi_n^*(z)M_\mathrm{b}g_m^{(3)}(k_\mathrm{t},z)\right|^2, \tag{3.51}$$

$$M_\mathrm{b}^2 = \frac{|\langle S|p_x|X\rangle|^2}{3} = \frac{m_0}{6}E_\mathrm{p}, \tag{3.52}$$

where M_b is the bulk momentum matrix element; and E_p is the optical energy parameter. Here a spin degeneracy of two has been included in the expressions of the average squared momentum matrix elements. Similarly, the average squared TM momentum matrix elements can be written as

$$M_{nm}^{\mathrm{U,TM}}(k_\mathrm{t}) = 2\left|\int_{-\infty}^{\infty} \mathrm{d}z\phi_n^*(z)M_\mathrm{b}g_m^{(2)}(k_\mathrm{t},z)\right|^2, \tag{3.53}$$

$$M_{nm}^{\mathrm{L,TM}}(k_\mathrm{t}) = 2\left|\int_{-\infty}^{\infty} \mathrm{d}z\phi_n^*(z)M_\mathrm{b}g_m^{(3)}(k_\mathrm{t},z)\right|^2. \tag{3.54}$$

Note that the TE momentum matrix elements have a stronger dependence on the heavy-hole (HH) components, $g_m^{(1)}(k_\mathrm{t},z)$ and $g_m^{(4)}(k_\mathrm{t},z)$, than the light-hole (LH) components, $g_m^{(2)}(k_\mathrm{t},z)$ and $g_m^{(3)}(k_\mathrm{t},z)$, while the TM momentum matrix elements depend on only the

LH components. Therefore the TE gain will be dominant if the highest valence band is HH-like, while the TM gain will be dominant if the highest valence band is LH-like. With the TE and TM momentum matrix elements determined, we can calculate the corresponding TE and TM material gain spectra based on the spontaneous emission transformation method, taking into account the homogenous broadening by the Lorentzian function with a full-width-at-half-maximum (FWHM) linewidth, Γ [30], [31]

$$\begin{aligned} g_{\mathrm{w}}^{\mathrm{TE}}(\hbar\omega) &= \frac{\pi}{n_{\mathrm{r}} c \varepsilon_0 L_{\mathrm{w}}} \left(\frac{e}{m_0}\right)^2 \left[1 - \exp\left(\frac{\hbar\omega - \Delta F}{k_{\mathrm{B}} T}\right)\right] \\ &\times \sum_{\sigma=\mathrm{L,U}} \sum_{n,m} \int_0^\infty \frac{\mathrm{d}k_{\mathrm{t}}}{2\pi} k_{\mathrm{t}} M_{nm}^{\sigma,\mathrm{TE}}(k_{\mathrm{t}}) \frac{f_n(k_{\mathrm{t}}) \left[1 - f_m^\sigma(k_{\mathrm{t}})\right] \Gamma/(2\pi)}{\left[E_n(k_{\mathrm{t}}) - E_m^\sigma(k_{\mathrm{t}}) - \hbar\omega\right]^2 + (\Gamma/2)^2}, \end{aligned} \tag{3.55}$$

$$\begin{aligned} g_{\mathrm{w}}^{\mathrm{TM}}(\hbar\omega) &= \frac{\pi}{n_{\mathrm{r}} c \varepsilon_0 L_{\mathrm{w}}} \left(\frac{e}{m_0}\right)^2 \left[1 - \exp\left(\frac{\hbar\omega - \Delta F}{k_{\mathrm{B}} T}\right)\right] \\ &\times \sum_{\sigma=\mathrm{L,U}} \sum_{n,m} \int_0^\infty \frac{\mathrm{d}k_{\mathrm{t}}}{2\pi} k_{\mathrm{t}} M_{nm}^{\sigma,\mathrm{TM}}(k_{\mathrm{t}}) \frac{f_n(k_{\mathrm{t}}) \left[1 - f_m^\sigma(k_{\mathrm{t}})\right] \Gamma/(2\pi)}{\left[E_n(k_{\mathrm{t}}) - E_m^\sigma(k_{\mathrm{t}}) - \hbar\omega\right]^2 + (\Gamma/2)^2}, \end{aligned} \tag{3.56}$$

where e is the elementary charge, c is the speed of light in free space, ε_0 is the permittivity of free space, $\Delta F = F_{\mathrm{c}} - F_{\mathrm{v}}$ is the quasi-Fermi level separation, $\hbar\omega$ is the photon energy, and n_{r} is the background refractive index.

3.5.6 Free-carrier absorption

Because the Ge wells are heavily n-doped, the free-carrier absorption may be significant, and it has to be taken into account to predict the threshold of this MQW laser. The free-carrier absorption, including the contribution form the L-conduction valleys, can be described by the Drude-Lorentz equation [32]

$$\alpha_{\mathrm{f}} = \frac{e^3\lambda^2}{4\pi^2 c^3 \varepsilon_0 n_{\mathrm{r}}} \left[\frac{n_\Gamma}{\mu_\Gamma \left(m_{\mathrm{c}}^*\right)^2} + \frac{n_{\mathrm{L}}}{\mu_{\mathrm{L}} \left(m_{\mathrm{L}}^*\right)^2} + \frac{p}{\mu_{\mathrm{p}} \left(m_{\mathrm{h}}^*\right)^2} \right], \tag{3.57}$$

where n_Γ and n_{L} are the volume electron densities in the Γ- and L-conduction valleys, respectively; m_{c}^* and m_{L}^* are the electron effective masses of the Γ- and L-conduction valleys, respectively; m_{h}^* is the hole effective mass of the valance band; μ_{L} and μ_Γ are the electron mobilities in the L- and Γ-conduction valleys, respectively; μ_{h} is the hole mobility in the valence band; and λ is the free space wavelength. Notice that the mobility is carrier-concentration-dependent. The electron mobility in the L-conduction valleys of Ge at room temperature is given by [33]

$$\mu_{\mathrm{L}} = \frac{\mu_{\mathrm{L0}}}{1 + \sqrt{n_{\mathrm{L}} \times 10^{-17}}}, \tag{3.58}$$

where $\mu_{\mathrm{L0}} = 3900\ \mathrm{cm}^2\mathrm{V}^{-1}\mathrm{s}^{-1}$ [29] and n_{L} is in the unit of cm^{-3}. The electron mobility in the Γ-conduction valley of Ge is still unavailable in the literature. However, the carrier mobility is related to the carrier effective mass m^* and the scattering time τ by $\mu = q\tau/m^*$. If assuming the scattering times τ for the electrons in the L- and Γ- conduction valleys are the same, we can simply estimate the electron mobility in the Γ-conduction valley from that in the L-conduction valleys. For the holes in the valence band, we obtain the hole mobility of Ge in the range of $10^{18} - 10^{20}\mathrm{cm}^{-3}$ at room temperature by fitting the experimental data [29]

$$\mu_{\mathrm{p}} = \frac{\mu_{\mathrm{p0}}}{1 + \sqrt{p \times 2.1 \times 10^{-17}}}, \tag{3.59}$$

where $\mu_{\mathrm{p0}} = 1900\ \mathrm{cm^2V^{-1}s^{-1}}$ [29] and p is in the unit of $\mathrm{cm^{-3}}$. Based on Eqs. (3.57), (3.58), and (3.59), several important characteristics for the free-carrier absorption should be pointed out. First, the free-carrier absorption is proportional to λ^2 [34], so it becomes significant at long wavelengths. Second, at a high doping concentration, the free-carrier absorption is proportional to $n^{3/2}$, which agrees well with the experimental results [35]. Last, the free-carrier absorption is inversely proportional to the effective mass squared, indicating that the free-carrier absorption will be significant if the carriers have a small effective mass.

3.5.7 Modal gain, optical confinement factor, and threshold lasing condition

The modal gain and threshold modal gain are two key parameters which characterize laser performance. The former describes the available optical gain for guided modes in a laser cavity, while the later stands for the required modal gain to overcome the background losses and radiation losses for lasing action to take place. We also need to convert the material gain to the modal gain using the optical confinement factor, since different modes experience different amount of optical gain. In addition, because optical gain in semiconductors are highly anisotropic, we need two optical confinement factors for the modal gain to properly specify the contributions from the TE and TM material gains. The general expression of the modal gain G_{mod} for a MQW laser with N_{w} wells can be expressed as [36, 37, 38]

$$G_{\mathrm{mod}} = N_{\mathrm{w}}\Gamma_{\mathrm{w}}^{\mathrm{TE}} g_{\mathrm{w}}^{\mathrm{TE}}(\hbar\omega) + N_{\mathrm{w}}\Gamma_{\mathrm{w}}^{\mathrm{TM}} g_{\mathrm{w}}^{\mathrm{TM}}(\hbar\omega), \tag{3.60}$$

where $\Gamma_{\mathrm{w}}^{\mathrm{TE}}$ and $\Gamma_{\mathrm{w}}^{\mathrm{TM}}$ are the TE and TM optical confinement factors per well of guided modes, respectively; and $g_{\mathrm{w}}^{\mathrm{TE}}$ and $g_{\mathrm{w}}^{\mathrm{TM}}$ are the TE and TM material gains per well, respectively. If a guided mode propagates in the x direction and the crystal growth direction is along the z direction, the TE and TM optical confinement factors for the well are

$$\Gamma_{\mathrm{w}}^{\mathrm{TE}} = \frac{\frac{n_{\mathrm{w}}}{2\eta_0}\int\int_{\mathrm{w}}\left(|E_x|^2 + |E_y|^2\right)dydz}{\frac{1}{2}\int_{-\infty}^{\infty}\int_{-\infty}^{\infty}\mathrm{Re}[\mathbf{E}\times\mathbf{H}^*]\cdot\hat{x}dydz}, \tag{3.61}$$

$$\Gamma_{\mathrm{w}}^{\mathrm{TM}} = \frac{\frac{n_{\mathrm{w}}}{2\eta_0}\int\int_{\mathrm{w}}|E_z|^2 dydz}{\frac{1}{2}\int_{-\infty}^{\infty}\int_{-\infty}^{\infty}\mathrm{Re}[\mathbf{E}\times\mathbf{H}^*]\cdot\hat{x}dydz}, \tag{3.62}$$

where n_{w} is the refractive index; and $\eta_0 = \sqrt{\mu_0/\varepsilon_0}$ is the intrinsic impedance. On the other hand, since the material loss attributed from the free-carrier absorption is isotropic, we need only one optical confinement factor $\Gamma_i = \Gamma_i^{\mathrm{TE}} + \Gamma_i^{\mathrm{TM}}$, which is the sum of the TE and TM optical confinement factors, for layer i to calculate the modal loss. If we assume that the free-carrier absorption due to the total electron density n occurs in the well region, the modal loss $\alpha(n)$ taking into account the absorption losses in the n- and p-contacts can be expressed as

$$\alpha(n) = N_{\mathrm{w}}\Gamma_{\mathrm{w}}\alpha_{\mathrm{w}}(n) + \Gamma_{\mathrm{p}}\alpha_{\mathrm{p}} + \Gamma_{\mathrm{n}}\alpha_{\mathrm{n}}, \tag{3.63}$$

$$\Gamma_i = \frac{\frac{n_{\mathrm{i}}}{2\eta_0}\int\int_{\mathrm{i}}|\mathbf{E}|^2 dydz}{\frac{1}{2}\int_{-\infty}^{\infty}\int_{-\infty}^{\infty}\mathrm{Re}[\mathbf{E}\times\mathbf{H}^*]\cdot\hat{x}dydz}, \tag{3.64}$$

where $\alpha_{\mathrm{w}}(n)$ is the absorption loss for one well; α_{n} and α_{p} are the absorption losses for the n-contact and p-contact regions, respectively; and Γ_{n} and Γ_{p} are the optical confinement factors of the n-contact and p-contact regions, respectively.

With the modal loss defined, it is sufficient to determine the threshold modal gain. For a Fabry-Pérot laser with a cavity length of L, the required modal gain at the threshold

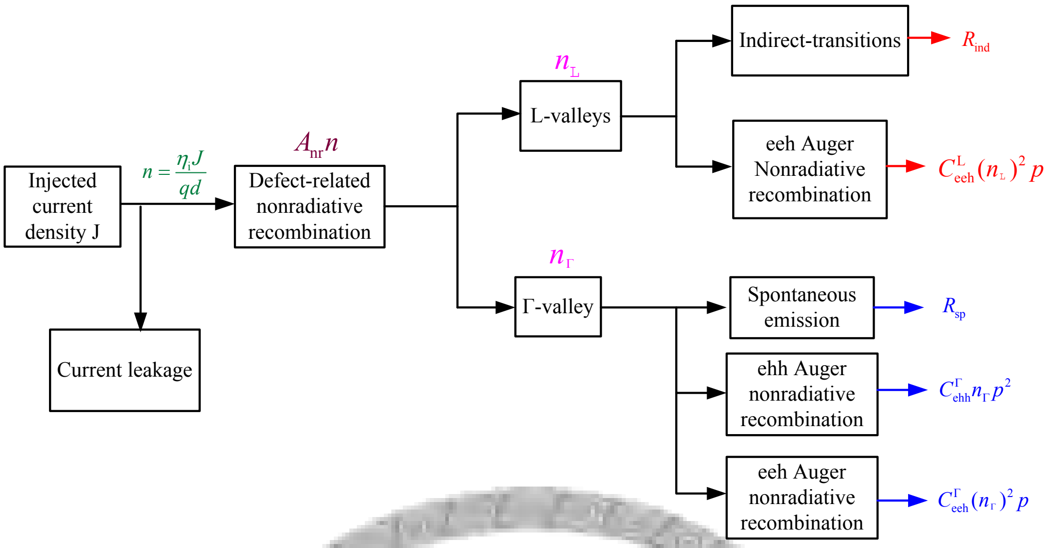

Figure 3.7: Carrier utilization below threshold in the n-doped, tensile-strained Ge WAS with $\text{Si}_x\text{Ge}_y\text{Sn}_{1-x-y}$ barriers.

lasing condition is

$$G_{\text{th}} = \alpha(n) + \frac{1}{2L}\ln\frac{1}{R_1R_2}, \tag{3.65}$$

where R_1 and R_2 are the reflectivities at the two facets of the cavity. Once the modal gain in Eq. (3.59) reaches the threshold modal gain in Eq. (3.64), lasing action can take place.

Figure 3.7 shows the carrier utilization below threshold for the n-doped, tensile-strained Ge/$\text{Si}_x\text{Ge}_y\text{Sn}_{1-x-y}$ QW lasers. The L-valley effects are also included. Below threshold condition, the stimulated emission rate is still too small to be considered and the relationship between the carrier density and the current density is

$$J_{\text{th}} = \frac{qN_{\text{w}}L_{\text{w}}}{\eta_{\text{i}}}\left[A_{\text{nr}}n + R_{\text{sp}} + (C^{\Gamma}_{\text{eeh}}n_{\Gamma} + C^{\Gamma}_{ehh}p)(n_{\Gamma}p) + R_{\text{ind}} + C^{\text{L}}_{eeh}n^2_{\text{L}}p\right] \tag{3.66}$$

where η_{i} is the injection quantum efficiency; A_{nr} is the nonradiative recombination rate; R_{sp} is the spontaneous rate per unit volume; C^{Γ}_{eeh} and C^{Γ}_{ehh} are the Auger recombination coefficients for electrons in the Γ conduction band and valence band, respectively; $C^{\text{L}}_{\text{eeh}}$ is the Auger recombination coefficient for electrons in the L conduction band, R_{ind} is the indirect transition rate per unit volume, and n_{v} is the volume carrier density. The total spontaneous emission rate per unit volume R_{sp} $(\mathrm{s}^{-1}\mathrm{cm}^{-3})$ can be rigourously calculated by [31], [39]

$$R_{\mathrm{st}} = \int_0^\infty r^{\mathrm{spon}}(\hbar\omega)\mathrm{d}\hbar\omega \tag{3.67}$$

$$r_{\mathrm{spon}} = \frac{n_{\mathrm{e}}^2\omega^2}{\pi^2\hbar c^2}\left(\frac{2g_{\mathrm{sp}}^{\mathrm{TE}} + g_{\mathrm{sp}}^{\mathrm{TM}}}{3}\right) \tag{3.68}$$

$$\begin{aligned} g_{\mathrm{sp}}^{\mathrm{TE}}(\hbar\omega) =& \frac{2\pi e^2}{n_{\mathrm{r}}c\varepsilon_0 m_0^2\omega L_{\mathrm{w}}} \times \sum_{\sigma=\mathrm{L,U}}\sum_{n,m}\int_0^\infty \frac{\mathrm{d}k_{\mathrm{t}}}{2\pi}k_{\mathrm{t}}M_{nm}^{\sigma,\mathrm{TE}}(k_{\mathrm{t}}) \\ & \frac{f_n(k_{\mathrm{t}})\left[1 - f_m^\sigma(k_{\mathrm{t}})\right]\Gamma/(2\pi)}{\left[E_n(k_{\mathrm{t}}) - E_m^\sigma(k_{\mathrm{t}}) - \hbar\omega\right]^2 + (\Gamma/2)^2}, \end{aligned} \tag{3.69}$$

$$\begin{aligned} g_{\mathrm{sp}}^{\mathrm{TM}}(\hbar\omega) =& \frac{2\pi e^2}{n_{\mathrm{r}}c\varepsilon_0 m_0^2\omega L_{\mathrm{w}}} \times \sum_{\sigma=\mathrm{L,U}}\sum_{n,m}\int_0^\infty \frac{\mathrm{d}k_{\mathrm{t}}}{2\pi}k_{\mathrm{t}}M_{nm}^{\sigma,\mathrm{TM}}(k_{\mathrm{t}}) \\ & \frac{f_n(k_{\mathrm{t}})\left[1 - f_m^\sigma(k_{\mathrm{t}})\right]\Gamma/(2\pi)}{\left[E_n(k_{\mathrm{t}}) - E_m^\sigma(k_{\mathrm{t}}) - \hbar\omega\right]^2 + (\Gamma/2)^2}, \end{aligned} \tag{3.70}$$

where $r_{\mathrm{sp}}(\hbar\omega)$ is the total spontaneous rate per unit volume per unit energy interval $(\mathrm{s}^{-1}\mathrm{cm}^{-3}\mathrm{eV}^{-1})$

3.6 Theoretical results and discussions

Figure 3.8 shows the potential profiles of various bands of the n-type doped, tensile-strained Ge/$\mathrm{Si}_{0.2}\mathrm{Ge}_{0.7}\mathrm{Sn}_{0.1}$ quantum-well structure. The zero energy is set at the top of the LH band of the well. Because both the Γ-conduction minimum and valence band maximum are located in the well region, this Ge/$\mathrm{Si}_{0.2}\mathrm{Ge}_{0.7}\mathrm{Sn}_{0.1}$ quantum-well has a type-I alignment. For the Ge well, the band edge of the LH band is shifted upward while

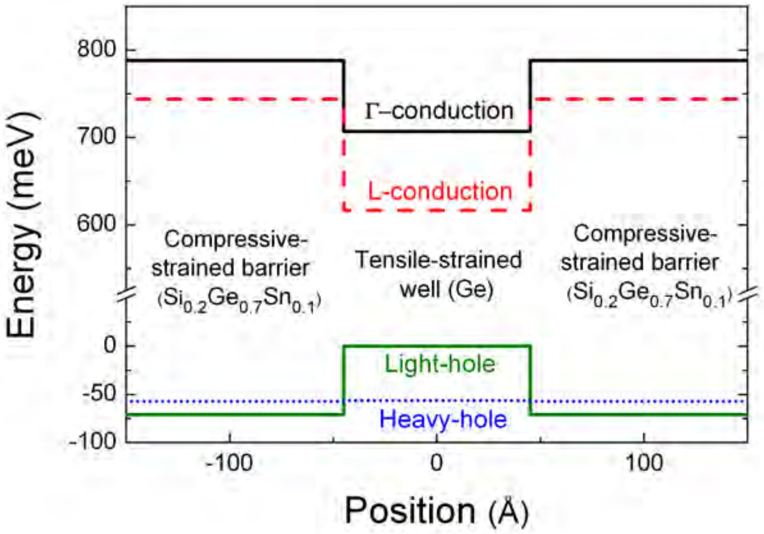

Figure 3.8: Potential profiles of various bands. In the Ge well region, the 0.514% tensile strain reduces the energy difference between the Γ- and L-conduction band edges to 91.5 meV. In the valence band, the LH band edge is lifted and HH band edge is lowered due to the tensile strain.

that of the HH band is shifted downward due to the tensile strain. Meanwhile, for the $\mathrm{Si_{0.2}Ge_{0.7}Sn_{0.1}}$ barriers, the shift directions of the LH and HH bands are opposite to those of the Ge well due to the compressive strain. As a result, the highest valence subband in the Ge well is LH-like and there is no bounded HH-like state. This is owing to that the tensile strain lowers the HH band edge so that the potential profile in the barrier region is higher than that of the Ge QW.

Figure 3.9(a) shows the dispersion relations of the Γ-conduction subband and valence subbands for the Ge well under the axial approximation. Only one quantized Γ-conduction subband and one LH subband exist, indicating that there is only one interband transition (CΓ1-LH1 transition) in the Ge well. The dispersion relation of the LH1 subband changes slowly with k_t due to the larger in-plane effective mass, leading to a significant hole accumulation under carrier injection. Figure 3.9(b) shows the dispersion relation of the first [111] L-conduction subband along the $[110]$ and $[\bar{1}10]$ directions. Because the energy surface of the L-conduction band is anisotropic, the dispersion relations

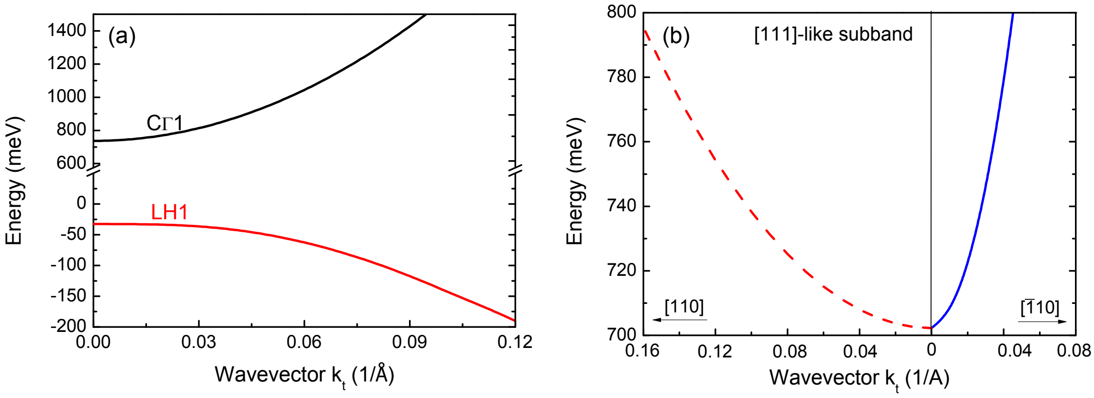

Figure 3.9: (a) Dispersion relations of the Γ-conduction and valence subbands for the Ge well. Because of the tensile strain, there is only one quantized LH subband in this Ge/Si$_{0.2}$Ge$_{0.7}$Sn$_{0.1}$ QW. (b) Dispersion relation of the lowest [111] L-conduction subband, showing that the dispersion relation varies along different directions due to the anisotropic energy surface.

are different along the different directions. Compared with the dispersion relations of the Γ-conduction and valence subbands as shown in Fig. 3.9(a), the L-conduction subband shows a slow-varying dispersion relation along the $[110]$ direction, representing a significant density of states. Together with the four equivalent L-conduction valleys, the significant density of states of the L-conduction subbands are very important for carrier occupation under carrier injection.

Figure 3.10 shows the surface carrier densities of the Γ- and L-conduction subbands as a function of the total injected surface carrier density for the 0.514% tensile-strained Ge/Si$_{0.2}$Ge$_{0.7}$Sn$_{0.1}$ QW with an n-type doping concentration of $2.14 \times 10^{19}\mathrm{cm}^{-3}$, compared with those of an intrinsic, strain-free Ge QW with Si$_{0.15}$Ge$_{0.81}$Sn$_{0.04}$ barriers. The well and barrier widths are 70Å and 200Å for both cases. The injected surface carrier density $N_{\mathrm{inj}}^{\mathrm{s}}$ is related to the total injected volume carrier density N_{inj} by $N_{\mathrm{inj}}^{\mathrm{s}} = N_{\mathrm{inj}} L_{\mathrm{w}}$. For the intrinsic, strain-free Ge QW, almost all of the injected carriers leak to the L-conduction band, and only less than 0.05% injected electrons can populate the direct Γ-conduction band because the L-conduction band is 134.5 meV lower the Γ-conduction band. Thus, population inversion is not achievable in strain-free Ge WAS to produce op-

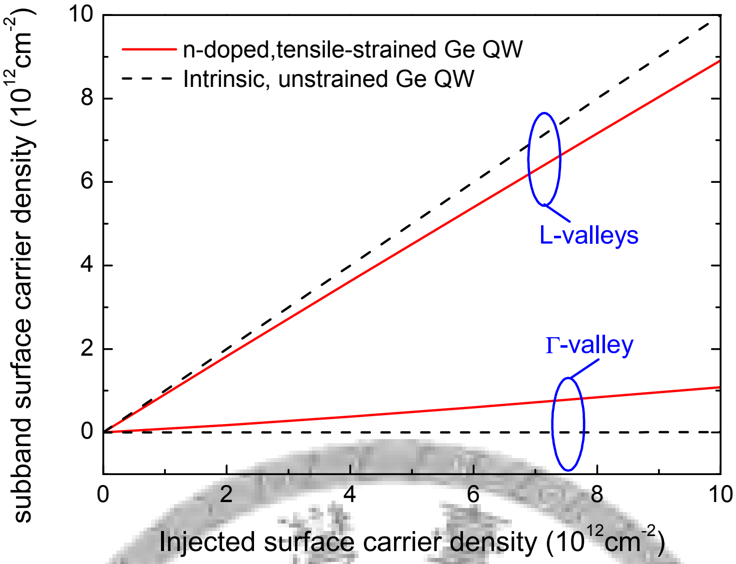

Figure 3.10: Surface carrier densities of the Γ- and L-conduction valleys as a function of the total injected surface carrier density $N_{\rm inj}^{\rm s}$ for an intrinsic, unstrained Ge QW and an n-type doped, tensile-strained Ge QW.

tical gain. On the other hand, in the tensile-strained, n-type doped Ge QW, about 9% injected carriers can populate the Γ-conduction subband. Those carriers injected to the Γ-conduction subband can radiatively recombine with holes via the direction transition and produce significant optical gain. However, because of the larger electron effective mass and four equivalent valleys of the L-conduction valleys, the carrier occupation of the L-conduction valleys outnumbers that of the Γ-conduction valley. Since those carriers in the L-conduction valleys do not contribute to the optical gain through the direct transition, the carrier leakage to the L-conduction band becomes important to this MQW laser.

Figure 3.11 shows the TE and TM squared normalized momentum matrix elements $M_{nm}^{\sigma,\rm TE}/M_{\rm b,Ge}^2$ and $M_{nm}^{\sigma,\rm TM}/M_{\rm b,Ge}^2$ as a function of the wave vector $k_{\rm t}$, where $M_{\rm b,Ge}$ is the bulk momentum matrix element of Ge. Because only one LH subband exists, the TM magnitude is about four times larger than the TE magnitude. When the wave vector $k_{\rm t}$ increases, the TM component always decreases due to less wave function overlap. On

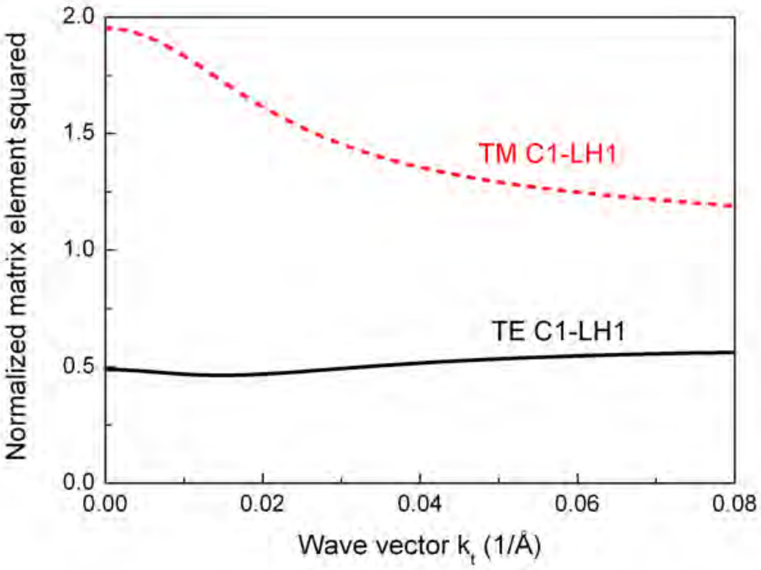

Figure 3.11: TE and TM normalized squared magnitudes of the momentum matrix elements. Because only one LH subband exists, the TM component is about four times larger than that of the TE component.

the other hand, the TE magnitude slightly increases at a high wave vector k_{t} due to the valence-band-mixing effect.

Figure 3.12 shows the TE and TM material gain spectra under varying injected surface carrier densities $N_{\mathrm{inj}}^{\mathrm{s}}$. The FWHM linewidth of the Lorentzian function is set to 20 meV. Because the magnitude of the TM momentum matrix element is about four times larger than that of the TE one, the magnitude of the TM gain is also about four times larger than that of the TE gain. It means that the TM-polarized light is dominant in this MQW laser. As the number of injected carriers increases, both the TE and TM gains increase but tend to saturate. The peak gain is close to 0.8 eV, corresponding to an emission wavelength of 1.55 $\mu\mathrm{m}$. In this calculation, the bandgap shrinkage due to the heavily n doping is not included. However, the amounts of the indirect- and direct-bandgap shrinkages due to n doping at room temperature are almost the same [40], so it does not qualitatively influence the calculation results except for the red shift of the gain spectra. However, this red shift can be compensated by adjusting the well width. By decreasing the well width, the gain

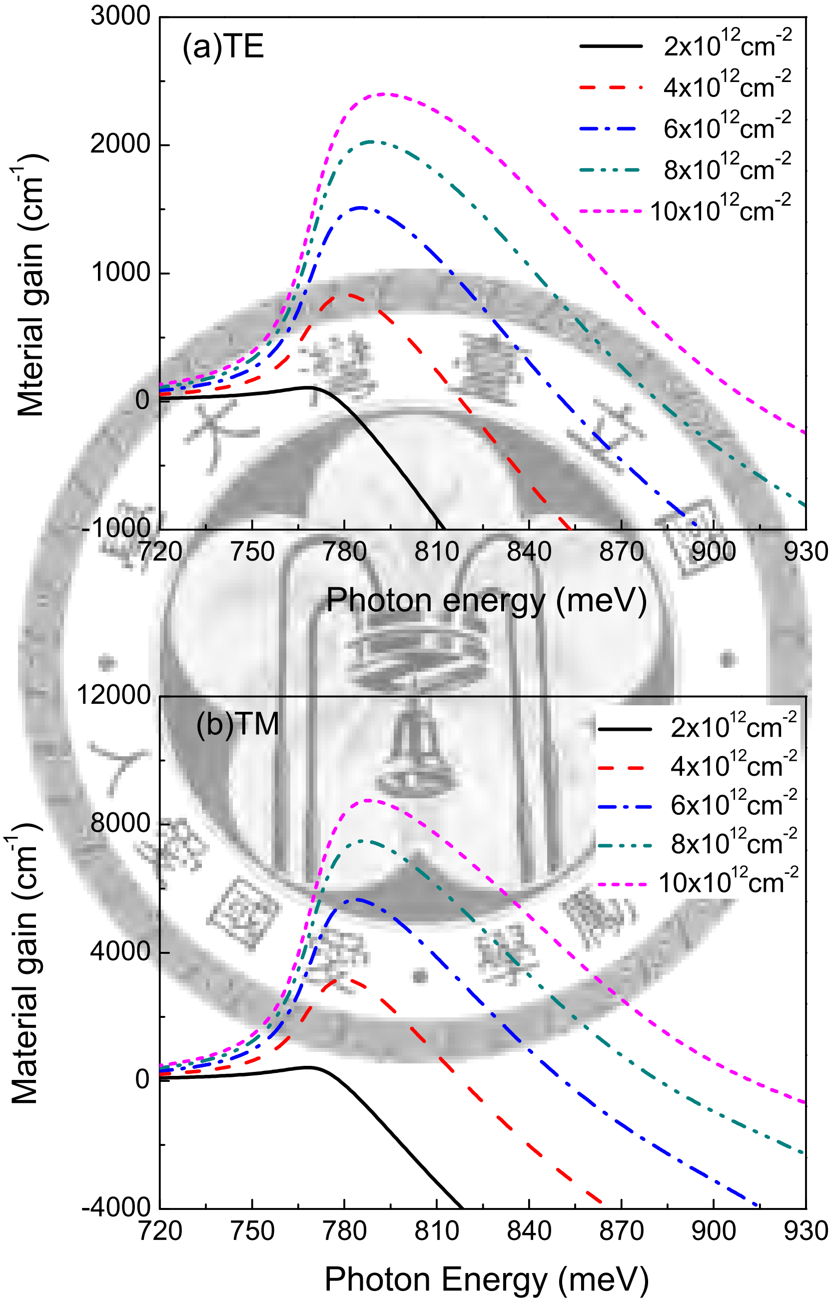

Figure 3.12: (a) TE and (b) TM material gain spectra at different injected surface carrier density $N^{\mathrm{s}}_{\mathrm{inj}}$.

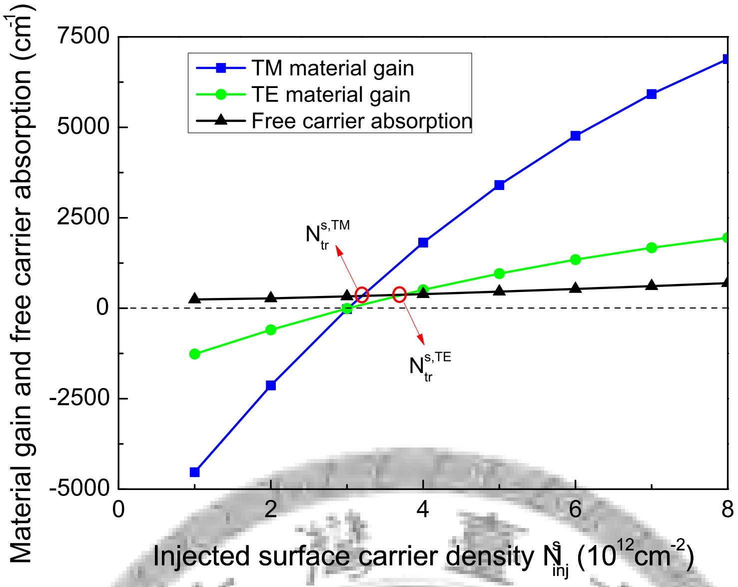

Figure 3.13: TE material gain, TM material gain, and free-carrier absorption per Ge well as a function of the injected surface carrier density. The transparency carrier densities for TE and TM polarizations are indicated.

spectra will be blue-shifted to cancel the influence of the bandgap shrinkage effects caused by the heavy n doping to maintain the peak gain around 0.8 eV for telecommunication applications.

Figure 3.13 shows the TE and TM material gains per quantum well from the direct transition and the free-carrier absorption (an n-doped, tensile strained Ge-well structure with a doping concentration $N_\mathrm{D} = 2.14 \times 10^{19}\ \mathrm{cm}^{-3}$) as a function of the injected surface carrier density $N^\mathrm{s}_\mathrm{inj}$ at $\lambda = 1550$ nm. As mentioned earlier, the free-carrier absorption is a function of the carrier concentration and the carrier effective mass. In the conduction band, due to the less electron occupation and the larger electron mobility of the Γ-conduction subbands than those of the L-conduction subbands, the free-carrier absorption from electrons in the Γ-conduction subbands is much smaller than that from the L-conduction subbands. In the valence band, because only one bounded LH state exists, and its effective mass is very small ($m_\mathrm{lh} = 0.043\ m_0$ for Ge), the free-carrier absorption for

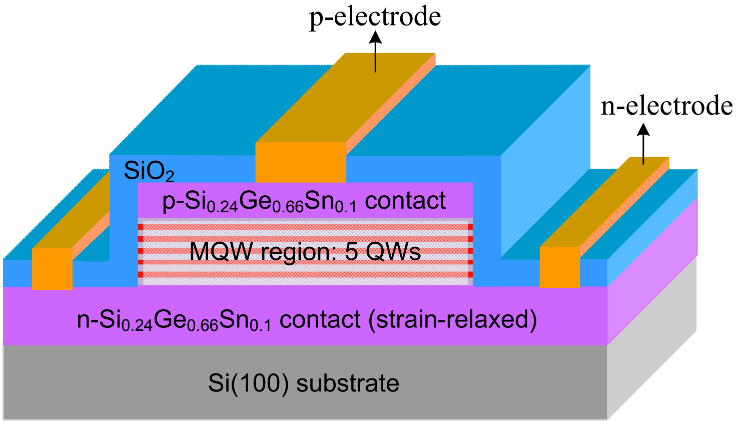

Figure 3.14: Schematic diagram of our designed silica ridge waveguide structure for index guidance. The silica ridge structure has a small refractive index and can provide a proper optical confinement for the active region.

Table 3.3: Doping concentrations, optical confinement factors of the quasi-TM fundamental mode, and absorption losses in various regions.

	n$^+$-wells	n-contact	p-contact
Doping concentration (cm^{-3})	2.14×10^{19}	5×10^{18}	1×10^{19}
Optical confinement factor Γ_i^{TE} (%)	0.0227	0.1.0685	1.4997
Optical confinement factor Γ_i^{TM} (%)	5.8689	51.3845	19.8612
Optical confinement factor Γ_i (%)	5.8917	52.4430	21.3609
Free-carrier absorption α_{f} (cm^{-1})	199.72	14.47	35.62

holes in the valance band becomes significant at a high injected carrier density. The intersection between the material gain and the free-carrier absorption gives the transparency carrier density for the Ge well. The Ge well becomes transparent for TM polarization at an injected surface carrier density of about $3.19 \times 10^{12}\ \mathrm{cm}^{-2}$ (or an injected volume carrier density of $4.55 \times 10^{18}\ \mathrm{cm}^{-3}$), while the transparency carrier density for TE polarization is $3.70 \times 10^{12}\ \mathrm{cm}^{-2}$ (or a injected volume carrier density of $5.28 \times 10^{18}\ \mathrm{cm}^{-3}$). A net TM material gain of about $6192\ \mathrm{cm}^{-1}$ at $\lambda = 1550\ \mathrm{nm}$ is obtainable at an injected surface carrier density of $8 \times 10^{12}\mathrm{cm}^{-2}$.

Another important concern is that the high refractive index of α-Sn $(n_{\mathrm{Sn}} = 4.885)$ [22] compared with those of Si $(n_{\mathrm{Si}} = 3.4784)$ [10] and Ge $(n_{\mathrm{Ge}} = 4.275)$ [11] at $\lambda = 1550\ \mathrm{nm}$. The high composition of α-Sn in Si$_x$Ge$_y$Sn$_{1-x-y}$ compounds leads to

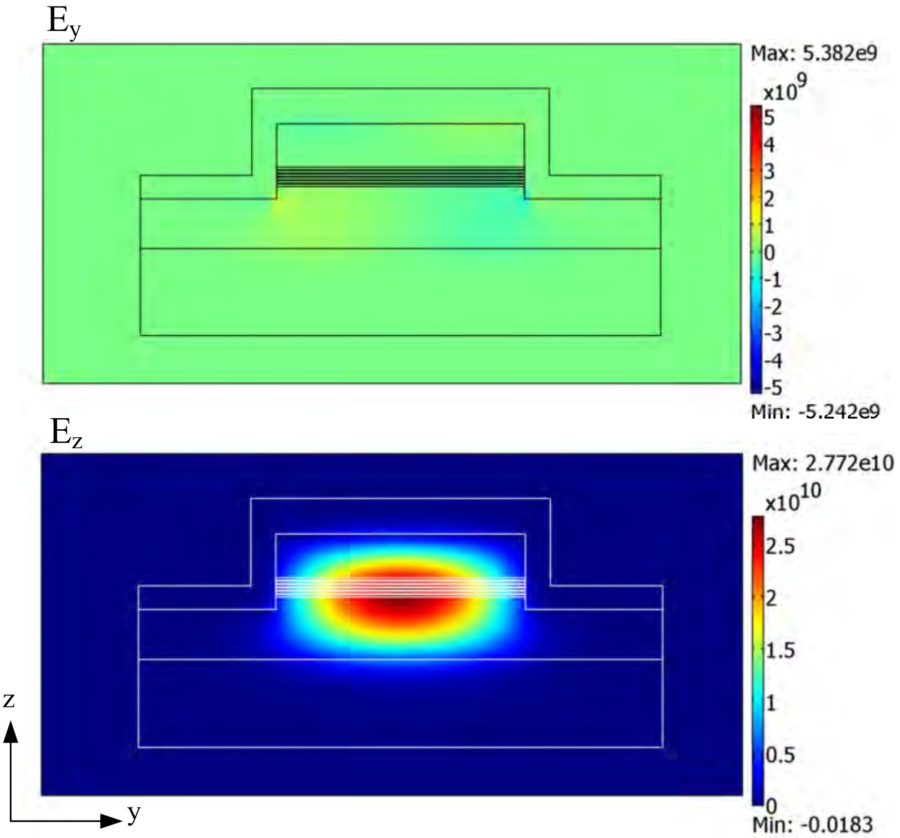

Figure 3.15: Transverse electric field distributions of the quasi-TM fundamental mode. The dominant transverse electric field is E_z with its peak located at the active region, leading to a high TM optical confinement factor of 5.8689% in the Ge wells.

the situation that the refractive index of the Ge well is slightly larger than that of the p-$\mathrm{Si_{0.24}Ge_{0.66}Sn_{0.1}}$ and n-$\mathrm{Si_{0.24}Ge_{0.66}Sn_{0.1}}$ contacts. It means that the n- and p-contacts cannot provide proper optical confinements for the active region. To confine light properly, we design a silica ridge waveguide structure, which has a smaller refractive index $n_{\mathrm{SiO_2}} = 1.45$, for index guidance, as shown in Fig. 3.14. The width of the ridge structure is set to 2 $\mu\mathrm{m}$. We use the finite element method (FEM) to calculate the field distributions of the guided modes. Since the TM-polarized gain is dominant in this MQW laser, this MQW laser is likely to lase with the TM-like modes. Figure 3.15 shows the transverse electric field distributions for the quasi-TM fundamental mode. The cap layer thickness is optimized to $350\ \mathrm{nm}$ to maximize the TM optical confinement factor for the wells.

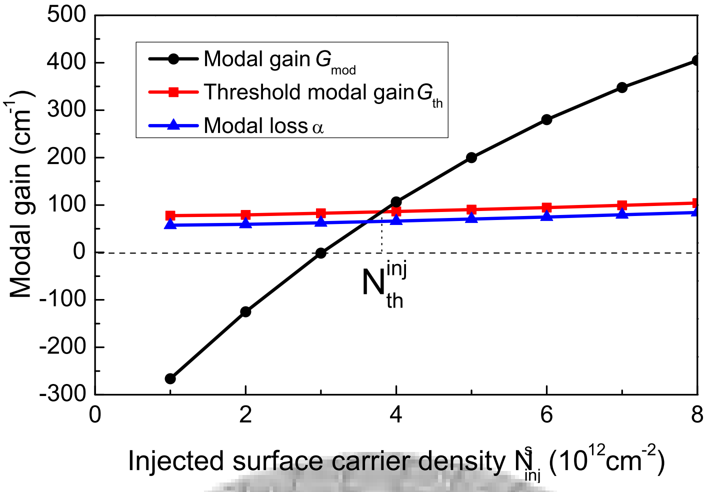

Figure 3.16: Modal gain, modal loss, and threshold modal gain for the quasi-TM fundamental mode as a function of the injected surface carrier density N^{s}_{inj}. The modal gain can reach the threshold modal gain at a reasonable threshold surface carrier density to make the device lase.

Clearly, the E_z field is the dominant transverse electric field for the quasi-TM fundamental mode. Besides, the silica ridge structure provides the upper cladding while the silicon substrate acts as a lower cladding for the waveguide. As a result, Table 3.3 tabulates the doping concentrations, the optical confinement factors, and the absorption losses of the n^{+}-well, n-contact, and p-contact regions, respectively. The TM optical confinement factors are much larger than the TE components for the quasi-TM fundamental mode due to the weak waveguiding. Meanwhile, because of the proper waveguide design, the TM optical confinement factor in the Ge wells is as high as 5.89%, leading to an improved stimulated emission process in the active region. Although the optical confinement factors of n- and p-contacts are much larger than that of the Ge wells, the absorption-losses in the n- and p-contacts are much smaller in contrast to the material gain generated by the Ge wells, resulting in very little modal losses in the n- and p-contact regions.

We then estimate the threshold carrier density, which is one of the most important parameters for a working device. Figure 3.16 shows the modal gain, the modal loss, and the threshold modal gain as a function of the injected surface carrier density $N^{\mathrm{s}}_{\mathrm{inj}}$, where the reflectivities $R_1 = R_2 = 0.368$ are obtained form the waveguide analysis; and the mirror loss is $19.97\ \mathrm{cm}^{-1}$ if we assume the cavity length is $500\ \mu\mathrm{m}$. The intersection of the modal gain and the threshold modal gain defines the threshold injected surface carrier density $N^{\mathrm{th}}_{\mathrm{inj}}$. The threshold lasing condition is reached at a threshold injected surface carrier density $N^{\mathrm{th}}_{\mathrm{inj,s}} = 3.81 \times 10^{12}\mathrm{cm}^{-2}$, corresponding to a volume carrier density of $N^{\mathrm{th}}_{\mathrm{inj,v}} = 5.22 \times 10^{18}\mathrm{cm}^{-3}$. The threshold carrier density is comparable with that of typical III-V MQW lasers. A further increase in the injected surface density above this threshold injected surface density can lead to lasing action.

After the transparency and threshold carrier densities are obtained, it is sufficient to further estimate the threshold current density. The nonradiative rate A_{nr} is set to $10^8\ \mathrm{s}^{-1}$. The Auger coefficient for L-conduction electrons is $C^{\mathrm{L}}_{\mathrm{eeh}} = 3 \times 10^{-32}\ \mathrm{cm}^6\mathrm{s}^{-1}$ [44], while that for holes in the valence band is $C^{\Gamma}_{\mathrm{ehh}} = 7 \times 10^{-32}\ \mathrm{cm}^6\mathrm{s}^{-1}$ [45]. The Auger coefficient for electrons in the Γ-conduction band is still not available in the literature, so we set it identical to that of L-valley electrons. The contribution of the indirection transition to the current density is neglected here since indirect transition rates are usually 4-5 orders smaller than direction transition rates. If the injection quantum efficiency η_i is set to 75%, the transparency current densities for TE and TM polarizations are $1.605\ \mathrm{kA/cm}^2$ and $1.865\ \mathrm{kA/cm}^2$, respectively. Further, the threshold current density of this MQW laser is $1.922\ \mathrm{kA/cm}^2$. The threshold current density is comparable with that of typical III-V MQW lasers (for example, the MQW laser with 5 pairs of InAsP/InGaAsP WAS and 480 nm in length has a threshold current density of $1.4\ \mathrm{kA/cm}^2$ [46]). In addition, the threshold current density of this Ge/SiGeSn MQW laser is much smaller than the predicted threshold current density of $5.8\ \mathrm{kA/cm}^2$ for a bulk Ge on Si laser with 0.25%

tensile-strain at an n-doping concentration of $7.6 \times 10^{19}\ \mathrm{cm}^{-3}$ [14]. It is the quantum-well structure that significantly reduces the required doping concentration and provides high material gain to dramatically reduce the threshold current density. Based on those results, we conclude that lasing action in this n-type doped, tensile-strained Ge/Si$_x$Ge$_y$Sn$_{1-x-y}$ MQW laser is possible.

3.7 Summary

We have developed a theoretical gain model for an n-doped and tensile-strained Ge/Si$_x$Ge$_y$Sn$_{1-x-y}$ multiple-quantum-well laser. The use of tensile strain and n doping in the Ge wells can effectively achieve population inversion for the direct transition and provide significant optical gain. Due to the tensile strain, the highest valance band is LH-like in nature, which leads to a dominant TM-polarized optical gain in this device. Our calculations show that the n-doped, tensile-strained Ge WAS can produce a high material gain to overcome the free-carrier loss and provide a significant net gain. We have also shown our waveguide design and calculated the optical confinement factors of the various regions to estimate the modal gain and predict the threshold carrier density. The threshold current density is estimated to be $1.922\ \mathrm{kA/cm^2}$ with reasonable parameters. Based on our results, we conclude that room-temperature lasing action in this n-doped, tensile-strained Ge/Si$_x$Ge$_y$Sn$_{1-x-y}$ MQW laser is possible.

Bibliography

[1] S. L. Chuang, *Physics of Photonic Devices* (Wiley, New York, 2009), 2nd ed.

[2] O. Boyraz and B. Jalali, "Demonstration of a silicon Raman laser," Opt. Express **12**, 5269–5273 (2004).

[3] L. T. Canham, "Silicon quantum wire array fabrication by electrochemical and chemical dissolution of wafers," Appl. Phys. Lett. **57**, 1046–1048 (1990).

[4] H. Ennen, J. Schneider, G. Pomrenke, and A. Axmann, "1.54-μm luminescence of erbium-implanted III-V semiconductors and silicon," Appl. Phys. Lett. **43**, 943–945 (1983).

[5] G. C. Osbourn, "In$_x$Ga$_{1-x}$As-In$_y$Ga$_{1-y}$As strained-layer superlattices: A proposal for useful, new electronic materials," Phys. Rev. B **27**, 5126–5128 (1983).

[6] A. Adams, "Band-structure engineering for low-threshold high-efficiency semiconductor lasers," Electron. Lett. **22**, 249–250 (1986).

[7] P. Thijs, L. Tiemeijer, P. Kuindersma, J. Binsma, and T. Van Dongen, "High-performance 1.5 μm wavelength InGaAs-InGaAsP strained quantum well lasers and amplifiers," IEEE J. Quantum Electron. **27**, 1426 –1439 (1991).

[8] D. K. Nayak, J. C. S. Woo, J. S. Park, K. L. Wang, and K. P. MacWilliams, "High-mobility p-channel metal-oxide-semiconductor field-effect transistor on strained Si," Appl. Phys. Lett. **62**, 2853–2855 (1993).

[9] K. Rim, J. Hoyt, and J. Gibbons, "Fabrication and analysis of deep submicron strained-Si n-MOSFET's," IEEE Trans. Electron Devices, **47**, 1406 –1415 (2000).

[10] J. Menéndez and J. Kouvetakis, "Type-I Ge/Ge$_{1-x-y}$Si$_x$Sn$_y$ strained-layer heterostructures with a direct Ge bandgap," Appl. Phys. Lett. **85**, 1175–1177 (2004).

[11] S. W. Chang and S. L. Chuang, "Theory of optical gain of Ge-Si$_x$Ge$_y$Sn$_{1-x-y}$ quantum-well lasers," IEEE J. Quantum Electron. **43**, 249–256 (2007).

[12] N. D. Zakharov, V. G. Talalaev, P. Werner, A. A. Tonkikh, and G. E. Cirlin, "Room-temperature light emission from a highly strained Si/Ge superlattice," Appl. Phys. Lett. **83**, 3084–3086 (2003).

[13] V. G. Talalaev, G. E. Cirlin, A. A. Tonkikh, N. D. Zakharov, P. Werner, U. Gösele, J. W. Tomm, and T. Elsaesser, "Miniband-related 1.4-1.8 $\mu\mathrm{m}$ luminescence of Ge/Si quantum dot superlattices," Nanoscale Res. Lett. **1**, 137–153 (2006).

[14] J. Liu, X. Sun, D. Pan, X. Wang, L. C. Kimerling, T. L. Koch, and J. Michel, "Tensile-strained, n-type Ge as a gain medium for monolithic laser integration on Si," Opt. Exp. **15**, 11272–11277 (2007).

[15] J. M. J. Kouvetakis, J. Tolle and V. R. D'Costa, "Advances in Si-Ge-Sn materials science and technology," in *Proceedings of IEEE 4th International Conference on Group IV Photonics*, (Tokyo, Japan, 2007), pp. 1–3.

[16] S. Takeuchi, Y. Shimura, O. Nakatsuka, S. Zaima, M. Ogawa, and A. Sakai, "Growth of highly strain-relaxed $\mathrm{Ge}_{1-x}\mathrm{Sn}_x$/virtual Ge by a Sn precipitation controlled compositionally step-graded method," Appl. Phys. Lett. **92**, 231916 (2008).

[17] O. Madelung, M. Schultz, and H. Weiss, eds., *Physics of Group IV Elements and III-V Compounds*, vol. 17a (Springer-Verlag, New York, 1982), 1st ed.

[18] C. Tserbak, H. M. Polatoglou, and G. Theodorou, "Unified approach to the electronic structure of strained Si/Ge superlattices," Phys. Rev. B **47**, 7104–7124 (1993).

[19] P. Lawaetz, "Valence-band parameters in cubic semiconductors," Phys. Rev. B **4**, 3460–3467 (1971).

[20] M. M. Rieger and P. Vogl, "Electronic-band parameters in strained $\mathrm{Si}_{1-x}\mathrm{Ge}_x$ alloys on $\mathrm{Si}_{1-y}\mathrm{Ge}_y$ substrates," Phys. Rev. B **48**, 14276–14287 (1993).

[21] T. Brudevoll, D. S. Citrin, M. Cardona, and N. E. Christensen, "Electronic structure of α-Sn and its dependence on hydrostatic strain," Phys. Rev. B **48**, 8629–8635 (1993).

[22] Y. H. Li, X. G. Gong, and S. H. Wei, "Ab initio all-electron calculation of absolute volume deformation potentials of IV-IV, III-V, and II-VI semiconductors: The chemical trends," Phys. Rev. B **73**, 245206 (2006).

[23] C. G. V. de Walle, "Band lineups and deformation potentials in the model-solid theory," Phys. Rev. B **39**, 1871–1883 (1989).

[24] M. Willatzen, L. C. L. Y. Voon, P. V. Santos, M. Cardona, D. Munzar, and N. E. Christensen, "Theoretical study of band-edge states in Sn_1Ge_n strained-layer superlattices," Phys. Rev. B **52**, 5070–5081 (1995).

[25] V. R. D'Costa, C. S. Cook, A. G. Birdwell, C. L. Littler, M. Canonico, S. Zollner, J. Kouvetakisand, and J. Menéndez, "Optical critical points of thin-film $Ge_{1-y}Sn_y$ alloys: A comparative $Ge_{1-y}Sn_y$/$Ge_{1-x}Si_x$ study," Phys. Rev. B **73**, 152207 (2006).

[26] V. R. D'Costa, Y.-Y. Fang, J. Tolle, J. Kouvetakis, and J. Menéndez, "Tunable optical gap at a fixed lattice constant in group-IV semiconductor alloys," Phys. Rev. Lett. **102**, 107403 (2009).

[27] V. R. D'Costa, C. S. Cook, J. Menéndez, J. Kouvetakis, and S. Zollner, "Transferability of optical bowing parameters between binary and ternary group-IV alloys," Solid State Commun. **138**, 309–313 (2006).

[28] P. Moontragoon, Z. Ikonić, and P. Harrison, "Band structure calculations of Si-Ge-Sn alloys: achieving direct band gap materials," Semicond. Sci. Technol. **22**, 742–748 (2007).

[29] B. Streetman, *Solid State Electronic Devices* (Prentice-Hall, New Jersey, 1995), 4th ed.

[30] T. Keating, S. H. Park, J. Minch, X. Jin, S. L. Chuang, and T. Tanbun-Ek, "Optical gain measurements based on fundamental properties and comparison with many-body theory," J. Appl. Phys. **86**, 2945–2952 (1999).

[31] J. Minch, S. H. Park, T. Keating, and S. L. Chuang, "Theory and experiment of $In_{1-x}Ga_xAs_yP_{1-y}$ and $In_{1-x-y}Ga_xAl_yAs$ long-wavelength strained quantum-well lasers," IEEE J. Quantum Electron. **35**, 771–782 (1999).

[32] R. Soref and J. Larenzo, "All-silicon active and passive guided-wave components for $\lambda = 1.3$ and 1.6 μm," IEEE J. Quantum Electron. **22**, 873–879 (1986).

[33] C. Hilsum, "Simple empirical relationship between mobility and carrier concentration," Electron. Lett. **10**, 259–260 (1974).

[34] J. I. Pankove, "Optical absorption by degenerate germanium," Phys. Rev. Lett. **4**, 454–455 (1960).

[35] J. I. Pankove, "Properties of heavily doped germanium," in *Prog. Semicond.*, vol. 9 (1965), p. 48.

[36] T. Visser, H. Blok, B. Demeulenaere, and D. Lenstra, “Confinement factors and gain in optical amplifiers,” IEEE J. Quantum Electron. **33**, 1763–1766 (1997).

[37] A. Maslov and C. Ning, “Modal gain in a semiconductor nanowire laser with anisotropic bandstructure,” IEEE J. Quantum Electron. **40**, 1389–1397 (2004).

[38] S.-W. Chang and S. L. Chuang, “Fundamental formulation for plasmonic nanolasers,” IEEE J. Quantum Electron. **45**, 1014–1023 (2009).

[39] S. L. Chuang, “Optical gain of strained wurtzite GaN quantum-well lasers,” IEEE J. Quantum Electron. **32**, 1791 – 1800 (1996).

[40] C. Haas, “Infrared absorption in heavily doped n-type germanium,” Phys. Rev. **125**, 1965–1971 (1962).

[41] R. E. Lindquist and A. W. Ewald, “Optical constants of single-crystal gray tin in the infrared,” Phys. Rev. **135**, A191–A194 (1964).

[42] D. F. Edwards, “Silicon (Si),” in *Handbook of Optical Constants of Solids,* , E. D. Palik, ed. (Academic, Orlando, Florida, 1985), pp. 547–569.

[43] R. F. Potter, “Germanium (Ge),” in *Handbook of Optical Constants of Solids,* , E. D. Palik, ed. (Academic, Orlando, Florida, 1985), pp. 465–478.

[44] S. Marchetti, M. Martinelli, R. Simili, M. Giorgi, and M. Fantoni, “Measurement of Ge electrical parameters by analyzing its optical dynamics,” Phys. Script. **64**, 509-511 (2001).

[45] R. Conradt and J. Aengenheister, “Minority carrier lifetime in highly doped Ge,” Solid State Communications **10**, 321 – 323 (1972).

[46] Z.-B. Hao, Z.-Y. Ren, W. He, and Y. Luo, “1.55 μm InAsP/InGaAsP strained multiple-quantum-well laser diodes grown by solid-source molecular beam epitaxy,” Jpn. J. Appl. Phys. **41**, 754–757 (2002).

Chapter 4

Strain-balanced GeSn/SiGeSn multiple-quantum-well lasers

In this chapter, we propose and analyze a strain-balanced GeSn/SiGeSn multiple-quantum-well (MQW) laser. Since α-Sn has a negative direct-bandgap, alloying Ge with α-Sn can effectively reduce the energy difference between the Γ- and L-conduction band edges to obtain direct-bandgap Gens alloys as a gain medium. In addition, the use of quasi-two-dimensional Ge$_z$Sn$_{1-z}$ QW with a direct bandgap for the gain medium can enable more efficient carriers utilization than that of bulk counterparts because of the improved density of states. To ensure that the Ge$_z$Sn$_{1-z}$ QW is the lowest bandgap semiconductor in the system, the Ge$_z$Sn$_{1-z}$ wells are sandwiched by the Si$_x$Ge$_y$Sn$_{1-x-y}$ barriers to provide an important type-I alignment. We first show our designed structure of a strain-balanced Ge$_z$Sn$_{1-z}$/Si$_x$Ge$_y$Sn$_{1-x-y}$ MQW consisting of tensile-strained Si$_x$Ge$_y$Sn$_{1-x-y}$ barriers and compressive-strained Ge$_z$Sn$_{1-z}$ wells. The thickness and the amount of strain in the wells and barriers are optimized based on the strain-balanced condition that minimizes the total strain energy to reduce the strain-misfit dislocation density in the MQW region. We then calculate the electronic band structure and polarization-dependent optical gain. The compressive strain in the Ge$_z$Sn$_{1-z}$ wells makes the topmost valence

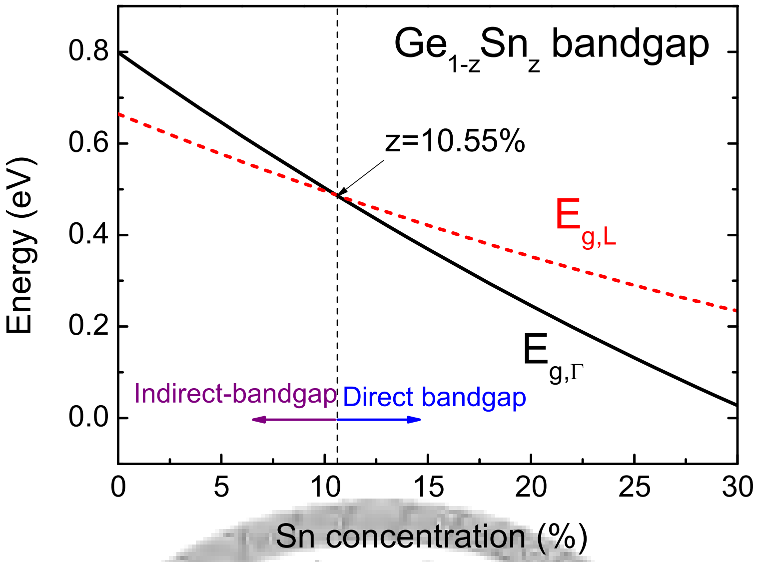

Figure 4.1: Direct and indirect bandgaps of unstrained Ge$_z$Sn$_{1-z}$ alloys as a function of α-Sn concentration. The indirect-to-direct-bandgap transition occurs at $z = 10.55\%$.

band heavy-hole-like (HH-like), resulting in a dominant transverse-electric (TE) gain in this MQW laser. In addition, the inclusion of compressive strain in the Ge$_z$Sn$_{1-z}$ wells can effectively change the valence subband structures to lighten the effective mass of the top HH state so that the threshold carrier density is reduced. We also design a silica index-guiding ridge structure to confine the lasing mode properly and enhance the optical confinement factor in the well region. The modal gain and modal loss are estimated to predict the threshold carrier density and the threshold current density of this MQW laser.

4.1 Direct-bandgap Gens alloys as a gain medium

Among the group-IV semiconductors, Ge holds promises for efficient light-emitters because it is a quasi direct-bandgap semiconductor because its direct conduction band edge lies only 134.5 meV above the bottom of the lowest conduction band. A possible way to reduce this small energy difference is to alloy Ge with α-Sn [1], [2]. One unique property of α-Sn is that the S-like Γ_7^- conduction band edge of α-Sn is situated below the

P-like Γ_8^+ valence band edge, effectively leading to a negative direct bandgap of α-Sn. Figure 4.1 shows the compositional dependence of the direct and indirect bandgaps of unstrained Ge_zSn_{1-z} alloys at 300 K. As the α-Sn composition increases in the Ge_zSn_{1-z} alloys, both the direct and indirect bandgaps decrease, but the direct bandgap decreases more rapidly than the indirect one due to the negative direct-bandgap of α-Sn and the huge bowing parameter of Ge_zSn_{1-z} alloys. The indirect-to-direct-bandgap transition occurs at an α-Sn mole fraction of 10.55$\%$, which agrees well with the experimental observations [2], [3]. Thus, when the mole fraction of α-Sn in Gens alloys is more than 10.55%, direct-bandgap Gens alloys are obtainable for photonic active applications.

4.2 Strain-balanced GeSn/SiGeSn MQW structure

Figure 4.2(a) schematically shows our proposed design of a strain-balanced $Ge_{0.86}Sn_{0.14}$-$Si_{0.09}Ge_{0.8}Sn_{0.11}$ MQW structure, where the crystal growth direction is along the z direction. A fully strain-relaxed $Ge_{0.88}Sn_{0.12}$ buffer layer is grown on a (001)-oriented silicon substrate to act as the virtual substrate for the subsequent growth of quantum wells. Then an *n*-type $Si_{0.08}Ge_{0.78}Sn_{0.14}$ contact layer (lattice-matched to the $Ge_{0.88}Sn_{0.12}$ buffer layer) is grown as the bottom contact. Subsequently, five pairs of $Ge_{0.84}Sn_{0.16}$/$Si_{0.09}Ge_{0.8}Sn_{0.11}$ QWs, that is, five $Ge_{0.84}Sn_{0.16}$ wells and six $Si_{0.09}Ge_{0.8}Sn_{0.11}$ barriers, are then grown on the n-contact. Finally, the whole structure is capped by a *p*-type $Si_{0.08}Ge_{0.78}Sn_{0.14}$ layer as the top contact. Since the $Ge_{0.88}Sn_{0.12}$ buffer layer is fully strain-relaxed, the in-plane lattice constants of the epitaxial layers grown on the $Ge_{0.88}Sn_{0.12}$ buffer layer, such as the $Ge_{0.84}Sn_{0.16}$ wells and the $Si_{0.09}Ge_{0.8}Sn_{0.11}$ barriers, will be compressed or extended to equal that of the $Ge_{0.88}Sn_{0.12}$ buffer layer, as shown in Fig. 4.2(b). The lattice constant of the $Ge_{0.84}Sn_{0.16}$ wells is larger than that of the $Ge_{0.88}Sn_{0.12}$ buffer layer, inducing a 0.57%

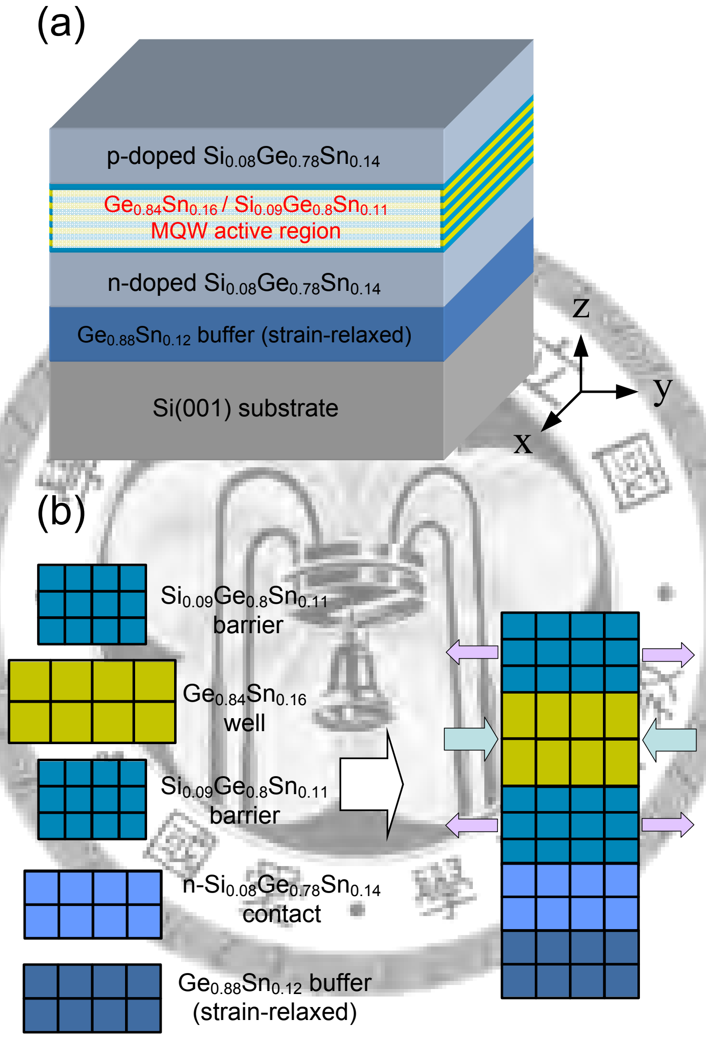

Figure 4.2: (a) Schematics of the strain-compensated $Ge_{0.86}Sn_{0.14}$ quantum-well structure with $Si_{0.09}Ge_{0.8}Sn_{0.11}$ barriers. The MQW structure sandwiched between the n- and p-$Si_{0.09}Ge_{0.8}Sn_{0.11}$ contacts is grown on a silicon substrate via a fully strain-relaxed $Ge_{0.88}Sn_{0.12}$ buffer layer. (b) The strain-compensated MQW consists of compressive-strained $Ge_{0.84}Sn_{0.16}$ wells and tensile-strained $Si_{0.09}Ge_{0.8}Sn_{0.11}$ barriers.

compressive strain in the $\mathrm{Ge_{0.84}Sn_{0.16}}$ wells. On the other hand, the $\mathrm{Si_{0.09}Ge_{0.8}Sn_{0.11}}$ barriers have a smaller lattice constant than that of the $\mathrm{Ge_{0.88}Sn_{0.12}}$ buffer layer, giving rise to a 0.50$\%$ tensile strain for the $\mathrm{Si_{0.09}Ge_{0.8}Sn_{0.11}}$ barriers to compensate for the compressive strain in the $\mathrm{Ge_{0.84}Sn_{0.16}}$ wells. The growth of such highly strained layers with low defect densities have been demonstrated experimentally [4], [5]. The well width is set to 100 Å. The barrier width is determined to be 90 Å by the strain-balanced condition for a cubic-based multilayer system grown along the (001) axis [7], [8]

$$\sum_{i=1}^{n} \frac{A_i L_i \varepsilon^i}{a_i} = 0, \tag{4.1}$$

$$A_i = C_{11}^{(i)} + C_{12}^{(i)} - \frac{2C_{12}^{(i)2}}{C_{11}^{(i)}}, \tag{4.2}$$

where L_i is the thickness of the *i*-th layer. The derivation of the strain-balanced condition is given in Appendix B. The designed alternating growth of the compressive-strained wells and tensile-strained barriers satisfying the strain-balanced condition can minimize the total strain energy and reduce the misfit dislocation density in the MQW region. In this way, the defect-related nonradiative recombination process can be suppressed and the nonradiative recombination current density is reduced.

4.3 Theoretical results and discussions

Figure 4.3 shows the potential profiles of various bands for the $\mathrm{Ge_{0.84}Sn_{0.16}}$ QW with the $\mathrm{Si_{0.09}Ge_{0.8}Sn_{0.11}}$ barriers. The reference energy is set to the top QW HH band edge. The band lineup shows that both the Γ-conduction band minimum and valence band maximum are located in the $\mathrm{Ge_{0.84}Sn_{0.16}}$ well, indicating that this $\mathrm{Ge_{0.84}Sn_{0.16}}$/$\mathrm{Si_{0.09}Ge_{0.8}Sn_{0.11}}$

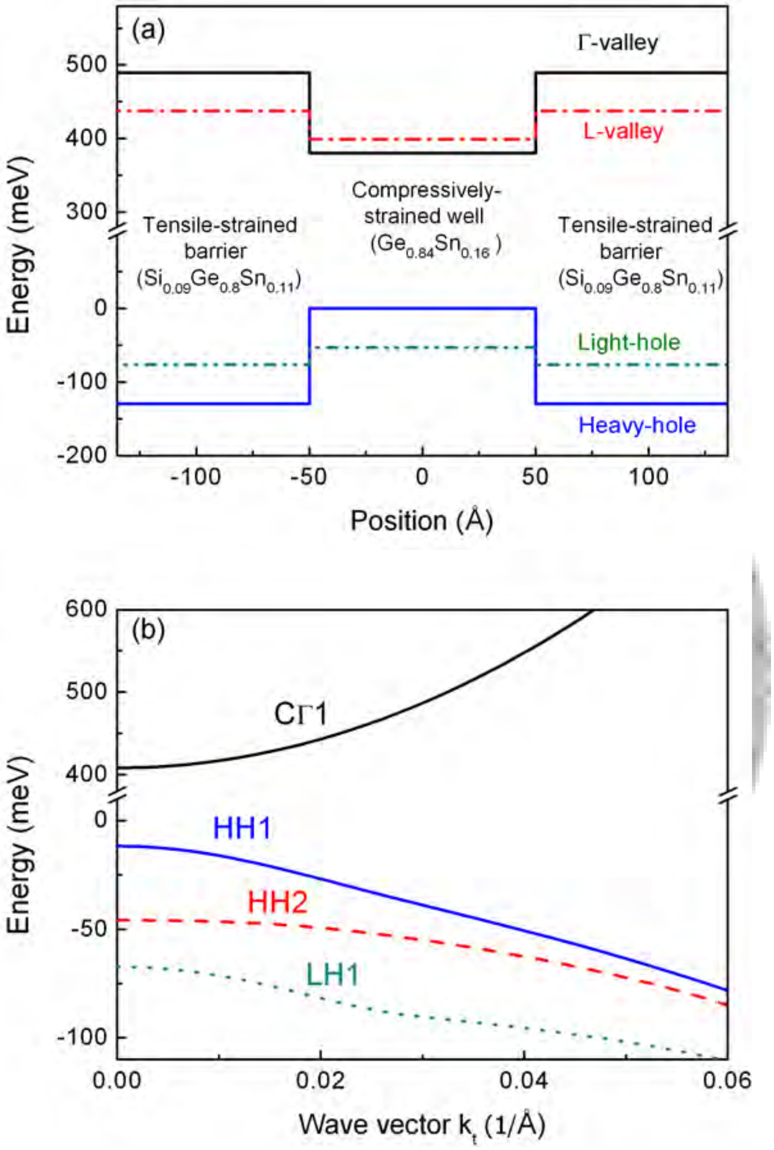

Figure 4.3: (a) Potential profiles of various bands of the $Ge_{0.84}Sn_{0.16}$/$Si_{0.09}Ge_{0.8}Sn_{0.11}$ QW. The band lineup shows an important type-I offset for the spatial confinement of electrons and holes in the well region. (b) In-plane dispersion relations of the Γ-conduction and valence subbands of the $Ge_{0.84}Sn_{0.16}$ well. The compressive strain in the $Ge_{0.84}Sn_{0.16}$ well pushes the HH subbands above the LH subband, so that the highest valence subband is HH-like. While the Γ-conduction subband exhibits a parabolic dispersion relation, the valence-band-mixing effect makes the valence subband dispersion nonparabolic.

QW has a type-I alignment. Thus, electrons and holes can be spatially confined in the $\mathrm{Ge}_{0.84}\mathrm{Sn}_{0.16}$ well, leading to improved electron-hole spatial wavefunction overlaps for the direct transitions occurring in the $\mathrm{Ge}_{0.84}\mathrm{Sn}_{0.16}$ well. In the $\mathrm{Ge}_{0.84}\mathrm{Sn}_{0.16}$ well region, although the compressive strain in the well lifts both the Γ- and L-conduction band edges, the Γ-conduction band edge is $19\ \mathrm{meV}$ lower than the L-conduction one, and the lowest Γ-conduction subband is $3\ \mathrm{meV}$ lower than the lowest L-conduction subband. Despite the lowest Γ- and L-conduction subbands are almost at the same level, population inversion in the Γ-conduction band is achievable to provide significant optical gain through the direct transitions. In the valence band, the compressive strain pushes the HH band edge above the LH band edge, so that the topmost valence band is HH-like. Correspondingly, Fig. 4.3(b) shows the dispersion relations of both the Γ-conduction and valence subbands for the $\mathrm{Ge}_{0.84}\mathrm{Sn}_{0.16}$ well under the axial approximation [1]. Owing to the compressive strain in the $\mathrm{Ge}_{0.84}\mathrm{Sn}_{0.16}$ well, the HH1 state is at least $34\ \mathrm{meV}$ higher than the other valence subbands near the zone center. While the Γ-conduction subband exhibits a parabolic dispersion relation, the valence subbands are nonparabolic due to the valence-band-mixing effect. In addition, the valence-band-mixing effect steepens the HH1 dispersion relation, leading to a lighter effective mass and reduced density of states of the HH1 state. With the large energy separation between the HH1 subband and the other valence subbands near the zone center, the lighter HH1 in-plane effective mass leads to a rapid accumulation of the injected holes in the HH1 subband under current injection. As a result, the hole quasi-Fermi level will lower into the valence subbands more rapidly under increasing carrier injection and reach the population inversion condition at a lower carrier density. In addition, the valence-band-mixing effect also affects the optical transitions. The selection rules only allow for the interband transitions from the first Γ-conduction

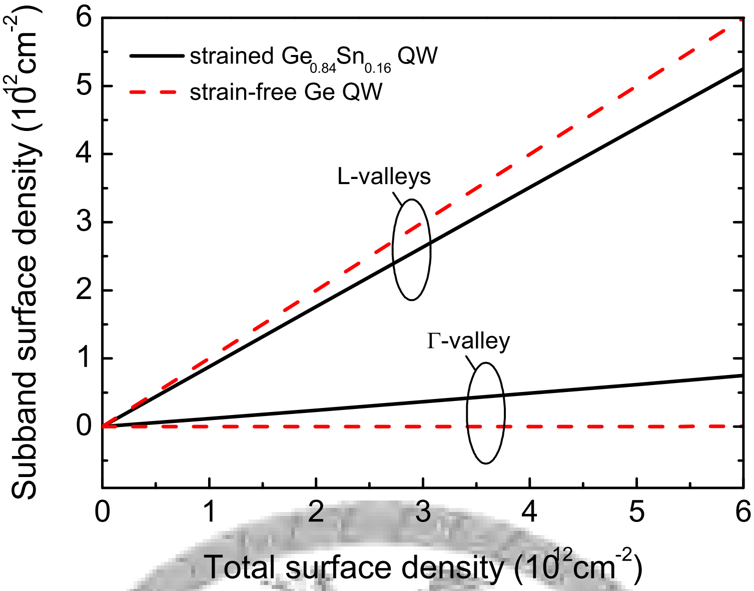

Figure 4.4: Comparison of the surface carrier densities of the Γ- and L-conduction subbands as a function of the total injected surface carrier density between the strained $Ge_{0.84}Sn_{0.16}/Si_{0.09}Ge_{0.8}Sn_{0.11}$ QW and a strain-free $Ge/Si_{0.15}Ge_{0.81}Sn_{0.04}$ QW with identical barrier and well widths. A significant improvement of injected carriers into the Γ-conduction subband for population inversion is present.

subband to the first HH subband ($C\Gamma1$-HH1) and to the first LH subband ($C\Gamma1$-LH1) at the Brillouin zone center. However, the valence-band-mixing effect at the finite transverse wave vector enables the originally forbidden transition between the first Γ-conduction and the second HH subbands ($C\Gamma1$-HH2) at the zone center, and makes $C\Gamma1$-HH2 also contribute to the optical gain.

Figure 4.4 shows the surface carrier densities of the Γ- and L-conduction subbands as a function of the total surface carrier density for the strained $Ge_{0.84}Sn_{0.16}$ QW with $Si_{0.09}Ge_{0.8}Sn_{0.11}$ barriers, compared with those of a strain-free $Ge/Si_{0.15}Ge_{0.81}Sn_{0.04}$ QW with a well width of 100 Å and a barrier width of 90 Å. The injected surface carrier density is limited to $6 \times 10^{12}\ \mathrm{cm}^{-2}$ because further increase of injected carrier density will raise the electron quasi-Fermi level over the barrier potential of the L-conduction valleys. For the strain-free Ge QW, the Γ-conduction band edge is 134.5 meV higher than the L-conduction one at room temperature. As a result, only fewer than 0.05%

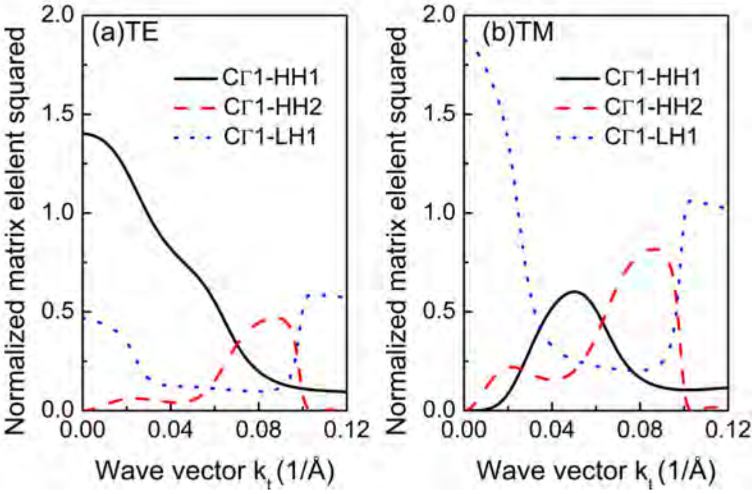

Figure 4.5: (a) TE and (b) TM normalized squared momentum matrix elements for the possible interband transitions. Near the zone center, the CΓ1-HH1 transition has a larger TE component while the CΓ1-LH1 transition has a dominant TM component, indicating that the CΓ1-HH1 and CΓ1-LH1 transitions are dominant for TE and TM optical gains, respectively.

injected carriers can populate the direct conduction subbands, and the rest of carriers leaks into the L-conduction subbands. Since those electrons in the L-conduction subbands cannot radiatively recombine with holes through the direct transitions, the light-emitting efficiency of the strain-free Ge well is low. On the other hand, for the strained $Ge_{0.84}Sn_{0.16}$ QW, despite the lowest Γ- and L-conduction subbands are almost at the same level, about 12.5% injected carriers can populate the direct conduction subband to achieve population inversion. The significant improvement of the injected carriers into the direct conduction band leads to a considerable optical gain via the direct transitions. Another advantage of using Gens QWs as the gain medium over Ge QWs is that the electron effective mass of the Γ-conduction band for α-Sn is 52% larger than that of Ge. Therefore, alloying Ge with α-Sn can enhance the density of states of the Γ-conduction subband. As a result, more carriers to populate the Γ-conduction subband under carrier injection and provide more optical gain through the direct transitions.

Figure 4.5 shows the transverse-electric (TE) and transverse-magnetic (TM) normalized squared momentum matrix elements $M_{nm}^{\sigma,\mathrm{TE}}/M_{\mathrm{b}}^2$ and $M_{nm}^{\sigma,\mathrm{TM}}/M_{\mathrm{b}}^2$ as a function of the magnitude of the transverse wavevector k_{t} for all possible interband transitions, where n and m are the subband indices of the Γ-conduction and valence subbands, respectively; and M_{b} is the bulk momentum matrix element of $\mathrm{Ge}_{0.84}\mathrm{Sn}_{0.16}$. Near the zone center, the CΓ1-HH1 transition has a dominant magnitude for the TE momentum matrix element, while the CΓ1-LH1 transition has a stronger TM component than the other transitions. Thus, the CΓ1-HH1 transition is dominant for the TE gain while the CΓ1-LH1 transition dominates the TM gain. As the wavevector k_{t} increases, the valence-band-mixing effect increases the TE momentum matrix element for the CΓ1-HH2 transition, and the TM momentum matrix elements for the CΓ1-HH1 and CΓ1-HH2 transitions. However, since the HH1 subband is the topmost valence subband with a large energy separation from the other valence subbands, the injected holes will populate mostly the HH1 subband. This means CΓ1-HH1 transition is expected to be dominant in the $\mathrm{Ge}_{0.84}\mathrm{Sn}_{0.16}$ well and contributes mostly to the TE gain.

Figure 4.6 shows the TE and TM material gain spectra at different total injected surface carrier densities. The carrier leakage into the L-conduction valleys, which does not contribute to the material gain here, has been included. The full-width-at-half-maximum (FWHM) linewidth is set to 20 meV. Since the CΓ1-HH1 transition has a dominant TE momentum matrix element, the TE material gain is substantially larger than the TM gain in this MQW laser. In addition, the fast-increasing TE gain due to the lighter HH1 effective mass helps reach the threshold lasing condition at a lower carrier density. The TE gain is peaked around 430 meV, corresponding to an emission wavelength of $2.883\ \mu\mathrm{m}$, which is in the mid-infrared spectral range. When the number of surface carriers increases further, the probability for injected holes to occupy the LH1 subband increases. In this way,

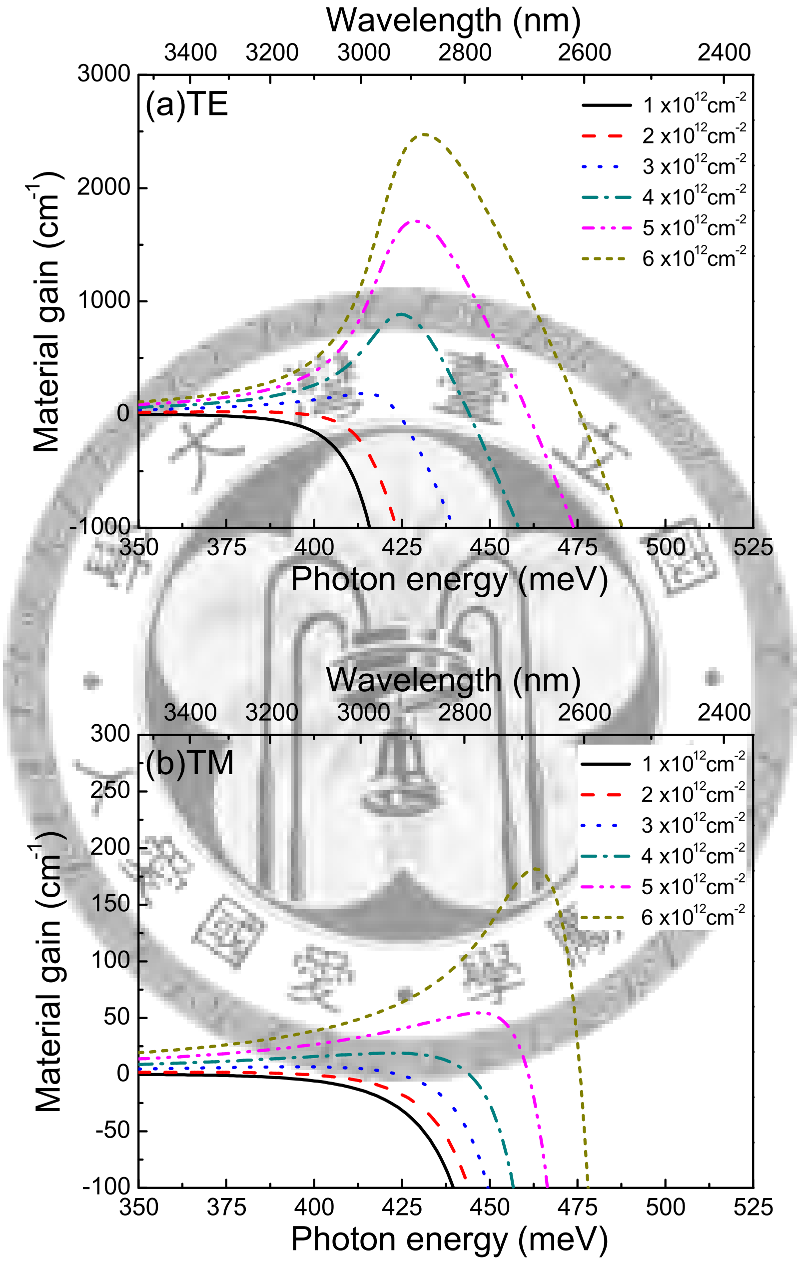

Figure 4.6: (a) TE and (b) TM material gain spectra at different total injected surface carrier densities. Because the top valence subband is HH-like, the dominant CΓ1-HH1 transition contributes mostly the TE gain, while the C1-LH1 transition contributes to a relatively weaker TM gain due to the less hole occupation in the LH subband.

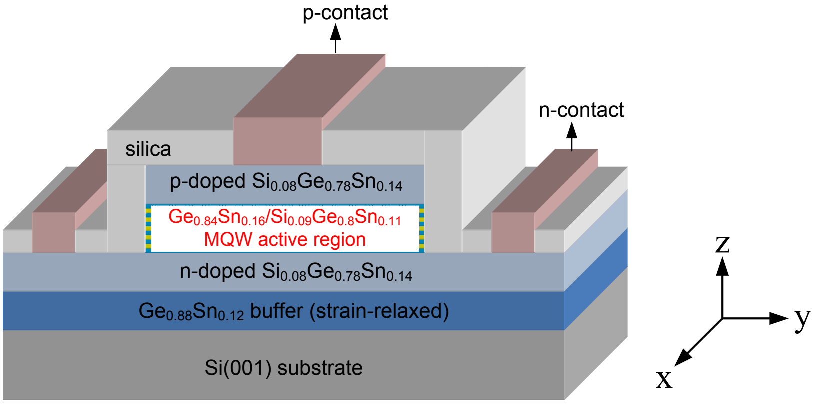

Figure 4.7: The designed silica ridge waveguide for index guiding. The silica ridge structure has a smaller refractive index than those of the semiconductors, and it can provide better optical confinements for the active region.

the $C\Gamma1$-LH1 transition will bring about mostly the TM gain peaked around 475 meV, as shown in Fig. 4.6(b).

For SiGeSn material system, another important issue is the high refractive index of α-Sn. At a such long wavelength $\lambda = 2.883\ \mu\text{m}$, α-Sn has a larger refractive index ($n_{\text{Sn}} = 5.791$ [9]) than those of Si ($n_{\text{Si}} = 3.434$ [10]) and Ge ($n_{\text{Ge}} = 4.051$ [11]), indicating that the ternary SiGeSn compounds with a high α-Sn composition have a high refractive index. As a result, the n- and p-contacts with refractive indices slightly smaller than that of the MQW active region may not provide the necessary optical confinement for the active region. To confine lasing modes better, we employ silica, which has a smaller refractive index ($n_{\text{SiO}_2} = 1.4198$ [12]) than those of Si, Ge, and α-Sn, as the ridge waveguide structure for index guiding, as shown in Fig. 4.7 The high contrast in the refractive indices between the silica ridge structure and the active region can provide a better optical confinement for the active region. Thus, the enhanced optical confinement factor of the wells can further reduce the threshold carrier density for this MQW laser. We use the finite element method to calculate the field distributions of the guided modes in this waveguide. Since the TE material gain is dominant, this MQW laser is likely to

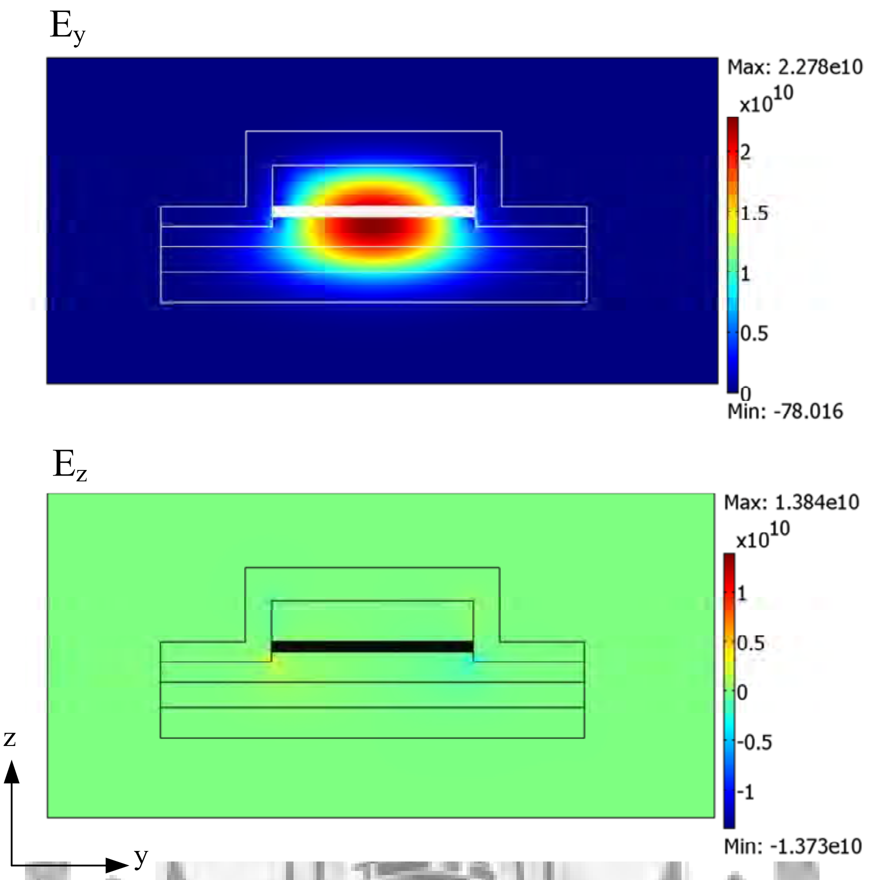

Figure 4.8: Transverse electric field distributions for the quasi-TE fundamental mode at $\lambda = 2.883\ \mu\text{m}$, showing that E_y is the dominant component. The silica ridge waveguide structure provides the upper cladding while the silicon substrate acts as the lower cladding for the active region. The peak of the transverse electrical field is located near the active region, providing a reasonable QW optical confinement factor of 6.98%.

lase with the quasi-TE modes at $\lambda = 2.883\ \mu\text{m}$. Meanwhile, we neglect the contribution from the TM material gain for the modal gain, since the TM material gain has a negligible magnitude at $\lambda = 2.883\ \mu\text{m}$ in contrast to that of TE material gain.

Correspondingly, Fig. 4.8 shows the transverse electric field distributions for the quasi-TE fundamental mode at $\lambda = 2.883\ \mu\text{m}$. The width of the ridge structure is 2 μm and the thickness of the p-contact is optimized to be 500 nm for maximizing the optical confinement factor of the wells. First, the dominant transverse electric field for the quasi-TE fundamental mode is E_y. From the field distribution, the silica ridge structure acts as the upper cladding while the silicon substrate plays the role of the lower cladding. The

Table 4.1: Doping concentrations, absorption losses, optical confinement factors, and modal losses in various regions

	wells	n-contact	p-contact
Doping concentration (cm^{-3})	N/A	5×10^{18}	1×10^{19}
Absorption loss (cm^{-1})	N/A	32.89	185.75
Optical confinement factor $(\%)$	6.98	42.75	25.91
Modal loss (cm^{-1})	0	14.06	48.12

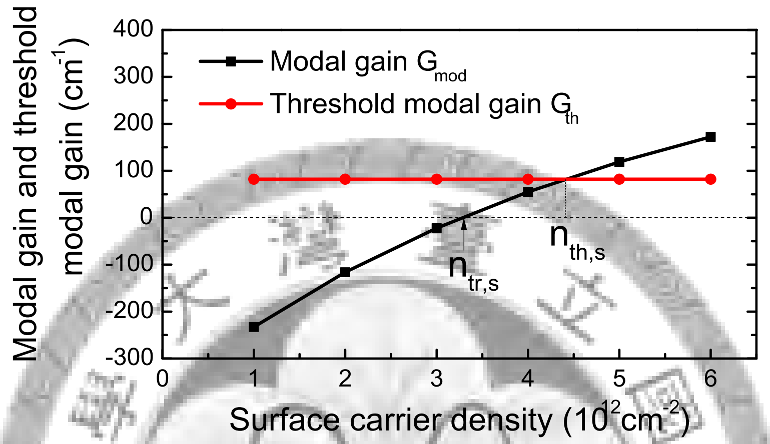

Figure 4.9: Modal gain and threshold modal gain as a function of the total injected surface density for the quasi-TE fundamental mode at $\lambda = 2.883\ \mu\mathrm{m}$. The intersection of the modal gain and the threshold modal gain gives the threshold surface carrier density of this MQW laser $n_{\mathrm{th,s}} = 4.364 \times 10^{12}\ \mathrm{cm}^{-2}$.

peak transverse electric field is located near the active region, providing a reasonable QW optical confinement factor of 6.98%. Table 4.1 tabulates the doping concentrations, the TE optical confinement factors for the quasi-TE fundamental mode, the absorption losses due to free-carrier absorption, and the modal losses in various regions. The TE optical confinement factors in the n- and p-contacts are much larger than that in the wells due to their relatively large thicknesses. Because of the high electron mobility of Ge, the absorption loss in the n-contact is insignificant. However, the small hole mobility and the high doping concentration in the p-contact leads to a significant absorption loss and contributes to the major modal loss in the waveguide.

To predict the threshold surface carrier density of this MQW laser, Fig. 4.9 shows the modal gain and the threshold modal gain as a function of the total injected surface density for the quasi-TE fundamental mode at $\lambda = 2.883\ \mu\mathrm{m}$, where the cavity length is set to $500\ \mu\mathrm{m}$. The reflectivities at the two facets are estimated to be $R_1 = R_2 = 0.357$ by the simple estimation from the effective index of the quasi-TE fundamental mode. The corresponding mirror loss is $19.98\ \mathrm{cm}^{-1}$. The modal gain increases with the injected surface carrier density, and reaches the transparency condition at a surface carrier density of $n_{\mathrm{tr,s}} = 3.304 \times 10^{12}\ \mathrm{cm}^{-2}$, corresponding to a volume carrier density of $n_{\mathrm{tr,v}} = 3.304 \times 10^{18}\ \mathrm{cm}^{-3}$. Above this transparency carrier density, net optical gain form the QW is obtainable. For a working laser device, the modal gain has to reach the threshold modal gain, which is the sum of the modal loss and radiation loss, so that the stimulated emission can take over the spontaneous emission to dominate the light output. The intersection of the modal gain and the threshold modal gain defines the threshold surface carrier density for the quasi-TE fundamental mode $n_{\mathrm{th,s}} = 4.364 \times 10^{12}\ \mathrm{cm}^{-2}$, corresponding to a volume threshold carrier density of $n_{\mathrm{th,v}} = 4.364 \times 10^{18}\ \mathrm{cm}^{-3}$. This threshold carrier density is still in a reasonable and achievable range compared to those of typical III-V MQW lasers. Around this threshold carrier density, the stimulated emission will take place and lead to lasing action. Based on the transparency carrier density and the threshold carrier density, it is possible to further estimate the transparency current density J_{tr} and the threshold current density J_{th}. Here the contribution of the indirect transitions to the current density is neglected because indirect transition rate is usually 4-5 orders smaller than direct transition rate. The nonradiative rate is set to $10^8\ \mathrm{s}^{-1}$. Since the Auger recombination coefficients for the Sn-based alloys are still unavailable yet, we set the Auger recombination coefficients $C^{\mathrm{L}}_{\mathrm{eeh}} = C^{\Gamma}_{\mathrm{eeh}} = C^{\Gamma}_{\mathrm{ehh}}$ to $1 \times 10^{-28}\ \mathrm{cm}^6\mathrm{s}^{-1}$ according to those of the GaInAsSb QW at similar emission wavelengths [13]. If the injection quantum efficiency is set to 75%, we obtain the transparency current density $J_{\mathrm{tr}} = 4.46\ \mathrm{kA/cm}^2$

and the threshold current density $J_{\mathrm{th}} = 9.78\ \mathrm{kA/cm^2}$. As expected, the Auger nonradiative recombination is the major limiting factor to the transparency and threshold current densities in this MQW laser. The threshold current density of this MQW laser is comparable with those of typical mid-infrared MQW lasers (for example, $7\ \mathrm{kA/cm^2}$ for a GaSb MQW laser at $3.26\ \mu\mathrm{m}$ [14], and $10\ \mathrm{kA/cm^2}$ for a AlGaAsSb/InGaAsSb MQW laser at $2.78\ \mu\mathrm{m}$ [15]). Above this threshold current density, the stimulated emission takes place and enables the lasing action for important mid-infrared applications, such as gas sensing, molecular spectroscopy, and chemical process monitoring.

4.4 Summary

We have theoretically analyzed a strain-balanced $\mathrm{Ge_{84}Sn_{16}/Si_{0.09}Ge_{0.8}Sn_{0.11}}$ MQW laser. The incorporation of α-Sn into Ge layers can effectively reduce the energy difference between the direct- and indirect-conduction band edges and provide a direct-bandgap Gens alloy to achieve population inversion. The compressive strain in the $\mathrm{Ge_{84}Sn_{0.16}}$ well makes the top-most valence subband HH-like and the TE-polarized gain dominant. The lighter HH1 effective mass due to the compressive strain also reduces the threshold carrier density. The designed silica ridge structure for index guiding shows good optical confinement for the lasing mode. We estimate the threshold volume carrier density as $n_{\mathrm{th,v}} = 4.364 \times 10^{18}\ \mathrm{cm^{-3}}$ and the threshold current density of this MQW laser as $J_{\mathrm{th}} = 9.78\ \mathrm{kA/cm^2}$ for a cavity length of $500\ \mu\mathrm{m}$ with reasonable parameters. Our calculations indicate that the lasing action in this strain-balanced $\mathrm{Ge_{84}Sn_{16}/Si_{0.09}Ge_{0.8}Sn_{0.11}}$ MQW laser is possible.

Bibliography

[1] R. A. Soref and C. H. Perry, “Predicted band gap of the new semiconductor SiGeSn,” J. Appl. Phys. **69**, 539–541 (1991).

[2] G. He and H. A. Atwater, “Interband transitions in $\mathrm{Sn}_x\mathrm{Ge}_{1-x}$ alloys,” Phys. Rev. Lett. **79**, 1937–1940 (1997).

[3] H. P. L. de Guevara, A. G. Rodríguez, H. Navarro-Contreras, and M. A. Vidal, “Determination of the optical energy gap of $\mathrm{Ge}_{1-x}\mathrm{Sn}_x$ alloys with $0 < x < 0.14$,” Appl. Phys. Lett. **84**, 4532–4534 (2004).

[4] O. Gurdal, P. Desjardins, J. R. A. Carlsson, N. Taylor, H. H. Radamson, J.-E. Sundgren, and J. E. Greene, “Low-temperature growth and critical epitaxial thicknesses of fully strained metastable $\mathrm{Ge}_{1-x}\mathrm{Sn}_x$ (x $\leq$ 0.26) alloys on Ge(001)2 $\times$ 1,” J. Appl. Phys. **83**, 162–170 (1998).

[5] J. Tolle, R. Roucka, A. V. G. Chizmeshya, J. Kouvetakis, V. R. D’Costa, and J. Menéndez, “Compliant tin-based buffers for the growth of defect-free strained heterostructures on silicon,” Appl. Phys. Lett. **88**, 252112 (2006).

[6] V. D. Jovanović, Z. Ikonić, D. Indjin, P. Harrison, V. Milanović, and R. A. Soref, “Designing strain-balanced GaN/AlGaN quantum well structures: Application to intersubband devices at 1.3 and 1.55 $\mu\mathrm{m}$ wavelengths,” J. Appl. Phys. **93**, 3194–3197 (2003).

[7] N. J. Ekins-Daukes, K. Kawaguchi, and J. Zhang, “Strain-balanced criteria for multiple quantum well structures and its signature in X-ray rocking curves,” Cryst. Growth Design **2**, 287–292 (2002).

[8] S. L. Chuang, *Physics of Photonic Devices* (Wiley, New York, 2009), 2nd ed.

[9] V. R. D’Costa, Y. Y. Fang, J. Mathews, R. Roucka, J. Tolle, J. Menéndez, and J. Kouvetakis, “Sn-alloying as a means of increasing the optical absorption of Ge at the C- and L-telecommunication bands,” Semicond. Sci. Technol. **24**, 1–8 (2009).

[10] D. F. Edwards, "Silicon (Si)," in *Handbook of Optical Constants of Solids,* , E. D. Palik, ed. (Academic, Orlando, Florida, 1985), pp. 547–569.

[11] R. F. Potter, "Germanium (Ge)," in *Handbook of Optical Constants of Solids,* , E. D. Palik, ed. (Academic, Orlando, Florida, 1985), pp. 465–478.

[12] H. R. Philipp, "Silicon dioxide (SiO_2) (glass)," in *Handbook of Optical Constants of Solids,* , E. D. Palik, ed. (Academic, Orlando, Florida, 1985), pp. 749–763.

[13] A. Joullié, P. Christol, A. N. Baranov, and A. Vicet, "Mid-infrared 2-5 μm heterojunction laser diodes," in *Solid-state mid-infrared laser sources,* , I. T. Sorokina and K. L. Vodopyanov, eds. (Springer, Berlin, Germany, 2003), pp. 1–61.

[14] M. Grau, C. Lin, O. Dier, C. Lauer, and M.-C. Amann, "Room-temperature operation of 3.26 μm GaSb-based type-I lasers with quinternary AlGaInAsSb barriers," Appl. Phys. Lett. **87**, 241104 (2005).

[15] H. Lee, P. K. York, R. J. Menna, R. U. Martinelli, D. Z. Garbuzov, S. Y. Narayan, and J. C. Connolly, "Room-temperature 2.78 μm AlGaAsSb/InGaAsSb quantum-well lasers," Appl. Phys. Lett. **66**, 1942–1944 (1995).

Chapter 5

Polarization-insensitive electroabsorption waveguide modulators using tensile-strained Ge/SiGeSn quantum wells at 1550 nm wavelength

In this chapter, we propose and analyze a polarization-insensitive electroabsorption modulator employing tensile-strained Ge/Si$_x$Ge$_y$Sn$_{1-x-y}$ quantum wells (QWs) operating at 1550 nm wavelength. First, we will briefly introduce the background and physics of electroabsorption effects in semiconductors, including the Franz-Keldysh (FK) effect in bulk semiconductors and the quantum-confined Stark effect (QCSE) in low dimensional semiconductor structures, such as quantum-well, quantum-wire, and quantum-dot structures. Then the first observation of strong QCSE in Ge/SiGe QWs will be introduced. We then develop a theoretical model for a QT electroabsorption modulator, including the electronic band structure, excitonic absorption, variation method for calculating exciton binding energies and oscillation strengths, and polarization-dependent optical confinement factor. Our theoretical results for QCSE in Ge/SiGe QWs will be compared with the experimental data.

In the second part, we propose and analyze a polarization-insensitive electroabsorption waveguide modulator using tensile-strained Ge/Si$_x$Ge$_y$Sn$_{1-x-y}$ quantum wells based on the quantum-confined Stark effect for 1550 nm operation. The use of tensile strain can effectively reduce the direct bandgap of the Ge wells to realize optimal modulation near 1550 nm wavelength, and achieve near degeneracy between the first heavy-hole and light-hole subbands for polarization-insensitive operation. We calculate the electronic band structure, polarization-dependent excitonic absorption coefficients, and polarization-dependent optical confinement factors. We also present our waveguide design for index guidance and calculate the optical confinement factors of various regions to determine the extinction ratio and insertion loss. With optimal designs of the MQW material and waveguide geometry, it is possible to achieve polarization-insensitive operation at 1550 nm wavelength in this electroabsorption waveguide modulator using tensile-strained Ge/Si$_x$Ge$_y$Sn$_{1-x-y}$ QWs.

5.1 Electroabsorption effects in semiconductors

Electroabsorption effects near semiconductor band edges have been intensively investigated for many years, including the Franz-Keldysh effect in bulk materials and the quantum-confined Stark effect in low-dimensional quantum structures. When a photon passes through a semiconductor with its energy larger than the bandgap of a semiconductor, it excites an electron in the valence band to the conduction band. This process is called interband transition which can happen in direct and indirect bandgap semiconductors and follows the Fermi's golden rule, that is, the energy and momentum conservation rules have to be satisfied. Meanwhile, the below-bandgap transitions are prohibited because there is

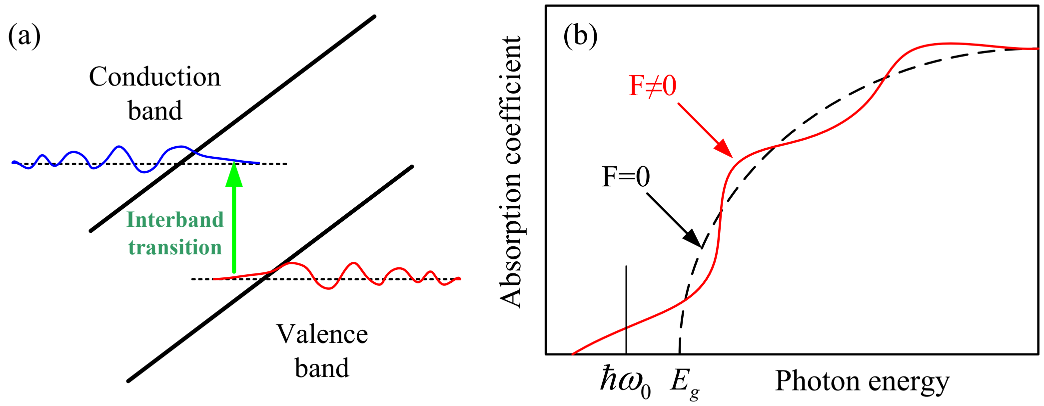

Figure 5.1: (a) Franz-Keldysh effects in bulk semiconductors with and without an electric field. (b) Absorption spectra in a bulk semiconductor with and without an electric field, showing that below-bandgap transitions become possible in the presence of an electric field.

no allowed state for such interband transitions. When an electric field is applied on a semiconductor, the tilted energy profiles of the semiconductor due to the electric field enable the originally forbidden below-bandgap transitions. In this way, the absorption spectrum significantly red shifts and the external electric field can control the near-gap absorption coefficients in semiconductors to achieve modulation in the semiconductors. Compared with other modulation mechanisms, such as electrooptic effects, acousticoptic effects, and free carrier plasma dispersion effects, electroabsorption effects are a very fast mechanism. Thus, modulators based on electroabsorption effects can achieve a very high-speed modulation of 40 GHz or higher. In addition, optical modulators based on electroabsorption effects are attractive for their small size and low-energy consummation, which are very important for electronic-photonic integrated circuits. Those advantages make electroabsorption modulators attractive for high density electronic-photonic integrated circuits.

5.1.1 Franz-Keldysh effect

The Franz-Keldysh effect describes the changes in absorption wavelength and strength in bulk semiconductors due to near bandgap transitions caused by an electric field. When an electric field is applied, the band structure of bulk semiconductors is tilted, as shown in Fig. 5.1(a). As a result, the electron wavefunction in the direct conduction band and hole wavefunction in the valence band tail into the bandgap, giving rise to probability of tunneling. Thus, the originally forbidden below-bandgap transitions become possible in the presence of an electric field, significantly increasing the below-bandgap absorption coefficients, as shown in Fig. 5.1(b). In this way, changing the strength of the electric field can manipulate the below-gap absorption coefficients to achieve modulation of light. However, a large electric field is usually required to have a sufficient change in absorption coefficient in bulk semiconductors due to the large thickness. As a result, the driving voltage in electroabsorption modulators employing bulk semiconductors based on the Franz-Keldysh effect is usually larger than 5 V.

5.1.2 Quantum-confined Stark effect

The quantum-confined Stark effect (QCSE) is another electroabsorption effect that describes a strong electric-field-dependent change in optical absorption spectra in low dimensional structures, such as quantum-well, quantum-wire, and quantum-dot systems. Figure 5.2 shows the scheme of QCSE in a type-I quantum well structure. In the absence of an electric field, there are quantized electron and hole states in the QT, as shown in Fig 5.2(a). Usually, the wavefunction overlap between the ground electron and hole states can approach to almost unity if the band offsets are large enough. When an electric field is applied across the QT, the energy potential profiles of the conduction and valence bands are tilted by the electric field. As a result, the electron and hole wavefunctions move in opposite directions, leading to a reduced transition energy and wavefunction overlap, as shown in Fig. 5.2(b). Since the oscillation strength is proportional to the

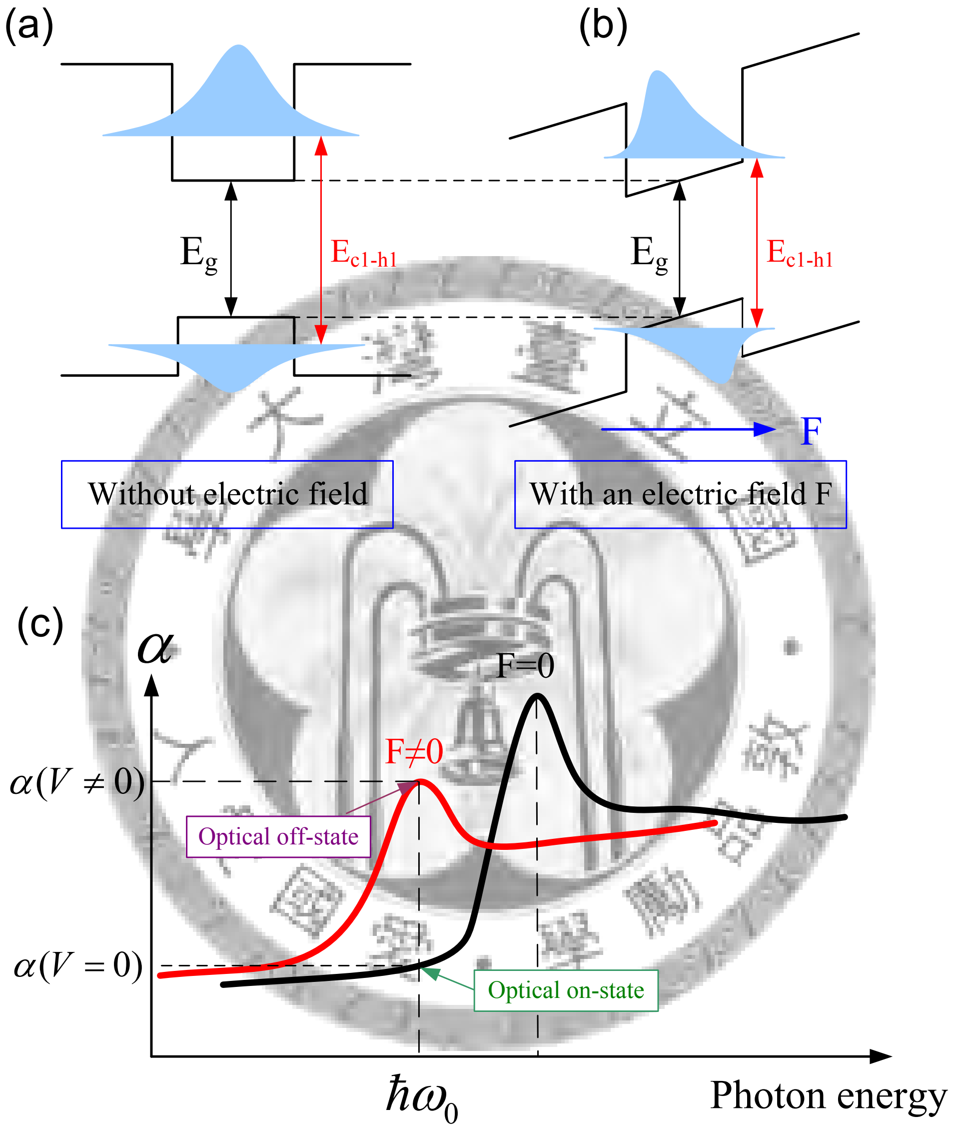

Figure 5.2: Electronic band structure and subband wavefunctions in a type-I quantum-well (a) with and (b) without an electric field. The electric field tilts the band profiles and pushes the electron and hole wavefunctions apart, reducing the electron-hole wavefunction overlap and transition energy. (c) Comparison of absorption spectra in a QT with and without an electric field, showing controllable near-gap absorption coefficients by an electric field.

squared wavefunction overlap between the electron and hole states, the whole absorption spectrum significantly red shifts with a reducing strength due to the tilted band profiles, as shown in Fig. 5.2(c). As a result, at zero bias, the semiconductor is transparency at the photon energy of $\hbar\omega_0$, while the semiconductor can become very absorptive under an electric field at the same photon energy. In this way, the near-gap absorption coefficients are controllable by the strength of the electric field to achieve modulation of light. In an infinite-barrier-high quantum well, the energy reduction of the ground transition due to an electric field F based on the perturbation theory can be expressed as [1]

$$\Delta E = \frac{\pi^2 - 15}{24\pi^2} \times \frac{(m_\mathrm{e} + m_\mathrm{h}) e^2 F^2 L^4}{\hbar^2}, \tag{5.1}$$

where m_e and m_h are electron and hole effective masses along the QT growth direction, respectively, and L is the well width. This simple formula points out that the Stark shift depends on the carrier effective mass, well width, and strength of electric field. The main difference between the Franz-Keldysh effect and the quantum-confined Stark effect is that the excitonic effect in quantum structures is significant compared to that in bulk materials, even at room temperature. The excitonic enhancement on the absorption coefficient is very strong and can lead to a significant change in absorption coefficient with QCSE. Thus, the quantum-confined Stark effect is considered the strongest electroabsorption effect. In addition, semiconductor quantum structures are much thinner in thickness than the bulk counterparts, so the electroabsorption modulators based on QCSE can have a driving voltage less than 2 V, much smaller than those based on the Franz-Keldysh effect. Thus, electroabsorption modulators based on QCSE are preferred for electronic-photonic integrated circuits.

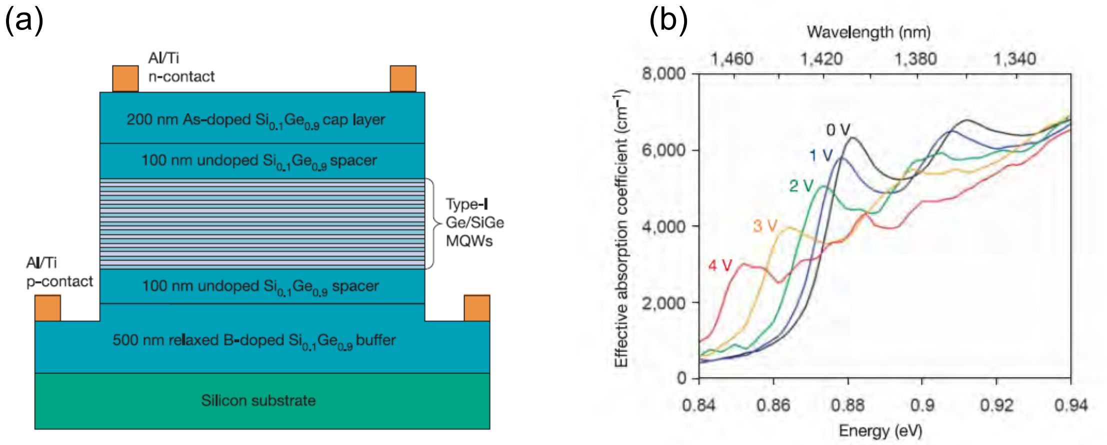

Figure 5.3: (a) Schematic structure of a type-I Ge/SiGe MQW system on a silicon substrate via a SiGe buffer layer. (b) Bias-dependent absorption spectra of the Ge/SiGe QWs [1].

5.1.3 Strong quantum-confined Stark effects in type-I Ge/SiGe quantum wells

Usually, the quantum-confined Stark effect is observed in direct-bandgap semiconductors. For indirect bandgap semiconductors, such as Si and Ge, they are indirect bandgap semiconductors and usually considered to have weak electroabsorption effects. Although some interest attempts have been made, SiGe/Si quantum well does not exhibit efficient QCSE due to the small conduction band offsets in type-I structures or small wavefunction overlaps in type-II structures [3, 4, 5, 6]. Until recently, a strong quantum-confined Stark effect was observed in type-I Ge/SiGe QWs [1]. The Ge/SiGe QWs consist of compressive-strained Ge wells and tensile-strained SiGe barriers grown on a silicon substrate via a strain-relaxed SiGe buffer layer, as shown in Fig. 5.3(a). Besides, this Ge/SiGe QWs have a type-I alignment with sufficiently high conduction and valence band offsets. Although the Ge QWs are an indirect bandgap material, they exhibit strong bias-dependent changes in absorption coefficient and wavelength, that is, quantum-confined Stark effect, as shown in Fig 5.3(b). The observed strength of the QCSE in the Ge/SiGe

QWs is comparable with that in typical III-V direct-bandgap materials. This important observation of robust QCSE in Ge/SiGe QWs has opened up new possibilities for high-speed Si-based modulators, and electroabsorption modulators employing Ge/SiGe QWs have been demonstrated [7].

5.2 Theory of excitonic absorption in a quantum well based on the quantum-confined Stark effect

In this section, we develop a theoretical model for a QT electroabsorption modulator based on the quantum-confined Stark effect, including the electronic band structure, excitonic absorption coefficient, variational method for calculating the exciton binding energies and oscillation strengths, polarization-independent optical confinement factor, extinction ratio, and insertion loss.

5.2.1 Electronic band structure

If a quantum well is grown along the z direction, the Γ-conduction band with an uniform electric field across the quantum-well structure can be characterized by a single-band effective mass Hamiltonian [1]

$$H_{\mathrm{c}}\left(k_{\mathrm{t}}, k_z = -i\hbar\frac{\partial}{\partial z}, F\right) = -\frac{\hbar^2}{2}\frac{\partial}{\partial z}\frac{1}{m_{\mathrm{c}}}\frac{\partial}{\partial z} + \frac{\hbar^2 k_{\mathrm{t}}^2}{2m_{\mathrm{c}}} + V_{\mathrm{c}}(z) + V_{\mathrm{c},\varepsilon}(z) + eFz, \quad (5.2)$$

where $\hbar$ is the Planck constant, m_{c} is the electron effective mass, k_{t} is the magnitude of wave vectors in the plane of quantum wells, $V_{\mathrm{c}}(z)$ is the intrinsic potentials, $V_{\mathrm{c},\varepsilon}$ is the energy shift due to strain effects, e is the elementary charge, and F is the strength of electric field. The electron subband energies and wavefunctions can be found by solving the Schrödinger equation

$$H_{\mathrm{c}}\left(k_{\mathrm{t}}, k_z = -i\frac{\partial}{\partial z}, F\right) f_n(k_{\mathrm{t}}, z, F) = E_n(k_{\mathrm{t}}, F) f_n(k_{\mathrm{t}}, z, F), \tag{5.3}$$

where E_n and f_n are the *n*th electron subband energy and wavefunction in the Γ-conduction band, respectively. For the valence band, we adopt the "*J*=4" Luttinger-Kohn Hamiltonian under the axial approximation to find the hole subband energies and wavefunctions in the valence band [1]

$$\mathbf{H}_{\mathrm{v,eff}}(k_{\mathrm{t}}, k_z = -i\frac{\partial}{\partial z}, F) = \begin{bmatrix} \mathbf{H}_{\mathrm{U}} & 0 \\ 0 & \mathbf{H}_{\mathrm{L}} \end{bmatrix}, \tag{5.4}$$

where $\mathbf{H}_{\mathrm{U}}$ and $\mathbf{H}_{\mathrm{L}}$ are upper and lower blocks of the "*J*=4" Luttinger-Kohn Hamiltonian given as follows

$$\mathbf{H}_{\mathrm{U}} = \begin{bmatrix} V_{\mathrm{v}}(z) - P - Q - eFz & -\tilde{R} \\ -\tilde{R}^{+} & V_{\mathrm{v}}(z) - P + Q + \Delta Q - eFz \end{bmatrix}, \tag{5.5}$$

$$\mathbf{H}_{\mathrm{L}} = \begin{bmatrix} V_{\mathrm{v}}(z) - P + Q + \Delta Q - eFz & -\tilde{R}^{+} \\ -\tilde{R} & V_{\mathrm{v}}(z) - P - Q - eFz \end{bmatrix}. \tag{5.6}$$

Those parameters can be found in chapter 3. Since the "*J*=4" Luttinger-Kohn Hamiltonian is block-diagonal, the upper and lower blocks can be solve independently

$$H_{\mathrm{U}} \begin{bmatrix} g_m^{(1)}(k_{\mathrm{t}}, z, F) \\ g_m^{(2)}(k_{\mathrm{t}}, z, F) \end{bmatrix} = E_m^{\mathrm{U}}(k_{\mathrm{t}}, F) \begin{bmatrix} g_m^{(1)}(k_{\mathrm{t}}, z, F) \\ g_m^{(2)}(k_{\mathrm{t}}, z, F) \end{bmatrix}, \tag{5.7}$$

$$H_{\mathrm{L}}\begin{bmatrix} g_m^{(3)}(k_{\mathrm{t}},z,F) \\ g_m^{(4)}(k_{\mathrm{t}},z,F) \end{bmatrix} = E_m^{\mathrm{L}}(k_{\mathrm{t}},F)\begin{bmatrix} g_m^{(3)}(k_{\mathrm{t}},z,F) \\ g_m^{(4)}(k_{\mathrm{t}},z,F) \end{bmatrix}, \tag{5.8}$$

where E_m^{U} and E_m^{L} are the eigenenergies and $g_m^{(1)}(k_{\mathrm{t}},z,F)$, $g_m^{(2)}(k_{\mathrm{t}},z,F)$, $g_m^{(3)}(k_{\mathrm{t}},z,F)$, and $g_m^{(4)}(k_{\mathrm{t}},z,F)$ are the corresponding eigenfunctions for the *m*th hole subband in the valence band. Those eigenfunctions will be used for the calculation of the moment matrix elements, the exciton binding energies, and the exciton oscillation strengths.

5.2.2 Excitonic absorption

The absorption coefficient in a quantum well consists of both continuum-state and discrete-state excitonic contributions. For the continuum-state contribution, the transverse electric (TE) and transverse magnetic (TM) excitonic absorption coefficients, including the Sommerfeld enhancement factor, $S(k_{\mathrm{t}})$, and the Lorentzian broadening function with a full-width-at-half-maximum (FWHM) linewidth, Γ, can be expressed as [1]

$$\alpha_{\mathrm{c}}^{\mathrm{TE}}(\hbar\omega) = \frac{\pi e^2}{n_{\mathrm{r}} c \varepsilon_0 m_0^2 \omega}\frac{1}{L_{\mathrm{w}}}\sum_{\sigma=\mathrm{U,L}}\sum_{n,m}\int \frac{k_{\mathrm{t}}\mathrm{d}k_{\mathrm{t}}}{2\pi} M_{nm}^{\sigma,\mathrm{TE}}(k_{\mathrm{t}}) S(k_{\mathrm{t}}) \times \frac{\Gamma/(2\pi)}{[E_n(k_{\mathrm{t}}) - E_m^{\sigma}(k_{\mathrm{t}}) - \hbar\omega]^2 + (\Gamma/2)^2}, \tag{5.9}$$

$$\alpha_{\mathrm{c}}^{\mathrm{TM}}(\hbar\omega) = \frac{\pi e^2}{n_{\mathrm{r}} c \varepsilon_0 m_0^2 \omega}\frac{1}{L_{\mathrm{w}}}\sum_{\sigma=\mathrm{U,L}}\sum_{n,m}\int \frac{k_{\mathrm{t}}\mathrm{d}k_{\mathrm{t}}}{2\pi} M_{nm}^{\sigma,\mathrm{TM}}(k_{\mathrm{t}}) S(k_{\mathrm{t}}) \times \frac{\Gamma/(2\pi)}{[E_n(k_{\mathrm{t}}) - E_m^{\sigma}(k_{\mathrm{t}}) - \hbar\omega]^2 + (\Gamma/2)^2}, \tag{5.10}$$

$$S(k_{\mathrm{t}}) = \frac{s_0}{1 + e^{-2\pi\sqrt{R_{\mathrm{y}}/E_{\mathrm{t}}}}}, \tag{5.11}$$

where $E_{\mathrm{t}} = \hbar^2 k_{\mathrm{t}}^2/(2m_{\mathrm{r}}^2)$ and $1 \le s_0 \le 2$ for quasi-two-dimensional QT structures. m_{r} is the reduced effective mass, m_0 is the free electron mass, c is the speed of light in free space, ε_0 is the permittivity of free space, $\hbar\omega$ is the photon energy, n_r is the background refractive index, L_w is the well width, and R_y is the exciton Rydberg energy. The average squared momentum matrix elements for TE polarization are [1], [8]

$$M_{nm}^{\mathrm{U,TE}}(k_\mathrm{t}, F) = \left[\frac{3}{2}\langle f_n|g_m^{(1)}\rangle^2 + \frac{1}{2}\langle f_n|g_m^{(2)}\rangle^2\right] M_\mathrm{b}^2, \tag{5.12}$$

$$M_{nm}^{\mathrm{L,TE}}(k_\mathrm{t}, F) = \left[\frac{3}{2}\langle f_n|g_m^{(4)}\rangle^2 + \frac{1}{2}\langle f_n|g_m^{(3)}\rangle^2\right] M_\mathrm{b}^2, \tag{5.13}$$

$$M_\mathrm{b}^2 = \frac{|\langle S|p_x|X\rangle|^2}{3} = \frac{m_0}{6}E_\mathrm{p}, \tag{5.14}$$

and those for TM polarization are

$$M_{nm}^{\mathrm{U,TM}}(k_\mathrm{t}, F) = 2\left[\langle f_n|g_m^{(2)}\rangle^2\right] M_\mathrm{b}^2, \tag{5.15}$$

$$M_{nm}^{\mathrm{L,TM}}(k_\mathrm{t}, F) = 2\left[\langle f_n|g_m^{(3)}\rangle^2\right] M_\mathrm{b}^2, \tag{5.16}$$

where M_b is the bulk momentum matrix element. Notice that a spin degeneracy of two has been included in the expressions of the TE and TM average squared momentum matrix elements.

For the contribution from discrete 1s-excitons, the TE and TM excitonic absorption coefficients with a Lorentzian broadening lineshape are given by [1]

$$\alpha_\mathrm{ex}^\mathrm{TE} = \frac{\pi e^2}{n_\mathrm{r} c \varepsilon_0 m_0^2 \omega}\frac{2}{L_\mathrm{w}}\sum_{n,m}\left(\frac{2}{\pi}\frac{1}{\Lambda^2}\right)\left|\hat{y}\cdot\mathbf{p}_{cv}\right|^2 \left|I_{nm}\right|^2 \frac{\Gamma/(2\pi)}{(E_\mathrm{x}-\hbar\omega)^2 + (\Gamma/2)^2}, \tag{5.17}$$

$$\alpha_\mathrm{ex}^\mathrm{TM} = \frac{\pi e^2}{n_\mathrm{r} c \varepsilon_0 m_0^2 \omega}\frac{2}{L_\mathrm{w}}\sum_{n,m}\left(\frac{2}{\pi}\frac{1}{\Lambda^2}\right)\left|\hat{z}\cdot\mathbf{p}_{cv}\right|^2 \left|I_{nm}\right|^2 \frac{\Gamma/(2\pi)}{(E_\mathrm{x}-\hbar\omega)^2 + (\Gamma/2)^2}, \tag{5.18}$$

where $E_\mathrm{x} = E_n - E_m + E_\mathrm{ex}$ is the exciton transition energy with E_ex being the exciton binding energy, Λ is a variational parameter, and I_{nm} is the wavefunction overlap integral between the *n*th electron state in the Γ-conduction band and the *m*th hole state in the valence band. The exciton binding energy and the variational parameter can be determined by the variation method [1], [9], [10]. The momentum matrix elements for TE polarization are [1]

$$|\hat{y} \cdot \mathbf{p}_{cv}|^2 = M_{\mathrm{b}}^2 \begin{cases} \frac{3}{2}, & \text{HH exciton} \\ \frac{1}{2}, & \text{LH exciton} \end{cases}, \tag{5.19}$$

and those for TM polarization are

$$|\hat{z} \cdot \mathbf{p}_{cv}|^2 = M_{\mathrm{b}}^2 \begin{cases} 0, & \text{HH exciton} \\ 2, & \text{LH exciton} \end{cases}. \tag{5.20}$$

After the continuum-state and discrete 1s-state excitonic absorption coefficients are obtained, the total absorption coefficients in a quantum well can be written as

$$\alpha^{\mathrm{TE}} = \alpha_{\mathrm{ex}}^{\mathrm{TE}} + \alpha_{\mathrm{c}}^{\mathrm{TE}}, \tag{5.21}$$

$$\alpha^{\mathrm{TM}} = \alpha_{\mathrm{ex}}^{\mathrm{TM}} + \alpha_{\mathrm{c}}^{\mathrm{TM}}. \tag{5.22}$$

5.2.3 Variational method for exciton problems

If a quantum is grown along the z direction, the Hamiltonian for an exciton in a quantum well can be expressed as

$$
\begin{aligned}
H =& H_\mathrm{e} + H_\mathrm{h} + H_\mathrm{eh}, && (5.23)\\
H_\mathrm{e} =& -\frac{\hbar^2}{2m_\mathrm{e}} + V_\mathrm{e}(z_\mathrm{e}) + eFz_\mathrm{e}, && (5.24)\\
H_\mathrm{h} =& -\frac{\hbar^2}{2m_\mathrm{h}} + V_\mathrm{h}(z_\mathrm{h}) - eFz_\mathrm{h}, && (5.25)\\
H_\mathrm{eh} =& -\frac{\hbar^2}{2m_\mathrm{r}}\nabla_r^2 - \frac{e^2}{4\pi\varepsilon r}, && (5.26)
\end{aligned}
$$

where H_e and H_h are the independent Hamiltonians for the electron and hole, respectively, H_eh represents the Coulomb interaction between the electron and hole, m_e is the electron effective mass, m_h is the hole effective mass, m_r is the reduced effective mass, V_e and V_h are the energy potentials along the QT growth direction for the electron and hole taking into account the effects of electric field and strain, respectively, z_e and z_h are the positions of the electron and hole along the QT growth direction, respectively, and r is the relative distance between the electron-hole pairs in the plane of quantum well. If there is no Coulomb interaction between the electron and hole, the electron and hole Hamiltonians can be solved independently. The presence of the Coulomb interaction leads to the binding effects and significantly contributes to the absorption coefficients. With the Hamiltonian in Eq. (5.23), the exciton energy and wavefunction can be found by solving the Schrödinger equation

$$H\Psi_{nm}(z_e, z_h, r) = E_{nm,\mathrm{x}}\Psi_{nm}(z_e, z_h, r), \qquad (5.27)$$

where $E_{nm,\mathrm{x}} = E_n + E_m - E^{\mathrm{ex}}_{nm}$ is the exciton transition energy with E^{ex}_{nm} being the exciton binding energy for the transition from the *m*th valence subband to the *n*th Γ-valley conduction subband, and $\Psi_{nm}(z_e, z_h, r)$ is the corresponding wavefunction. Equation (5.27) is difficult to solve analytically in a finite-barrier-high quantum well, and we will seek the solution numerically. The variation method is one of the most commonly used methods to find exciton binding energies and oscillation strengthes in a quantum well. It is relatively easy to use with reasonable accuracy when the width of quantum well is around or less then 10 nm. Since the 1s excitons behave like $e^{-r/(a_0)}$ or $e^{-r/(2a_0)}$, one can assume the trial wavefuntion for 1s exciton as [1], [9], [10]

$$\Psi_{nm}(r, z_e, z_h) = \phi(r) f_n(z_e) h_m(z_h) = \sqrt{\frac{2}{\pi}\frac{1}{\Lambda}} \exp\left[-\frac{r}{\Lambda}\right] f_n(z_e) h_m(z_h), \tag{5.28}$$

where Λ is a variational parameter, $f_n(z_e)$ is the *n*th electron subband wavefunction in the Γ-conduction band, and $h_m(z_h)$ is the *mth* hole subband wavefunction in the valence band. Substituting Eq. (5.28) into Eq. (5.27), multiplying the both sides of the equation by $\Psi_{n'm'}$, and integrating the equation over the whole space, the exciton binding energy can be expressed as [1]

$$E^{\mathrm{ex}}_{nm}(\Lambda) = \frac{\hbar^2}{2m_{\mathrm{r}}\Lambda^2} - \frac{e^2}{4\pi\varepsilon}\frac{4}{\Lambda^2}\int dz_{\mathrm{e}} |f_n(z_{\mathrm{e}})|^2 \int dz_{\mathrm{h}} |h_m(z_{\mathrm{h}})|^2 \int_0^\infty r\mathrm{d}r \frac{e^{-2r/\Lambda}}{\sqrt{r^2 + (z_{\mathrm{e}} - z_{\mathrm{h}})^2}}. \tag{5.29}$$

Thus, by minimizing the excition binding energy, that is, $\frac{\mathrm{d}}{\mathrm{d}\Lambda}E^{\mathrm{ex}}_{nm}(\Lambda) = 0$, one can determine the variational parameter Λ and obtain the exciton binding energy E^{ex}_{nm}. In addition, the exciton oscillation strength is

$$|\phi(r=0)|^2 = \left(\frac{2}{\pi}\frac{1}{\Lambda^2}\right), \tag{5.30}$$

which will be used for the calculation of absorption coefficients from discrete 1s-state contribution .

5.2.4 Polarization-dependent optical confinement factor

For MQW EA waveguide modulators, since the quantum wells only occupy partial volume in the waveguide and different waveguide modes experience different amounts of optical absorption, the optical confinement factors are necessary to convert the material absorption coefficients into the modal absorption coefficients for waveguide modes of interest. Besides, since the excitonic absorptions due to the direct band-edge excitonic transitions are anisotropic, two optical confinement factors are necessary to properly define the contributions from the TE and TM material absorption coefficients to the modal absorption coefficients for the waveguide modes. If a guided mode propagates along the x direction and the QT growth direction is along the z direction, the TE and TM optical confinement factors for the wells can be expressed as [11, 12, 13]

$$\Gamma_{\text{wells}}^{\text{TE}} = \frac{\frac{n_{\text{w}}}{2\eta_0}\int\int_{\text{wells}}\left(|E_x|^2+|E_y|^2\right)dydz}{\frac{1}{2}\int_{-\infty}^{\infty}\int_{-\infty}^{\infty}\text{Re}[\mathbf{E}\times\mathbf{H}^*]\cdot\hat{x}dydz}, \tag{5.31}$$

$$\Gamma_{\text{wells}}^{\text{TM}} = \frac{\frac{n_{\text{w}}}{2\eta_0}\int\int_{\text{wells}}|E_z|^2dydz}{\frac{1}{2}\int_{-\infty}^{\infty}\int_{-\infty}^{\infty}\text{Re}[\mathbf{E}\times\mathbf{H}^*]\cdot\hat{x}dydz}, \tag{5.32}$$

where n_{w} is the refractive index of the wells, and $\eta_0 = \sqrt{\mu_0/\varepsilon_0}$ is the intrinsic impedance. In addition to the excitonic absorptions due to the direct band-edge transitions in the wells, the material absorption due to free-carrier absorption in the waveguide also contribute to the modal absorption coefficients. Since free-carrier absorption is isotropic, only one optical confinement factor, which is the sum of the TE and TM optical confinement factors, is necessary for layer i

$$\Gamma_i = \frac{\frac{n_i}{2\eta_0}\int\int_i |\mathbf{E}|^2 dydz}{\frac{1}{2}\int_{-\infty}^{\infty}\int_{-\infty}^{\infty} \mathrm{Re}[\mathbf{E}\times\mathbf{H}^*]\cdot\hat{x}dydz}, \tag{5.33}$$

where n_i is the refractive index of the *i*th layer.

5.2.5 Extinction ratio and insertion loss

Extinction ratio and insertion loss are two of the most representative parameters of a modulator. The former describes the ratio of the transmitted optical powers at the optical on-state to the optical off-state, while the later stands for the optical power loss due to material absorption at the optical on-state. If we define the optical on-state and off-state in an electroabsorption modulator are at a zero bias ($V_{\text{on}} = 0$) and at a reverse bias of V_{r} ($V_{\text{off}} = V_{\text{r}}$), the extinction ratio at wavelength λ in decibels is given by [1], [14]

$$\begin{aligned} R(\lambda,\ V_{\text{r}}) &= 10\times\log\frac{T(\lambda,\ V_{\text{on}}=0)}{T(\lambda,\ V_{\text{off}}=V_{\text{r}})} \\ &= 4.343\Big\{\Gamma^{\text{TE}}_{\text{wells}}\left[\alpha^{\text{TE}}(\lambda,\ V_{\text{r}})-\alpha^{\text{TE}}(\lambda,0)\right]+\Gamma^{\text{TM}}_{\text{wells}}\left[\alpha^{\text{TM}}(\lambda,\ V_{\text{r}})-\alpha^{\text{TM}}(\lambda,\ 0)\right]\Big\}L \end{aligned} \tag{5.34}$$

where $T(\lambda,\ V_{\text{off}} = V_{\text{r}})$ and $T(\lambda,\ V_{\text{on}} = 0)$ are the transmission coefficients at wavelength λ at the optical off-state and on-state, respectively; $\alpha^{\text{TE}}(\lambda,\ V_{\text{r}})$, $\alpha^{\text{TM}}(\lambda,\ V_{\text{r}})$, $\alpha^{\text{TE}}(\lambda,\ 0)$, and $\alpha^{\text{TM}}(\lambda,0)$ are the TE- and TM-polarized absorption coefficients at wavelength λ at the optical off-state and on-state, respectively; and L is the waveguide length. On the other hand, the insertion loss at wavelength λ attributed to the direct band-edge excitonic absorption in the QWs and material absorption due to free carrier absorption in the n- and

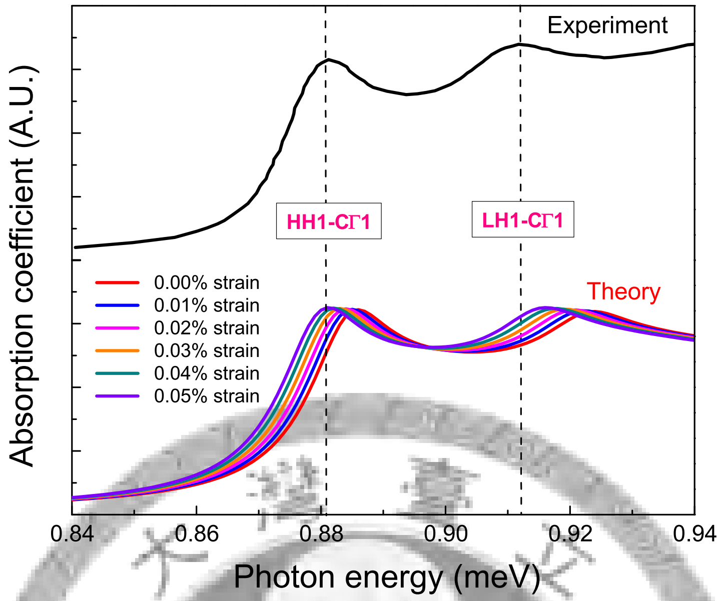

Figure 5.4: Comparison of the experimental absorption spectrum of Ge/SiGe QWs [1] and our calculated absorption spectra at zero bias. The calculated absorption spectra with different levels of tensile strain in the $\mathrm{Si}_{0.1}\mathrm{Ge}_{0.9}$ buffer layer are also displayed.

p-contacts, in decibels, is given by [1], [14]

$$\begin{aligned} L_{\mathrm{in}}(\lambda) &= -10 \times \log\left[T(\lambda,\ V_{\mathrm{on}}=0)\right] \\ &= 4.343\left[\Gamma_{\mathrm{wells}}^{\mathrm{TE}}\alpha^{\mathrm{TE}}(\lambda,\ 0) + \Gamma_{\mathrm{wells}}^{\mathrm{TM}}\alpha^{\mathrm{TM}}(\lambda,\ 0) + \Gamma_{\mathrm{n}}\alpha_{\mathrm{n}}(\lambda) + \Gamma_{\mathrm{p}}\alpha_{\mathrm{p}}(\lambda)\right] L, \end{aligned} \quad (5.35)$$

where α_{n} and α_{p} are the material absorptions due to free-carrier absorption in the n- and p-contact regions, respectively, and Γ_{n} and Γ_{p} are the optical confinement factors of the n-contact and p-contact regions, respectively, as defined in Eq. (5.33).

5.3 Quantum-confined Stark effects in Ge/SiGe quantum wells

To validate our model, we first compare our theoretical results with the experimental data for QCSE in Ge/Si$_{0.15}$Ge$_{0.85}$ QWs, which consists of ten pairs of 10-nm-thick Ge wells and 16-nm-thick Si$_{0.15}$Ge$_{0.85}$ barriers on a silicon substrate via a Si$_{0.1}$Ge$_{0.9}$ buffer layer [1]. Figure 5.4 shows our calculated absorption spectra compared with the experimental data at zero bias, corresponding to a built-in electric field $F_0 = 16.3\ \mathrm{kV/cm}$. The experimental data show that the HH1-CΓ1 and the LH1-CΓ1 exciton peaks are situated at about 0.881 eV and 0.91 eV, respectively. Clearly, our theoretical results show good agreements with the experimental data, except for a small blue shift of $\sim$2 meV. The error may possibly come from: (1) the error of the deformation potentials used in our calculation, and (2) the strain condition of the $\mathrm{Si_{0.1}Ge_{0.9}}$ buffer layer. Indeed, the buffer layer in this device was grown at a low temperature of $400^{\circ}\mathrm{C}$ and then thermally annealed at $750^{\circ}\mathrm{C}$ and $850^{\circ}\mathrm{C}$ before the growth of the QWs. Several papers have indicated that such a process may induce tensile strain due to the difference in thermal expansion coefficients between Si and Ge [15], [16], and a tensile-strain as high as 0.25% has been shown by such a thermally annealing process. Thus, in Fig. 5.4, we also plot the calculated absorption spectra at different tensile strain levels in the SiGe buffer layer. As the tensile strain increases, the whole absorption spectra shifts toward lower photon energies. At a tensile strain of 0.05% in the buffer layer, our calculated CΓ1-HH1 exciton peak shifts to 0.881 eV and the calculated absorption spectrum agrees with the experimental one. Thus, we assume that the buffer layer is subject to a 0.05% tensile strain in the following calculations.

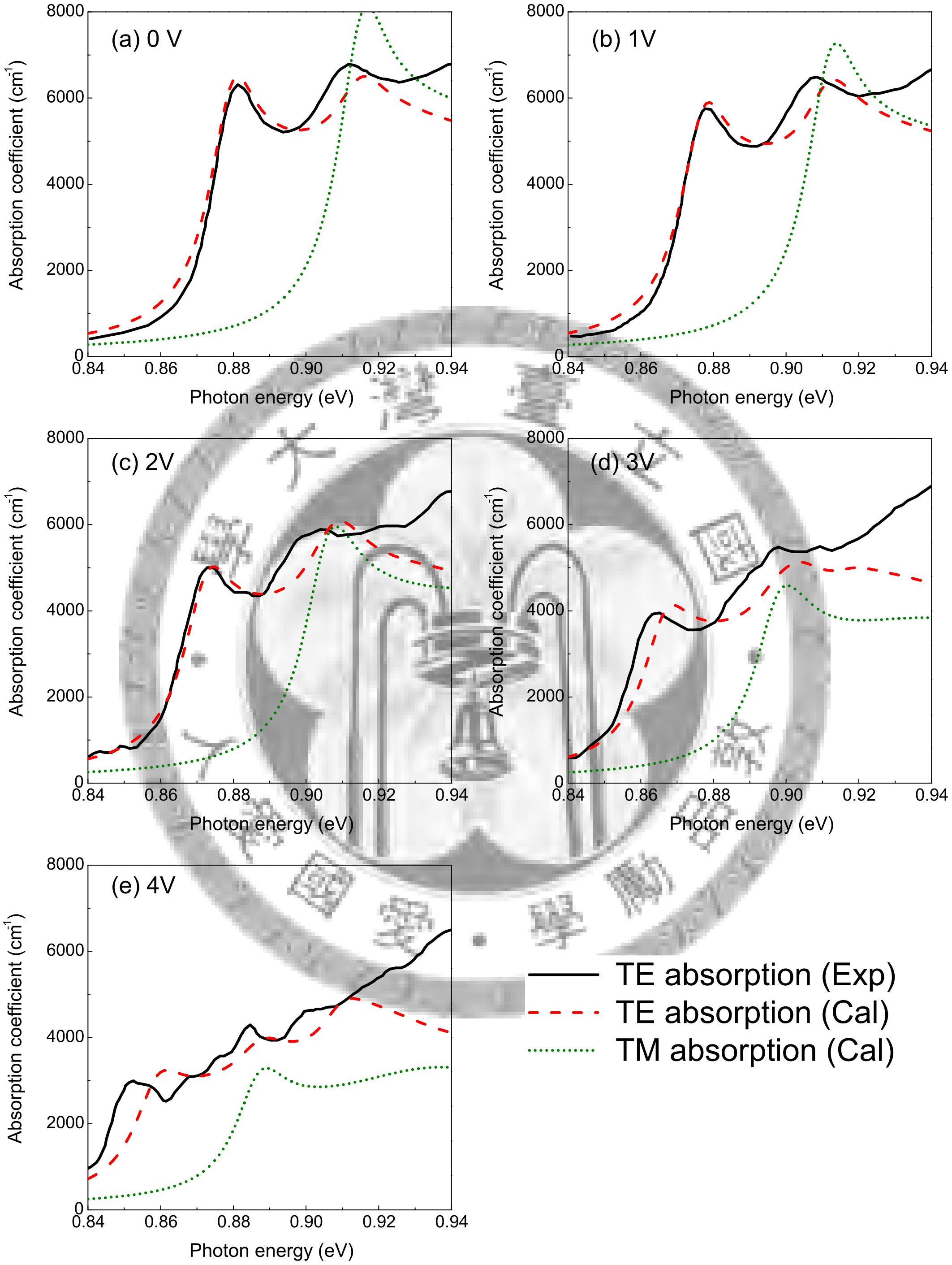

Figure 5.5: Comparison of the experimental [1] and our calculated absorption spectra at different reverse biases for the Ge/SiGe QWs. A 0.05% tensile strain in the buffer is assumed.

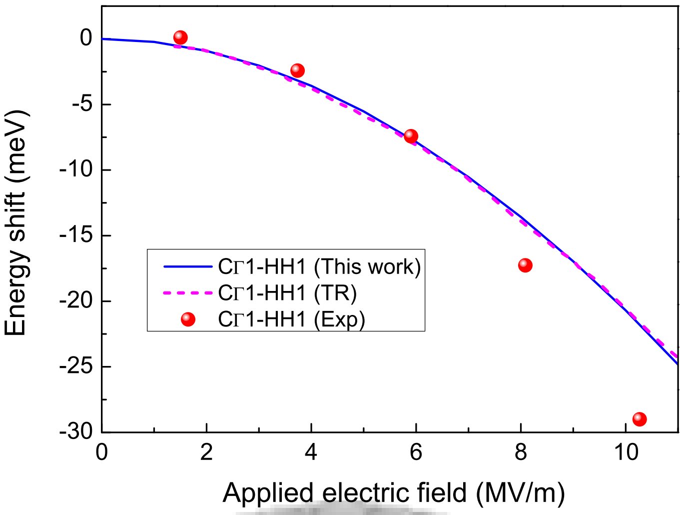

Figure 5.6: Calculated Stark shifts for the HH1-CΓ1 transition compared with those from experimental data and tunneling resonance calculations [1].

Figure 5.5 shows the comparison between our calculated and the experimental absorption spectra in the Ge/SiGe QWs at different reverse biases, where the buffer is assumed to have a 0.05% tensile strain. Here the constant s_0 is determined to be 1.2 to obtain best fitting curves and will be used for the later calculations. The calculated TM-polarized absorption spectra are also present. Our theoretical results show excellent agreements with the experimental results from 0 V to 2 V. However, at reverse biases of 3 V and 4 V, the exciton peaks of the experimental data shifts faster than those of our calculated results. It is believed thermal effects due to the high-voltage operation that significantly reduces the bandgaps. Figure 5.6 shows the calculated HH1-CΓ1 exciton shift due to QCSE compared with those form experimental data and tunneling resonance (TR) calculations [1]. Our calculated curve is almost superimposed with the tunneling resonance calculations, but both the calculated Stark shifts are smaller than the experimental data at high reverse biases. Based on the excellent agreements between our theoretical results and the experimental data, our developed model is adequate for the description of QCSE in a quantum well and will be used to design new group-IV MQW EA waveguide modulators.

5.4 Toward Silicon-based electroabsorption modulators at 1550 nm wavelength: tensile-strained Ge/SiGeSn quantum wells for electroabsorption modulators

Although Ga has a direct bandgap of about 0.8 eV at room temperature and the Ge/SiGe QT systems exhibit a strong quantum-confined Stark effect, the Ge/SiGe QT modulators can only operate in 1440-1460 nm [1], [7]. This is due to the large difference in lattice constant between Si and Ge that induces a compressive strain when growing Ge wells on a silicon substrate via a SiGe buffer layer. The unwanted compressive strain in the Ge wells, together with the quantum-well confinement energy, significantly increase the direct transition energy of the Ge wells from its unstrained direct bandgap of 0.8 eV to 0.88 eV. As a result, the wavelengths of optimal extinction ratio shift to 1440-1460 nm, which is neither compatible with the most important telecom window of optical fiber around 1300 nm nor 1550 nm wavelength. Although this unwanted compressive strain in the Ge wells can be reduced to near zero by decreasing the mole fraction of Si in the buffer layer, The SiGe barriers will be subject to a large tensile-strain. As a result, a strain-balanced structure is not possible so that significant strain-misfit dislocations occurs. In this case, using wide Ge wells operating at a high temperature can red shift the absorption spectra to achieve C-band operation [17].

To make the Ge QT modulator compatible with the fiber-optic telecommunications, our approach is to introduce tensile strain into Ge wells, that is, growing tensile-strained Ge wells. Tensile strain can effectively reduce the direct bandgap of the Ge wells to compensate the quantum-well confinement energy for 1550 nm operation. We employ compressive-strained $\mathrm{Si}_x\mathrm{Ge}_y\mathrm{Sn}_{1-x-y}$ barriers to compensate the tensile strain in the Ge

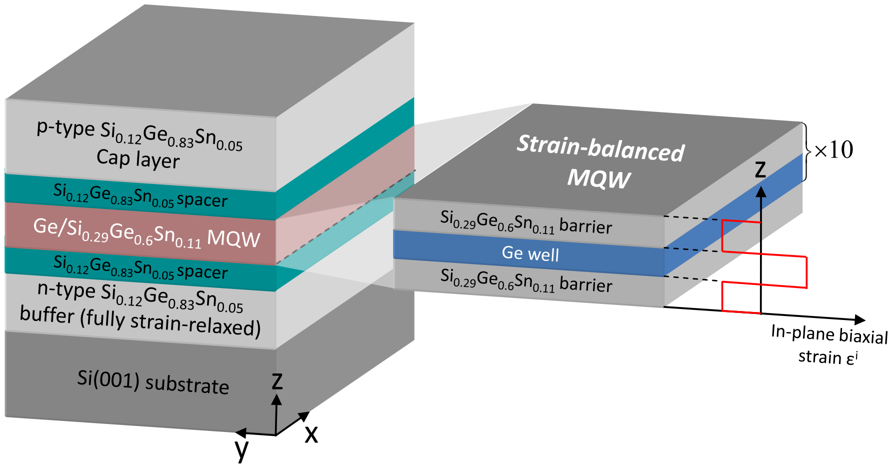

Figure 5.7: Schematic structure of a strained-balanced Ge/$\mathrm{Si_{0.29}Ge_{0.6}Sn_{0.11}}$ MQW with alternating growth of tensile-strained Ge wells and compressive-strained $\mathrm{Si_{0.29}Ge_{0.6}Sn_{0.11}}$ barriers. The MQW structure sandwiched by $\mathrm{Si_{0.12}Ge_{0.83}Sn_{0.05}}$ spacers is grown on a silicon substrate via a fully strain-relaxed $\mathrm{Si_{0.12}Ge_{0.83}Sn_{0.05}}$ buffer layer.

wells, leading to a strain-balanced MQW structure to reduce strain-misfit dislocations. Thus, a multiple-quantum-well system with many periods is achievable to further enhance the performance of electroabsorption modulators. Additionally, the tensile strain reduces the energy difference between the first heavy-hole (HH) and light-hole (LH) subbands to achieve polarization-insensitive operation, which is one of the most desirable features in optical modulators for telecommunications. With adequate adjustments of the well width, the amount of tensile strain in the Ge wells, and the waveguide geometry, polarization-insensitive operation at 1550 nm wavelength in this MQW EA waveguide modulator is achievable.

5.4.1 Material design: tensile-strained Ge/$\mathrm{Si}_x\mathrm{Ge}_y\mathrm{Sn}_{1-x-y}$ MQW

Figure 5.7 schematically shows our proposal of a tensile-strained Ge/$\mathrm{Si_{0.29}Ge_{0.6}Sn_{0.11}}$ MQW structure for EA waveguide modulators, where the crystal growth direction is along the z direction. A fully strain-relaxed $\mathrm{Si_{0.12}Ge_{0.83}Sn_{0.05}}$ buffer layer is grown on a (001)-oriented silicon substrate as the virtual substrate for the subsequent growth of quantum wells. The buffer layer is also n-type doped at a level of $5 \times 10^{18}\ \mathrm{cm}^{-3}$ as the bottom contact. The direct growth of doped, strain-relaxed SiGeSn layers on a Si(001) substrate has been reported recently [2]. Subsequently, a 50-nm spacer layer of intrinsic $\mathrm{Si}_{0.12}\mathrm{Ge}_{0.83}\mathrm{Sn}_{0.05}$ is grown on the buffer layer. Then ten pairs of Ge/$\mathrm{Si}_{0.29}\mathrm{Ge}_{0.6}\mathrm{Sn}_{0.11}$ quantum wells, that is, ten Ge wells and eleven $\mathrm{Si}_{0.29}\mathrm{Ge}_{0.6}\mathrm{Sn}_{0.11}$ barriers, are grown, followed by another 50-nm spacer layer of intrinsic $\mathrm{Si}_{0.12}\mathrm{Ge}_{0.83}\mathrm{Sn}_{0.05}$. Finally, the entire structure is capped by a p-type $\mathrm{Si}_{0.12}\mathrm{Ge}_{0.83}\mathrm{Sn}_{0.05}$ layer with a p-doping concentration of $1 \times 10^{19}\ \mathrm{cm}^{-3}$ as the top contact. Because the $\mathrm{Si}_{0.12}\mathrm{Ge}_{0.83}\mathrm{Sn}_{0.05}$ buffer layer is fully strain-relaxed, the in-plane lattice constants of the Ge wells and $\mathrm{Si}_{0.29}\mathrm{Ge}_{0.6}\mathrm{Sn}_{0.11}$ barriers will be forced to equal to that of the buffer layer. The lattice constant of the Ge wells is smaller than that of the $\mathrm{Si}_{0.12}\mathrm{Ge}_{0.83}\mathrm{Sn}_{0.05}$ buffer layer, giving rise to an in-plane biaxial tensile strain of 0.254% in the Ge wells. On the other hand, the $\mathrm{Si}_{0.29}\mathrm{Ge}_{0.6}\mathrm{Sn}_{0.11}$ barriers have a lattice constant larger than that of the buffer layer, so they are subject to a 0.200% compressive strain to compensate for the tensile strain in the Ge wells. The well width is set to 100 Å to maintain proper electron-hole wavefunction overlaps for moderate excitonic absorption. The barrier width is determined to be 120 Å by the strain-balanced condition that minimizes the total strain energy. As the total strain energy is minimized in the MQW region, the generation of strain-misfit dislocations can be reduced to improve the material quality.

5.4.2 Theoretical results and discussions

Figure 5.8(a) shows the various band profiles and the squared wavefunctions of the confined states for the tensile-strained Ge well sandwiched between the compressive-strained $\mathrm{Si}_{0.29}\mathrm{Ge}_{0.6}\mathrm{Sn}_{0.11}$ barriers in the absence of an electric field. The zero energy is

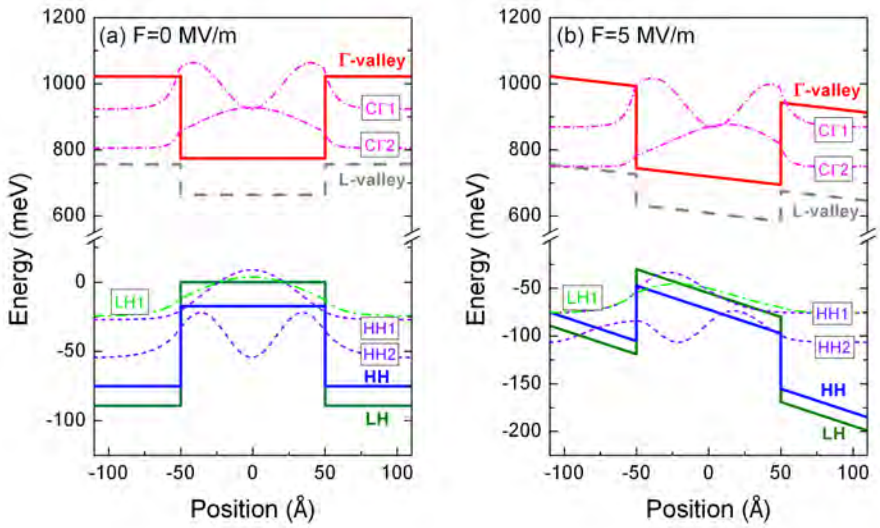

Figure 5.8: Band structures and squared wavefunctions of the confined states for the tensile-strained Ge well sandwiched between the compressive-strained $\mathrm{Si_{0.29}Ge_{0.6}Sn_{0.11}}$ barriers at electric fields of (a) 0 MV/m and (b) 5 MV/m applied along the QT growth direction.

set to the QT LH band edge. Because both the conduction band minimum and the valence band maximum are in the Ge well region, this tensile-strained Ge/$\mathrm{Si_{0.29}Ge_{0.6}Sn_{0.11}}$ quantum-well has a type-I alignment, which is particularly important for QT modulators because of the improved electron-hole wavefunction overlaps in the well region. There are two confined electron states in the Γ-conduction band, while two HH states and one LH state in the valence band. The 0.254% tensile strain in the Ge well reduces the direct bandgap to 774.4 meV to compensate the quantum-well confinement energy for 1550 nm operation. In addition, the tensile strain lifts up the LH band edge above the HH band edge by 17.2 meV. As a result, the first LH subband (LH1) is 2.7 meV higher than the first HH subband (HH1) in the absence of an electric field. This near degeneracy between the HH1 and LH1 states due to the tensile strain in the Ge well helps achieve polarization-insensitive operation in the modulator. Figure 5.8(b), on the other hand, shows the various band lineups and the squared wavefunctions of the confined states at an electric field $F = 5\ \mathrm{MV/m}$ applied along the QT growth direction. In this case, the $\mathrm{C\Gamma 1}$ and $\mathrm{C\Gamma 2}$

states are almost completely confined in the Ge well due to the sufficiently high conduction band offset. In the valence band, the HH1 and LH1 states are well confined in the Ge well, while the HH2 state has an nonvanishing wavefunction tailing into the left barrier. The applied electric field tilts the QT potential profiles and moves the electron and hole wavefunctions in opposite directions, reducing the transition energies and the wavefunction overlap integrals of the HH1-$C\Gamma1$ and LH1-$C\Gamma1$ transitions.

Figure 5.9 shows the TE and TM excitonic absorption spectra due to the direct band-edge excitonic absorptions under different electric fields at room temperature. Here s_0 is set to 1.2 while the FWHM linewidth Γ is set to 14 meV by the temperature-dependent analysis of FWHM in Ge/SiGe QWs [3]. At a zero electric field, the HH1-$C\Gamma1$ and LH1-$C\Gamma1$ exciton peaks are situated at 829.3 meV and 826.7 meV, respectively. Meanwhile, the TE and TM absorption coefficients at 1550 nm are as low as 792.4 cm^{-1} and 892.0 cm^{-1}, respectively, which lead to a low insertion loss for this modulator. As the magnitude of the electric field increases, both the TE and TM absorption spectra shift toward lower photon energies and can sweep the target photon energy of 0.8 eV for 1550 nm operation. At an electric field of 10 MV/m, the QCSE red shifts the absorption spectra and significantly increases the TE and TM absorption coefficients at 1550 nm to 2645.9 cm^{-1} and 2703.5 cm^{-1}, respectively, making the Ge QT more absorptive to achieve effective modulation at 1550 nm.

The near degeneracy between the HH1 and LH1 states can build the basis for polarization-insensitive operation in this MQW EA waveguide modulator. However, the near identity of the electric-field-dependent TE and TM material absorption coefficients at desired wavelengths is more important to achieve polarization-insensitive operation. Indeed, the excitonic absorption coefficients due to QCSE depend on the carrier effective

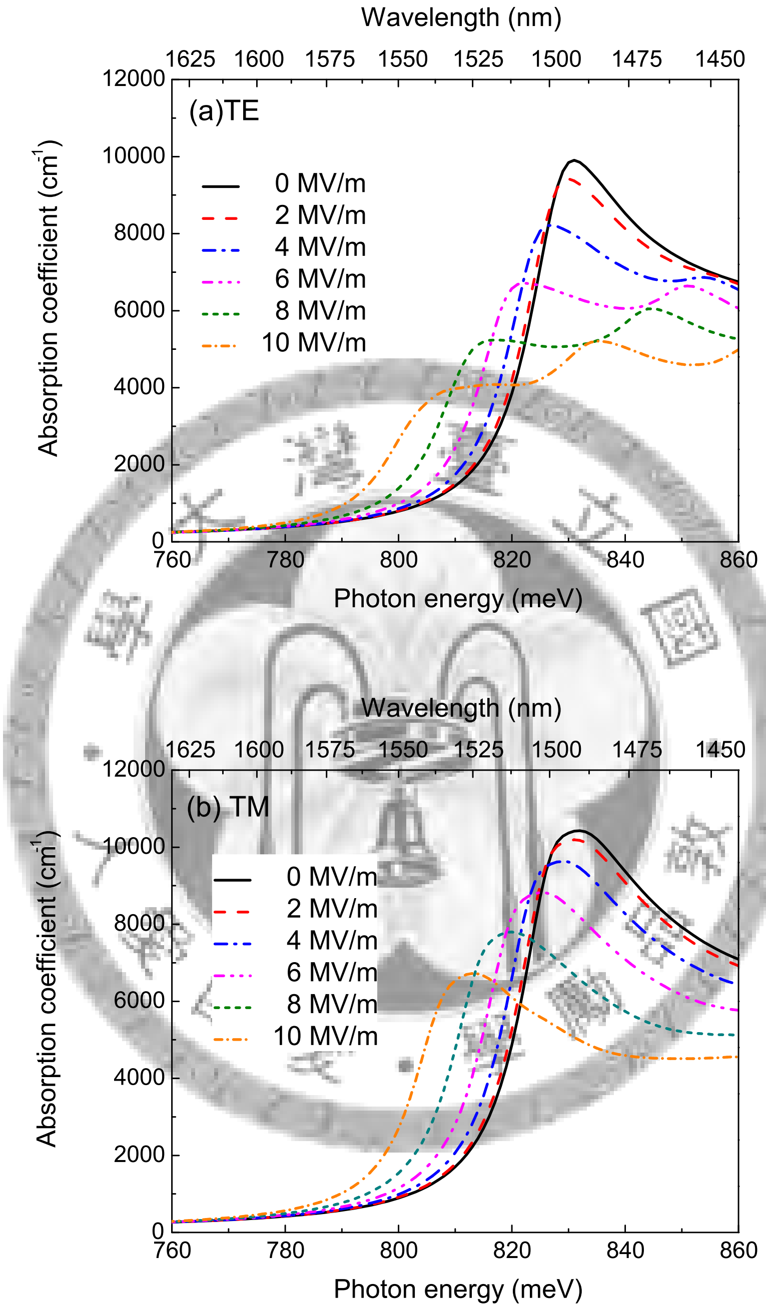

Figure 5.9: Electric-field-dependent (a) TE and (b) TM excitonic absorption spectra for the tensile-strained Ge/$Si_{0.29}Ge_{0.6}Sn_{0.11}$ QT. In the absence of an electric filed, the HH1-CΓ1 and the LH1-CΓ1 exciton peaks are 29.3 meV and 26.7 meV higher than the target photon energy of 0.8 eV, respectively. When the strength of the applied electric filed increases, the excitonic peaks shift toward lower photon energies, and both the TE and TM material absorption coefficients at 1550 nm significantly increase.

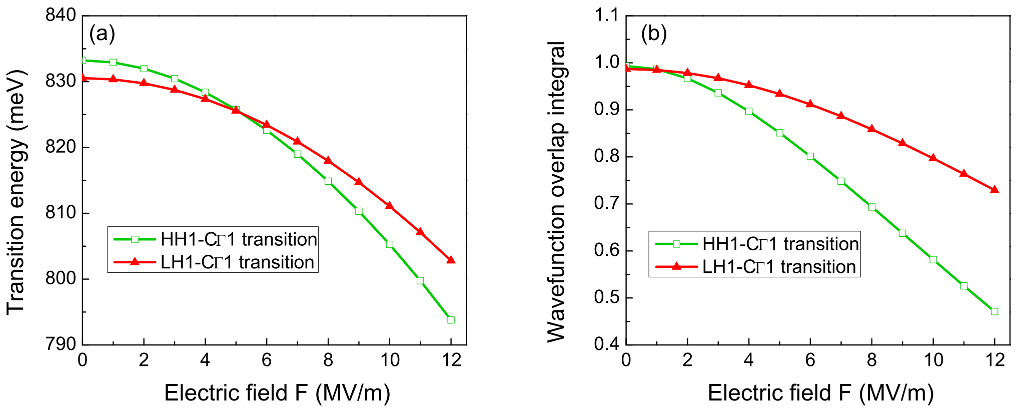

Figure 5.10: (a) Electric-field-dependent HH1-CΓ1 and LH1-CΓ1 transition energies. (b) Wavefunction overlap integrals of the HH1-CΓ1 and LH1-CΓ1 transitions as a function of electric field.

masses, electron-hole wavefunction overlaps, oscillation strengths, and broadening effects. Those effects have to be adequately engineered to compensate each other to ensure the near identity of the TE and TM material absorption coefficients at desired wavelengths for polarization-insensitive operation. Figure 5.10(a) shows the HH1-CΓ1 and LH1-CΓ1 transition energies as a function of electric field. Both the HH1-CΓ1 and LH1-CΓ1 transitions show quadratic-dependence to the applied electric field. Although the HH1-CΓ1 transition energy is 2.7 meV larger than the LH1-CΓ1 transition energy in the absence of an electric field, the HH1-CΓ1 transition energy diminishes more rapidly than the LH1-CΓ1 transition energy. This is owing to the larger effective mass along the QT growth direction of the HH1 state ($m_{\mathrm{hh},z} = 0.204\ m_0$) than that of the LH1 state ($m_{\mathrm{lh},z} = 0.0457\ m_0$). The HH1-CΓ1 exciton peak can shift to 0.8 eV at an electric field of about 11 MV/m, while the LH1-CΓ1 exciton peak requires a higher electric field of about 12.5 MV/m to sweep this value. Figure 5.10(b) shows the spatial wavefunction overlap integrals of the HH1-CΓ1 and LH1-CΓ1 transitions as a function of electric field. At zero electric field, both the LH1-CΓ1 and HH1-CΓ1 transitions have wavefunction overlap integrals of almost unity due to the sufficiently large band offsets provided by the barriers.

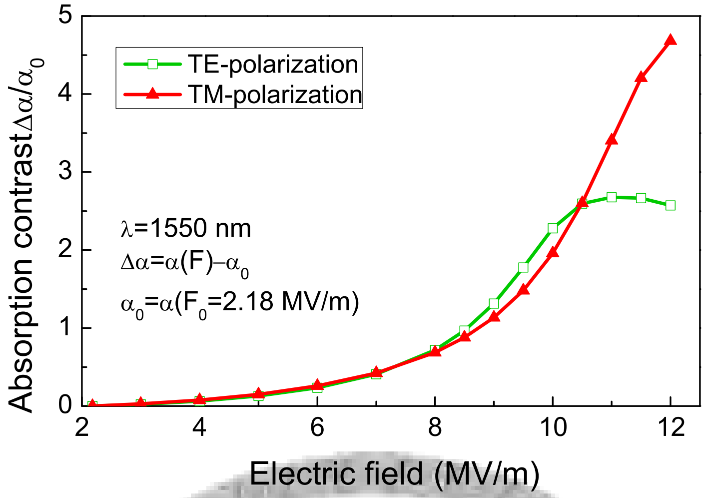

Figure 5.11: TE and TM absorption contrasts for the Ge QT at 1550 nm as a function of electric field, showing good polarization-insensitive modulation behavior up to $F = 10.5\ \mathrm{MV/m}$.

However, the spatial wavefunction overlap integral of the HH1-CΓ1 transition falls off faster with the electric field than that of the LH1-CΓ1 transition because of the twofold reasons: (1) The HH band offset is smaller than the LH band offset due to the strain effect in the QT. As a result, the HH1 wavefunction penetrates into the barrier region more deeply with the electric field than the LH1 wavefunction. (2) The HH1 wavefunction becomes more asymmetric about the center of the QT than the LH1 wavefunction with the increasing strength of electric field because of $m_{\mathrm{hh},z} > m_{\mathrm{lh},z}$. In other words, the HH1-CΓ1 transition has a larger energy shift but its spatial wavefunction overlap integral also decreases faster with the increasing strength of electric field than those of the LH1-CΓ1 transition. With the compensation between the two effects (electric-field-dependent transition energy shifts and wavefunction overlap integrals), nearly identical TE and TM material absorption coefficients in the QT are achievable.

Figure 5.11 shows the TE- and TM-polarized absorption contrasts, $\Delta\alpha/\alpha_0$, at $\lambda = 1550\ \mathrm{nm}$ for the tensile-strained Ge/Si$_{0.29}$Ge$_{0.6}$Sn$_{0.11}$ QT, where $\Delta\alpha = \alpha(F) - \alpha_0$ is the change in absorption coefficient due to QCSE, and α_0 is the absorption coefficient

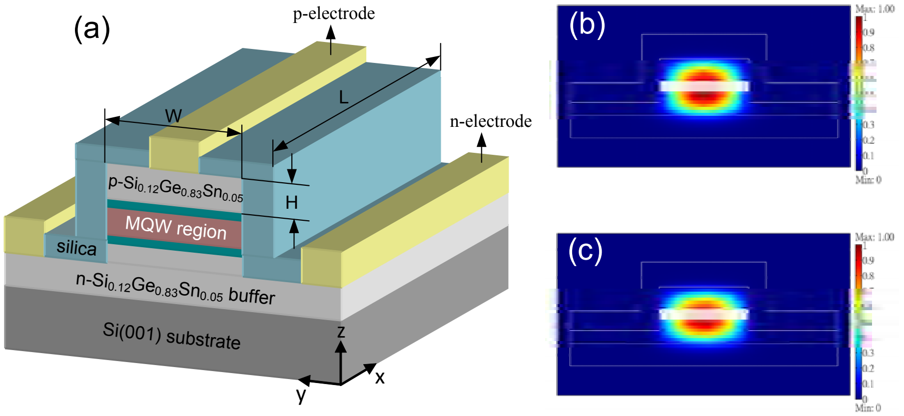

Figure 5.12: (a) Schematic diagram of our designed silica ridge waveguide structure for index guidance. The silica ridge structure has a small refractive index compared to those of the semiconductors and can provide the necessary optical confinement for the guided modes. (b) Normalized E_y field distribution for the quasi-TE fundamental mode and (c) normalized E_z field distribution for the quasi-TM fundamental mode at $\lambda = 1550$ nm with $H = 400$ nm and $W = 1.5$ μm. With the peak fields located near the MQW region, the enhanced optical confinement factors for the wells can improve the extinction ratio of the modulator.

at the optical on-state (zero bias voltage), corresponding to a built-in electric field $F_0 = 2.18$ MV/m estimated by the depletion approximation [20]. With the effective compensation between the various effects, the absorption contrast shows little polarization dependence up to $F = 10.5$ MV/m, corresponding to an extinction contrast of about 2.6, which can produce a high extinction ratio and low insertion loss for the modulator.

Figure 5.12(a) shows our waveguide design, where the width of the ridge structure is W, the thickness of the $Si_{0.12}Ge_{0.83}Sn_{0.05}$ cap layer is H, and the device length is L, respectively. We use silica as the ridge structure for index guidance because the refractive index of silica at $\lambda = 1550$ nm ($n_{\text{silica}} = 1.4438$ [21]) is much smaller that those of Si, Ge, and α-Sn ($n_{\text{Si}} = 3.4784$, $n_{\text{Ge}} = 4.275$, $n_{\text{Sn}} = 4.885$ [21], [22]). The large contrast in refractive index between the silica ridge structure and the semiconductors can effectively confine the waveguide modes. We use the finite element method (FEM) to calculate the waveguide modes and their field distributions. The waveguide width, W, is set to 1.5 μm and the thickness of the cap layer, H, will be optimized for polarization-insensitive operation. Figures 5.12(b) and 5.12(c) show the normalized E_y and E_z field distributions for the quasi-TE fundamental mode, HE_{11} mode (the dominant fields are E_y and H_z), and quasi-TM fundamental mode, EH_{11} mode (the dominant fields are E_z and H_y), respectively, with $H = 400$ nm. It is clear to see that the silica ridge structure acts as the upper and side cladding layers while the silicon substrate plays the role of the lower cladding layer, showing a good optical confinement for the waveguide modes. With the careful design of the waveguide geometry, the peak electric fields are located around the MQW region, leading to enhanced optical confinement factors for the wells. As a result, Table 5.1 tabulates the free-carrier absorption calculated by the Drude-Lorentz equation [23], [24], and the TE and TM optical confinement factors at $\lambda = 1550$ nm of the various regions for the EH_{11} and HE_{11} modes with $H = 400$ nm. For the wells, the TE optical confinement factor for the EH_{11} mode is as high as 12.7005% while the TM optical confinement factor for the HE_{11} mode is 12.0431%, leading to an improved extinction ratio for the modulators. On the other hand, the optical confinement factors of the n- and p-contacts are much larger than those of the wells due to their relatively larger thicknesses. Nevertheless, the material absorption in the n- and p-contacts due to free-carrier absorption is small because of the high carrier mobilities in those Ge-rich semiconductors. As a result, the modal absorption attributed to the material absorptions in the n- and p-contacts is insignificant.

Near identity of TE and TM material absorption coefficients in QWs alone is not sufficient to achieve polarization-insensitivity in a MQW EA waveguide modulator. The optical confinement factors of the various regions in the waveguide should be adequately engineered to ensure the nearly identical modulation behavior at desired wavelengths for both the TE and TM modes. To find out the optimal value of H for polarization-insensitive

Table 5.1: Free-carrier absorption, and TE and TM optical confinement factors at $\lambda = 1550$ nm for the HE$_{11}$ and EH$_{11}$ modes of the various regions with $W = 1.5\ \mu\mathrm{m}$ and $H = 400$ nm.

		HE$_{11}$ mode		EH$_{11}$ mode	
	Free-carrier absorption (cm^{-1})	Γ_i^{TE} (%)	Γ_i^{TM} (%)	Γ_i^{TE} (%)	Γ_i^{TM} (%)
wells	N/A	12.7005	0.0001	0.0198	12.0431
n-contact	17.03	41.8735	0.0152	0.8221	41.2335
p-contact	20.02	18.3031	0.0011	0.8384	15.2997

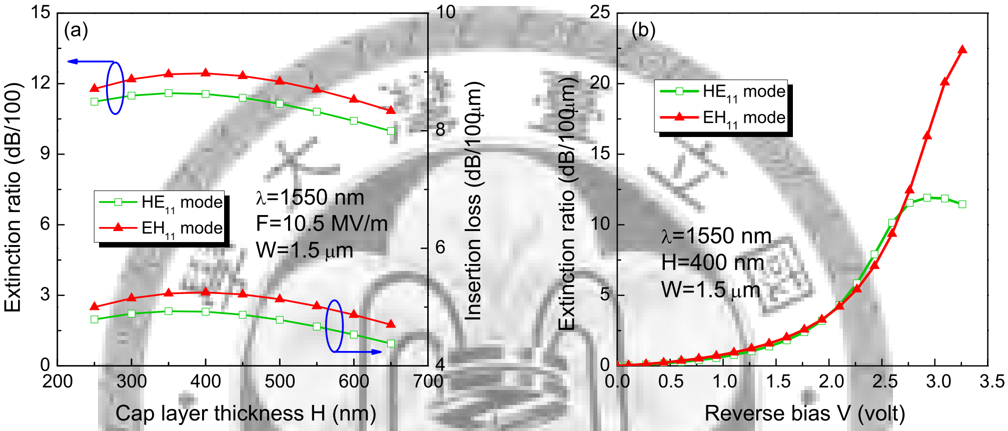

Figure 5.13: (a) Extinction ratios and insertion losses at $\lambda = 1550$ nm for the HE$_{11}$ and EH$_{11}$ modes per 100 μm waveguide length as a function of the cap layer thickness at an electric field of 10.5 MV/m, showing small differences in extinction ratio and insertion loss. (b) Extinction ratios and insertion losses at $\lambda = 1550$ nm for the HE$_{11}$ and EH$_{11}$ modes per 100 μm waveguide length as a function of reverse bias.

operation, Fig. 5.13(a) shows the extinction ratios and insertion losses per 100 μm waveguide length at $\lambda = 1550$ nm for the HE$_{11}$ and EH$_{11}$ modes as a function of the cap layer thickness at an electric field of 10.5 MV/m. From $H = 250$ nm to $H = 650$ nm, the differences in extinction ratio and insertion loss between the HE$_{11}$ and EH$_{11}$ modes are smaller than 1 dB and 0.4 dB, respectively, indicating good polarization-insensitive modulation properties. The optimal cap layer thickness is $H = 400$ nm that maximizes the extinction ratios for the HE$_{11}$ and EH$_{11}$ modes and minimizes the extinction ratio difference from $F_0 = 2.18$ MV/m to $F = 10.5$ MV/m. With the waveguide geometry determined ($W = 1.5\ \mu$m and $H = 400$ nm), Fig. 5.13(b) shows the bias-dependent extinction

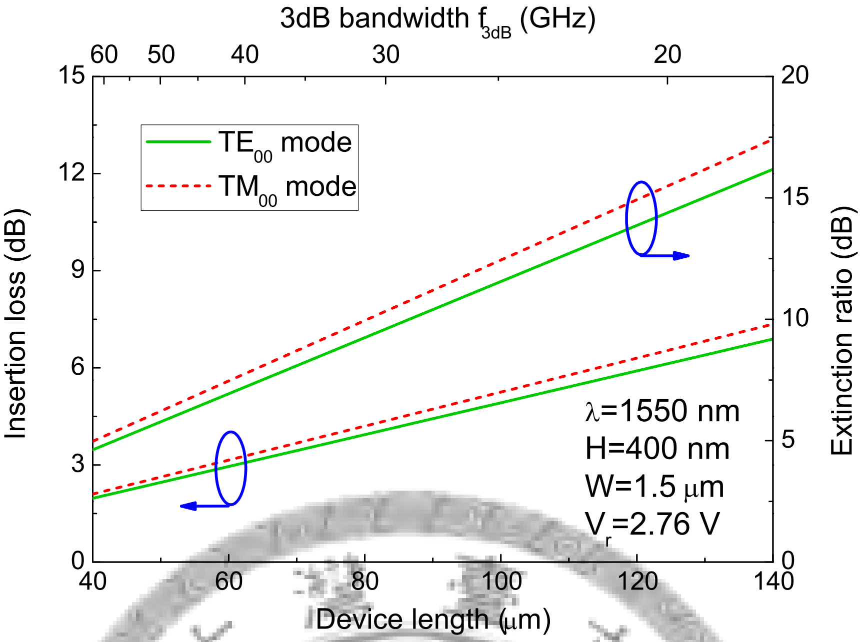

Figure 5.14: Modulation characteristics at $\lambda = 1550$ nm as a function of the device length for the MQW EA modulator, showing that high-speed and polarization-insensitive operation is possible.

ratios per 100 μm waveguide length at $\lambda = 1550$ nm for the HE$_{11}$ and EH$_{11}$ modes. The reverse bias V_r is related to the electric field F by $V_\text{r} = (F - F_0)d$, where d is the distance between the p- and n-contact regions (the total thickness of the MQW and the two spacers). The corresponding insertion losses for the HE$_{11}$ and EH$_{11}$ modes are 4.92 dB and 5.25 dB, respectively. The TE and TM extinction ratios are almost superimposed with a difference smaller than 0.85 dB up to $V_\text{r} = 2.76$ V, indicating a near polarization insensitivity at $\lambda = 1550$ nm. When the reverse bias increases further, the mutual compensation between the various effects loses its effectiveness and the TE and TM extinction ratios begin to diverge. If we fix the reverse bias at $V_\text{r} = 2.76$ V, Fig. 5.14 shows the 3-dB bandwidth, extinction ratios, and insertion losses of the MQW EA waveguide modulator as a function of the device length L. The 3-dB bandwidth for an EA modulator f_3dB is mainly limited by the RC time delay and can be calculated by $f_\text{3dB} = (2\pi RC)^{-1}$, where R is the load resistance and C is the junction capacitance. We set $R = 100\ \Omega$ and the junction capacitance is calculated using the depletion approximation [20]. Although a longer device length can enhance the extinction ratios, the insertion losses also increase and the polarization-insensitivity becomes less effective. Besides, as the device length increases, the 3-dB bandwidth also decreases drastically due to the increasing junction capacitance. To optimize the tradeoff relationship, the optimal device length should be around $L = 90\ \mu\mathrm{m}$, corresponding to a high extinction ratio of ~11 dB, a low insertion loss of ~4.5 dB, and a 3-dB bandwidth of 27.6 GHz at a driving voltage of 2.76 V. Those results indicate that the designed polarization-insensitive EA waveguide modulator using tensile-strained Ge/$\mathrm{Si}_{0.29}\mathrm{Ge}_{0.6}\mathrm{Sn}_{0.11}$ MQW has significant potentials for high-speed and low power electronic-photonic integrated circuits.

5.5 Summary

This chapter has presented a theoretical model to calculate QCSE and excitonic absorptions in a quantum well structure. Our calculation results for QCSE in Ge/SiGe QWs show excellent agreements with the experimental data, indicating our developed model is adequate for describing QCSE in a quantum-well structure. We have presented a polarization-insensitive electroabsorption waveguide modulator using tensile-strained Ge/$\mathrm{Si}_x\mathrm{Ge}_y\mathrm{Sn}_{1-x-y}$ multiple-quantum-well based on the quantum-confined Stark effect. The introduction of tensile strain into the Ge wells effectively reduces the bandgap to compensate the quantum-well confinement energy to realize optimal modulation at 1550 nm. In addition, the tensile strain brings about the near degeneracy between the lowest HH and LH states, allowing for polarization-insensitive operation in the modulator. We have also presented our waveguide design for index guidance, which shows proper optical confinements for the waveguide modes. With the optimal designs of the MQW material and waveguide geometry, a 90-$\mu\mathrm{m}$-long waveguide modulator with ten pairs of tensile-strained Ge/$\mathrm{Si}_{0.29}\mathrm{Ge}_{0.6}\mathrm{Sn}_{0.11}$ QWs remains polarization-insensitive up to 2.76 V, corresponding to a high extinction ratio of $\sim$11 dB, a small insertion loss of $\sim$4.5 dB, and a high 3-dB bandwidth of 27.6 GHz for high-speed and low-power electronic-photonic integrated circuits.

國立臺灣大學
敦品 · 勵學 · 愛國 · 愛人

Bibliography

[1] S. L. Chuang, *Physics of Photonic Devices* (Wiley, New York, 2009), 2nd ed.

[2] Y. H. Kuo, Y. K. Lee, Y. Ge, S. Ren, J. E. Roth, T. I. Kamins, D. A. B. Miller, and J. S. Harris, "Strong quantum-confined Stark effect in germanium quantum-well structures on silicon," Nature **437**, 1334–1336 (2005).

[3] O. Qasaimeh, P. Bhattacharya, and E. T. Croke, "SiGe-Si quantum-well electroabsorption modulators," IEEE Photon. Tech. Lett. **10**, 807-809 (1998).

[4] Y. Miyake, J. Y. Kim, Y. Shiraki, and S. Fukatsu, "Absence of Stark shift in strained $\mathrm{Si}_{1-x}\mathrm{Ge}_x$/Si type-I quantum wells," Appl. Phys. Lett. **68**, 2097-2099 (1996).

[5] C. Li, "Observation of quantum-confined Stark shifts in SiGe/Si type-I multiple quantum wells." J. Appl. Phys. **87**, 8195-8197 (2000).

[6] J. S. Park, R. P. G. Karunasiri, and K. L. Wang, "Observation of large Stark shift in $\mathrm{Ge}_x\mathrm{Si}_{1-x}$/Si multiple quantum wells," J. Vac. Sci. Technol. B **8**, 217-220 (1990).

[7] J. E. Roth, O. Fidaner, R. K. Schaevitz, Y.-H. Kuo, T. I. Kamins, J. S. Harris, and D. A. B. Miller, "Optical modulator on silicon employing germanium quantum wells," Opt. Express **15**, 5851–5859 (2007).

[8] S. W. Chang and S. L. Chuang, "Theory of optical gain of Ge-$\mathrm{Si}_x\mathrm{Ge}_y\mathrm{Sn}_{1-x-y}$ quantum-well lasers," IEEE J. Quantum. Electron. **43**, 249–256 (2007).

[9] D. A. B. Miller, D. S. Chemla, T. C. Damen, A. C. Gossard, W. Wiegmann, T. H. Wood, and C. A. Burrus, "Electric field dependence of optical absorption near the band gap of quantum-well structures," Phys. Rev. B **32**, 1043–1060 (1985).

[10] S. L. Chuang, S. Schmitt-Rink, D. A. B. Miller, and D. S. Chemla, "Exciton Green's-function approach to optical absorption in a quantum well with an applied electric field," Phys. Rev. B **43**, 1500–1509 (1991).

[11] T. Visser, H. Blok, B. Demeulenaere, and D. Lenstra, "Confinement factors and gain in optical amplifiers," IEEE J. Quantum Electron. **33**, 1763–1766 (1997).

[12] A. Maslov and C. Ning, “Modal gain in a semiconductor nanowire laser with anisotropic bandstructure,” IEEE J. Quantum Electron. **40**, 1389–1397 (2004).

[13] S. W. Chang and S. L. Chuang, “Fundamental formulation for plasmonic nanolasers,” IEEE J. Quantum Electron. **45**, 1014–1023 (2009).

[14] A. Stöhr, O. Humbach, S. Zumkley, G. Wingen, G. David, D. Jäger, B. Bollig, E. C. Larkins, and J. D. Ralston, “InGaAs/GaAs multiple-quantum-well modulators and switches,” Opt. Quantum Electron. **25**, S865–S883 (1993).

[15] J. Liu, D. D. Cannon, K. Wada, Y. Ishikawa, D. T. Danielson, S. Jongthammanurak, J. Michel, and L. C. Kimerling, “Deformation potential constants of biaxially tensile stressed Ge epitaxial films on Si(100),” Phys. Rev. B **70**, 155309 (2004).

[16] J. Liu, D. D. Cannon, K. Wada, Y. Ishikawa, S. Jongthammanurak, D. T. Danielson, J. Michel, and L. C. Kimerling, “Tensile strained Ge p-i-n photodetectors on Si platform for C and L band telecommunications,” Appl. Phys. Lett. **87**, 011110 (2005).

[17] Y. H. Kuo, Y. K. Lee, Y. Ge, S. Ren, J. E. Roth, T. I. Kamins, D. A. B. Miller, and J. S. Harris, Jr., “Quantum-confined Stark effect in Ge/SiGe quantum wells on Si for optical modulators,” IEEE J. Sel. Top. Quantum Electron. **12**, 1503–1513 (2006).

[18] J. Xie, J. Tolle, V. R. D’Costa, A. V. G. Chizmeshya, J. Menéndez, and J. Kouvetakis, “Direct integration of active $\mathrm{Ge}_{1-x}(\mathrm{Si}_4\mathrm{Sn})_x$ semiconductors on Si(100),” Appl. Phys. Lett. **95**, 181909 (2009).

[19] M. Bonfanti, E. Grilli, M. Guzzi, D. Chrastina, G. Isella, H. von Känel, and H. Sigg “Direct gap related optical transitions in Ge/SiGe quantum wells,” Physica E **41**(6) 972-975 (2008).

[20] B. G. Streetman, *Solid State Electronic Devices* (Prentice-Hall, New Jersey, 1995), 4th ed.

[21] E. D. Palik, ed., *Handbook of Optical Constants of Solids* (Academic, Orlando, Florida, 1985).

[22] R. E. Lindquist and A. W. Ewald, “Optical constants of single-crystal gray tin in the infrared,” Phys. Rev. **135**, A191–A194 (1964).

[23] R. Soref and J. Larenzo, “All-silicon active and passive guided-wave components for $\lambda = 1.3$ and 1.6 $\mu\mathrm{m}$,” IEEE J. Quantum. Electron. **22**, 873–879 (1986).

[24] G. E. Chang, S. W. Chang, and S. L. Chuang, "Theory for n-type doped, tensile-strained Ge-$Si_xGe_ySn_{1-x-y}$ quantum-well lasers at telecom wavelength," Opt. Express **17**, 11246–11258 (2009).

國立臺灣大學
敦品勵學 · 愛國愛人

Chapter 6

Strain-free $\mathrm{Ge}_z\mathrm{Sn}_{1-z}$/$\mathrm{Si}_x\mathrm{Ge}_y\mathrm{Sn}_{1-x-y}$ multiple-quantum-well modulators at 1550 nm wavelength

This chapter proposes and analyzes an electroabsorption waveguide modulator employing strain-free $\mathrm{Ge}_z\mathrm{Sn}_{1-z}$/$\mathrm{Si}_x\mathrm{Ge}_y\mathrm{Sn}_{1-x-y}$ quantum wells operating at 1550 nm. We suggest a combination of two approaches to achieve optimal modulation at 1550 nm: (1) alloying Ge with α-Sn reduces the direct bandgap to compensate the quantum-well confinement energy, that is, growing $\mathrm{Ge}_z\mathrm{Sn}_{1-z}$ QWs, and (2) sandwiching $\mathrm{Ge}_z\mathrm{Sn}_{1-z}$ wells by lattice-matched $\mathrm{Si}_x\mathrm{Ge}_y\mathrm{Sn}_z$ barriers can eliminate the influence of strain effects on the direct bandgap and provide an important type-I alignment. We calculate the electronic band structure and the polarization-dependent excitonic absorption coefficients. We also present the designed waveguide structure and calculate the optical confinement factors of various regions. The extinction ratio and insertion loss of the EA modulator are also estimated. The effects of the well width on the performance of the MQW waveguide modulator will be discussed.

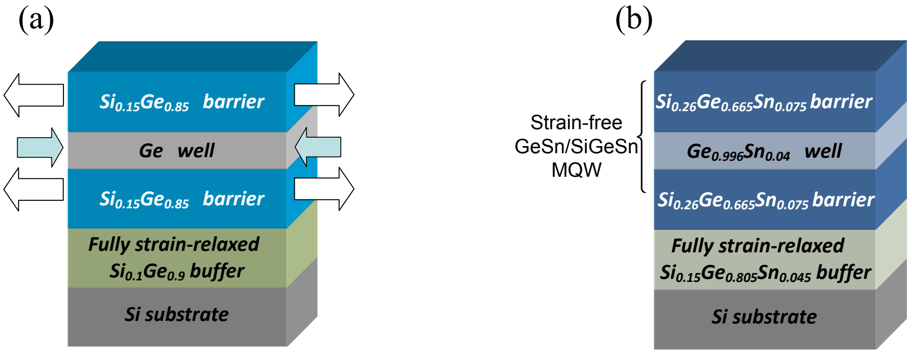

Existing design:
Strain-balanced Ge/SiGe
MQW structure

New design:
Strain-free GeSn/SiGeSn
MQW structure

Figure 6.1: Schematics of (a) the exiting design of a strain-balanced Ge/SiGe QW structure [1] and (b) our proposed strain-free GeSn/SiGeSn QW structure for electroabsorption modulators.

6.1 Strain-free Ge_zSn_{1-z}/$Si_xGe_ySn_{1-x-y}$ quantum well

Figure 6.1 schematically shows the existing design of a strain-balanced Ge/SiGe QW structure [1] and our proposed strain-free GeSn/SiGeSn QW structure for EA modulators. The existing Ge/SiGe QW structure consists a compressive-strained Ge well and tensile-strained SiGe barriers on a silicon substrate via a strain-relaxed SiGe buffer layer. However, although the direct bandgap of Ge is about 0.8 eV at room temperature, the compressive strain, together with the quantum-well confinement energy, significantly increases the direct band-edge transition energies. As a result, the Ge/SiGe QW modulator can only operate in 1440-1460 nm. On the other hand, Fig. 6.1(b) shows our proposed strain-free $Ge_{0.996}Sn_{0.004}$/$Si_{0.26}Ge_{0.665}Sn_{0.075}$ QW structure for developing electroabsorption modulators operating at 1550 nm wavelength. The inclusion of α-Sn into Ge, that is, growing Ge_zSn_{1-z} QWs, provides the opportunity to reduce the direct bandgap of Ge to compensate the quantum-well confinement energy for the realization of 1550 nm operation. Then we employ the ternary $Si_{0.26}Ge_{0.665}Sn_{0.075}$ alloy lattice-matched to the $Ge_{0.996}Sn_{0.004}$ wells as the barrier material to eliminate the influence of strain effects

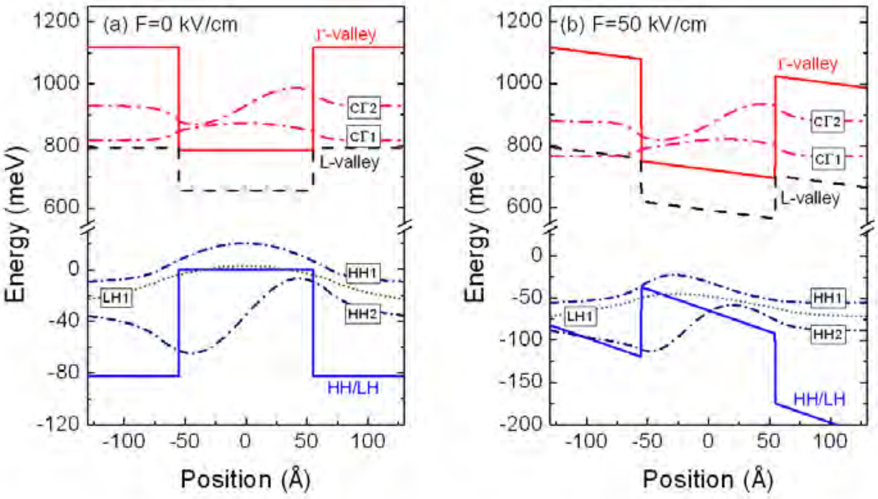

Figure 6.2: Various potential profiles and subband wavefunctions for the strain-free $Ge_{0.996}Sn_{0.004}/Si_{0.26}Ge_{0.665}Sn_{0.075}$ QW at electric fields of (a) 0 kV/cm and (b) 50 kV/cm. The magnitudes of electron wavefunctions have been scaled to 2 times for clarity.

on the direct bandgap. The recent advances in the direct growth of fully strain-relaxed SiGeSn layers on silicon substrates can provide a fully strain-relaxed, lattice-matched buffer layer for this strain-free QW to grow [2]. In this way, the entire QW can be strain-free and can provide the following advantages: (1) it helps remove the constraint of critical thickness in strained multi-layer systems, allowing the well width to be flexibly changed to adjust the transition energies, (2) it avoids the generation of strain-misfit dislocations to improve the material quality, and (3) it allows for the growth of a multiple-quantum-well (MQW) system with many periods to further enhance the performance of the modulator, since no strain energy is accumulated in the MQW region.

6.2 Optical properties of the strain-free GeSn-SiGeSn QW

Figure 6.2(a) shows the various band alignments and the confined electron and hole wavefunctions for the strain-free $Ge_{0.996}Sn_{0.004}/Si_{0.26}Ge_{0.665}Sn_{0.075}$ QW. The barrier width is 100 Å, while the well width is set to 110 Å to maintain proper electron-hole wave-

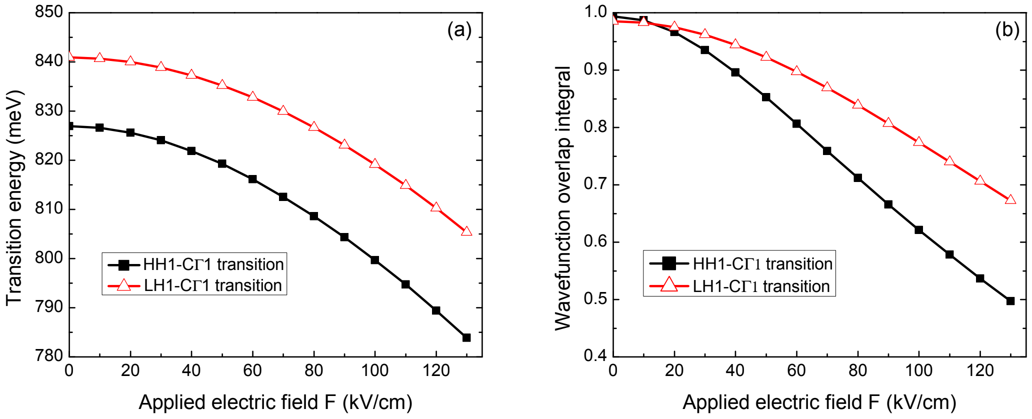

Figure 6.3: (a) Bias-dependent HH1-CΓ1 and LH1-CΓ1 transition energies. (b) Wavefunction overlap integrals of the HH1-CΓ1 and LH1-CΓ1 transitions as a function of electric field.

function overlaps for moderate excitonic absorption. Incorporating α-Sn into Ge reduces the direct bandgap of the Ge$_{0.996}$Sn$_{0.004}$ well to 787.4 meV, which is lower than that of pure Ge and can compensate for the quantum-well confinement energy. The band offsets also show that both the Γ-conduction band minimum and valence band maximum are located in the Ge$_{0.996}$Sn$_{0.004}$ well, indicating that this QW has a type-I alignment for important optical transitions in the well. There are two confined electron states in the Γ-conduction band, while two confined heavy-hole (HH) states and one light-hole (LH) state are present in the valence band. Even though the HH and LH band edges remain degenerate in the strain-free QW, the HH1 state is the topmost valence subband due to its smaller quantized energy than that of LH1 state. Therefore, the lowest excitonic transition is the CΓ1-HH1 transition. On the other hand, Fig. 6.2(b) shows the band lineups and confined states in the presence of an electric field of 50 kV/cm along the QW growth direction. The applied electric field pushes the electron and hole wavefunctions apart, indicating that the QCSE takes place.

Figure 6.3(a) shows the HH1-CΓ1 and LH1-CΓ1 transition energies as a function of electric field. In the absence of an electric field, the HH1-CΓ1 and LH1-CΓ1 transition energies are about 827 meV and 842 meV, respectively. When an electric field is applied along the QW growth direction, both the HH1-C$\Gamma 1$ and LH1-C$\Gamma 1$ transition energies decrease quadratically with the applied electric field. Nevertheless, the HH1-C$\Gamma 1$ transition energy shifts faster than the LH1-C$\Gamma 1$ transition energy due to the larger HH effective mass along the QW growth direction than the LH one. At an electric field of about 100 kV/cm, the HH1-C$\Gamma 1$ transition energy significantly shifts to about 800 meV, while the LH1-C$\Gamma 1$ transition energy can only shift to about 819 meV at the same electric field. Since the HH1-C$\Gamma 1$ transition provides dominantly transverse electric (TE) absorption in nature, this strain-free QW is expected to achieve TE-polarized modulation at $\lambda = 1550$ nm. Figure 6.3(b) shows the wavefunction overlap integrals of the HH1-C$\Gamma 1$ and LH1-C$\Gamma 1$ transitions as a function of electric field. In the absence of an electric field, both the HH1-C$\Gamma 1$ and LH1-C$\Gamma 1$ transitions have wavefunction overlap integrals of almost unity due to the sufficiently high conduction and valence band offsets provided by the $\mathrm{Si_{0.26}Ge_{0.665}Sn_{0.075}}$ barriers. As the strength of the electric field increases, both the wavefunction overlap integrals of the HH1-C$\Gamma 1$ and LH1-C$\Gamma 1$ transitions gradually diminish. However, the wavefunction overlap integral of the HH1-C$\Gamma 1$ transition falls off faster than that of the LH1-C$\Gamma 1$ transition. This is a reflection that the HH1 wavefunction becomes more asymmetric about the center of the QW than the LH1 one with the electric filed due to $m_{\mathrm{hh,z}} > m_{\mathrm{lh,z}}$.

Figure 6.4 shows the TE- and TM-polarized absorption spectra due to the direct band-edge excitonic transitions at different electric fields at room temperature. We set the FWHM linewidth $\Gamma = 14$ meV according to the analysis of the temperature-dependent FWHM in Ge/SiGe QWs [3]. In the absence of an electric field, the HH1-C$\Gamma 1$ and LH1-C$\Gamma 1$ exciton peaks are situated at about 823.2 meV and 838.8 meV, respectively. Mean-

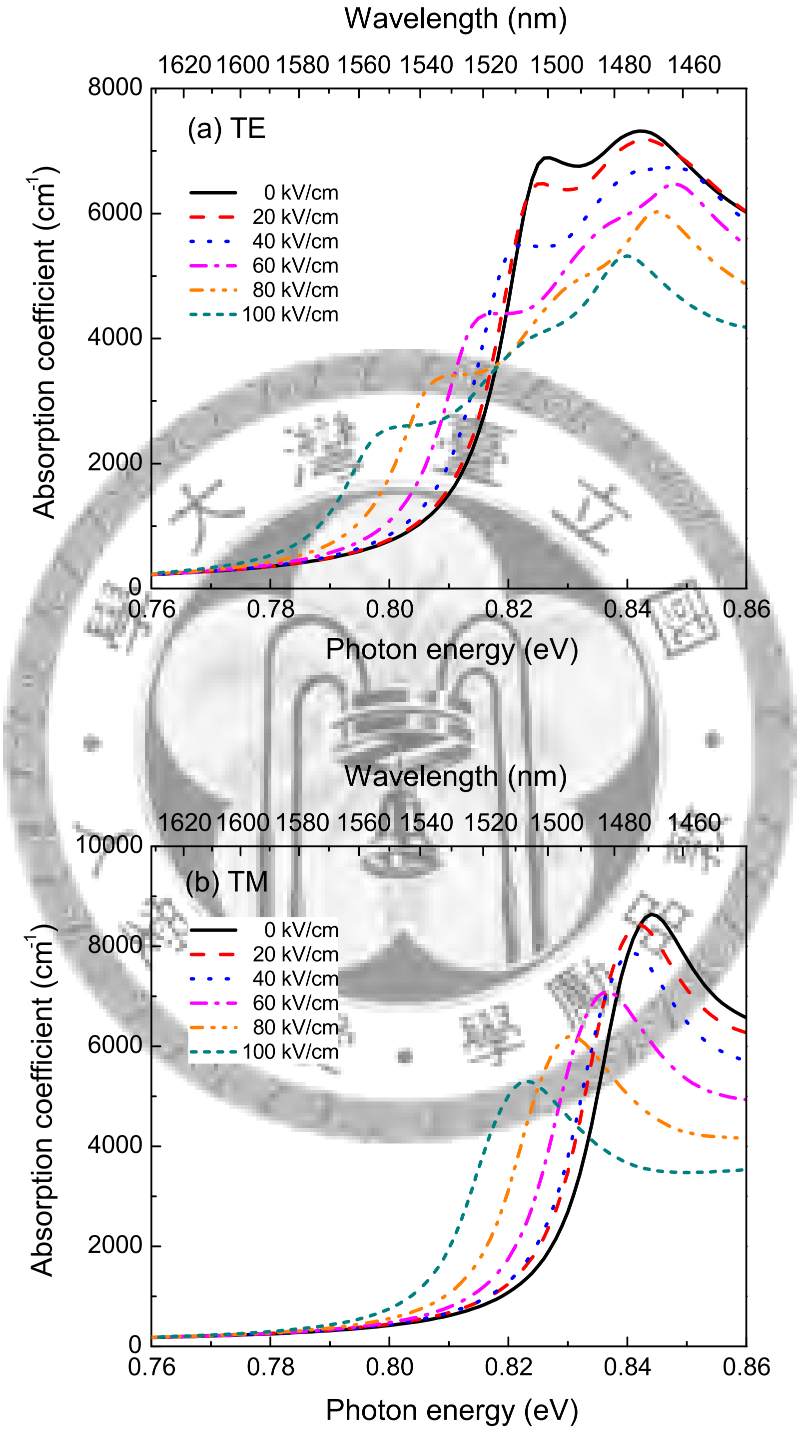

Figure 6.4: (a) TE and (b) TM absorption spectra at different applied electric fields for the strain-free $Ge_{0.996}Sn_{0.004}/Si_{0.26}Ge_{0.665}Sn_{0.075}$ QW (110 Å $Ge_{0.996}Sn_{0.004}$ well and 100 Å $Si_{0.26}Ge_{0.665}Sn_{0.075}$ barrier).

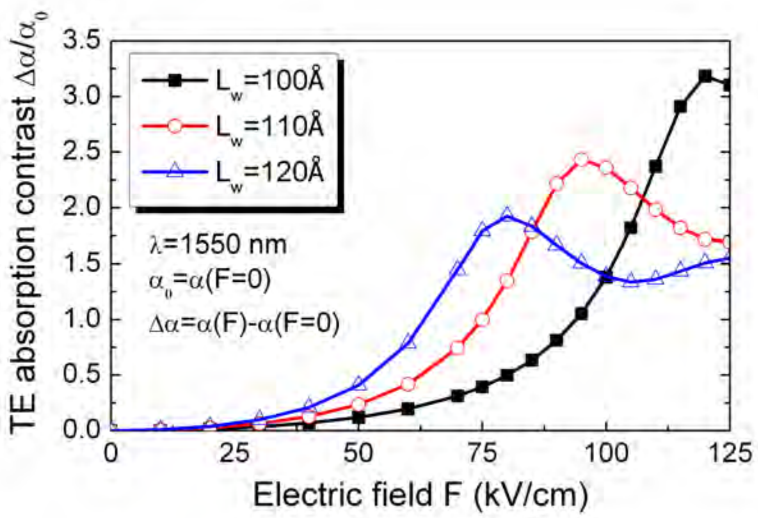

Figure 6.5: TE-polarized absorption contrast ($\Delta\alpha/\alpha_0$) at 1550 nm of the strain-free $Ge_{0.996}Sn_{0.004}/Si_{0.26}Ge_{0.665}Sn_{0.075}$ QW with different well widths as a function of electric field.

while, the TE and TM absorption coefficients at 1550 nm are as low as 762 cm^{-1} and 419 cm^{-1}, respectively, which produce a low insertion loss. As the strength of the applied electric field increases, the HH1-CΓ1 and LH1-CΓ1 exciton peaks shift toward longer wavelengths with a decreasing peak absorption strength due to the reduced electron-hole wavefunction overlaps. At an electric field of 100 kV/cm, the TE absorption coefficient at 1550 nm significantly increases to 2560.4 cm^{-1}. This large change in absorption coefficient due to QCSE implies that the strain-free QW can achieve effective modulation with a good extinction ratio and low insertion loss at 1550 nm. On the other hand, the LH1-CΓ1 exciton peak in the TM mode is more robust than the HH1-CΓ1 exciton peak in the TE mode due to its better wavefunction overlap integral and larger momentum matrix element. However, it can only shift to about 819 meV at $F = 100\ \mathrm{kV/cm}$. Thus, the wavelengths of optimal extinction ratio in the TM mode for this strain-free QW are around $\lambda = 1510\ \mathrm{nm}$.

Ideally, optical modulators should be able to achieve a high extinction ratio and low insertion loss simultaneously. An important parameter is the absorption contrast, $\Delta\alpha/\alpha_0$, where $\alpha_0 = \alpha(F = 0)$ is defined as the absorption coefficient at a zero electric field, and $\Delta\alpha = \alpha(F) - \alpha_0$ is the change in absorption coefficient caused by the QCSE. Figure 6.5 shows the TE absorption contrast at 1550 nm for the $Ge_{0.996}Sn_{0.004}/Si_{0.26}Ge_{0.665}Sn_{0.075}$ QW with different well widths, where the barrier width is kept at 100 Å. For the 110 Å-wide well, the peak absorption contrast is 2.43 at $F = 95$ kV/cm, which meets the requirements of both high extinction ratio and low insertion loss. As the well width decreases to 100 Å, the absorption contrast increases to 3.18 due to the improved electron-hole wavefunction overlap, even though a higher electric field $F = 120$ kV/cm is required. If a relatively wide well of 120 Å is used, the maximum absorption contrast occurs earlier at $F = 80$ kV/cm because the exciton peaks are more sensitive to shift with the electric field due to the wider well width. However, the maximum available absorption contrast decreases to 1.94 due to the reduced electron-hole wavefunction overlap. Based on those results, the optimal well width should be around 100$\sim$110 Å to achieve a high contrast ratio of at least 2.43 with a moderate electric field.

6.3 Waveguide design for EA modulator

Figures 6.6 shows schematics of a waveguide EA modulator employing strain-free $Ge_{0.996}Sn_{0.004}/Si_{0.26}Ge_{0.665}Sn_{0.075}$ QWs. First, a 500-nm-thick, fully strain-relaxed buffer layer of n-type $Si_{0.15}Ge_{0.805}Sn_{0.045}$ is grown on a (001)-oriented silicon substrate for the subsequent growth of the QWs. The n doping concentration is 5×10^{18} cm^{-3} to serve the buffer layer as the bottom contact. A 100-nm spacer layer of intrinsic $Si_{0.15}Ge_{0.805}Sn_{0.045}$ layer is then grown on the buffer layer. Subsequently, five pairs of $Ge_{0.996}Sn_{0.004}$ QWs with $Si_{0.26}Ge_{0.665}Sn_{0.075}$ barriers are grown on the spacer. Following the MQW, another 100-nm spacer layer of intrinsic $Si_{0.15}Ge_{0.805}Sn_{0.045}$ spacer is grown. Finally, the whole

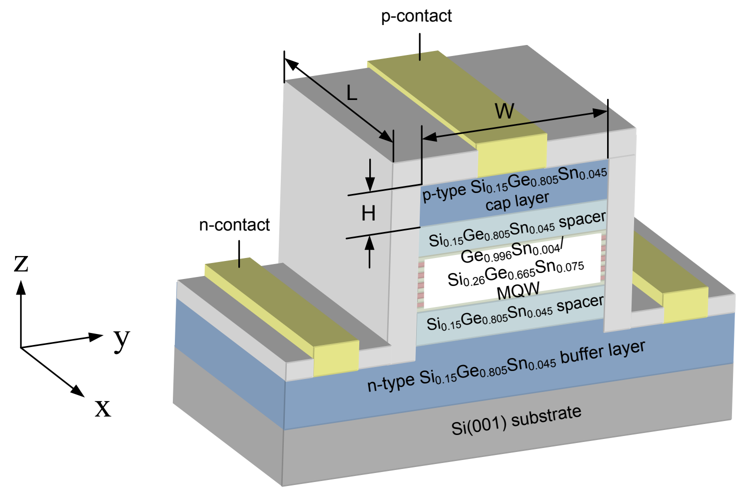

Figure 6.6: Diagram of the PIN diode mesa with 5 pairs of strain-free $Ge_{0.996}Sn_{0.004}$ QWs with $Si_{0.26}Ge_{0.665}Sn_{0.075}$ barriers for waveguide modulators.

Table 6.1: Parameters for different devices.

	Device A	Device B	Device C
Well width (Å)	100	110	120
Barrier width (Å)	100	100	100
Built-in field (kV/cm)	23.80	23.43	23.07
Optimal applied field (kV/cm)	120	95	80
Optimal operation bias voltage	2.98	2.25	1.82

structure is capped by a p-doped $Si_{0.15}Ge_{0.805}Sn_{0.045}$ layer with a p-doping concentration of $1 \times 10^{19}\mathrm{cm}^{-3}$ as the top contact. After the etching mesa is processed, then ridge structure is cover by a SiO_2 layer to form the waveguide structure. The width of the ridge structure W and the cap layer thickness H will be optimized for maximizing the absorption contrast of this modulator. For convenience, the devices with well widths of 100 Å, 110 Å, and 120 Å are denoted as devices A, B, and C, respectively, and their parameters are listed in table 6.1. The optimal electric field for optimal absorption contrasts are obtained according to Fig. 6.5.

Figure 6.7 shows the E_y field distribution of the quasi-TE fundamental mode at $\lambda = 1550\ \mathrm{nm}$ with different cap layer thickness, where the width of the ridge structure is $2\ \mu\mathrm{m}$. Clearly, the silica layer provides the upper and side cladding layers while the

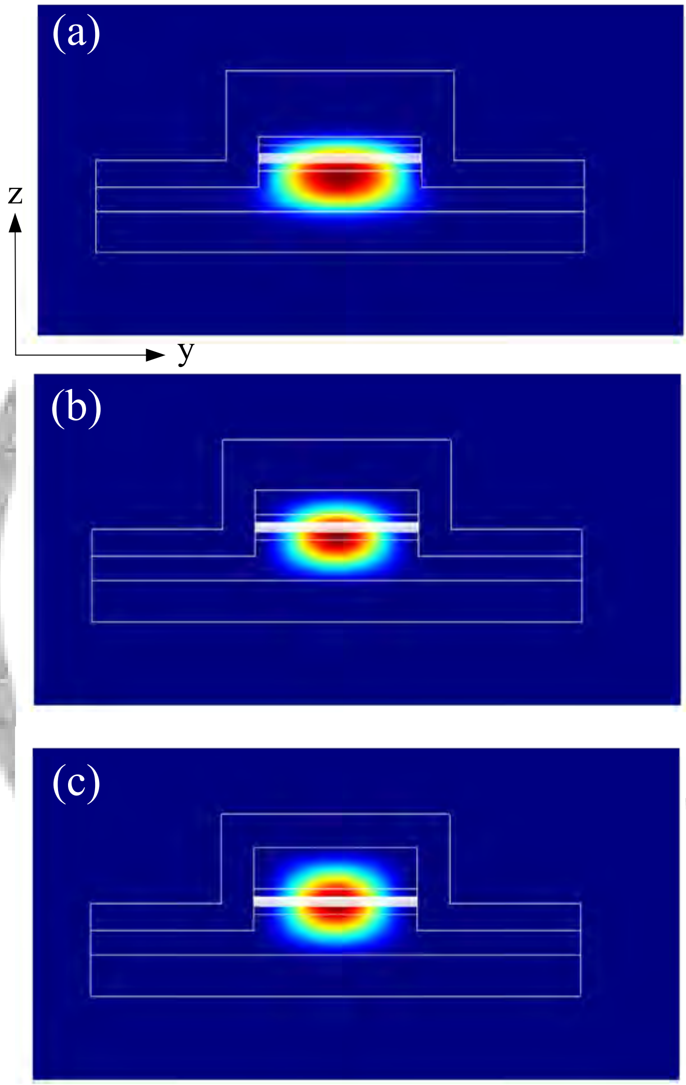

Figure 6.7: Transverse electric field (E_y) distributions of the quasi-TE fundamental mode with the p-contact layer thicknesses of (a) 100 nm, (b) 300 nm, and (c) 500nm.

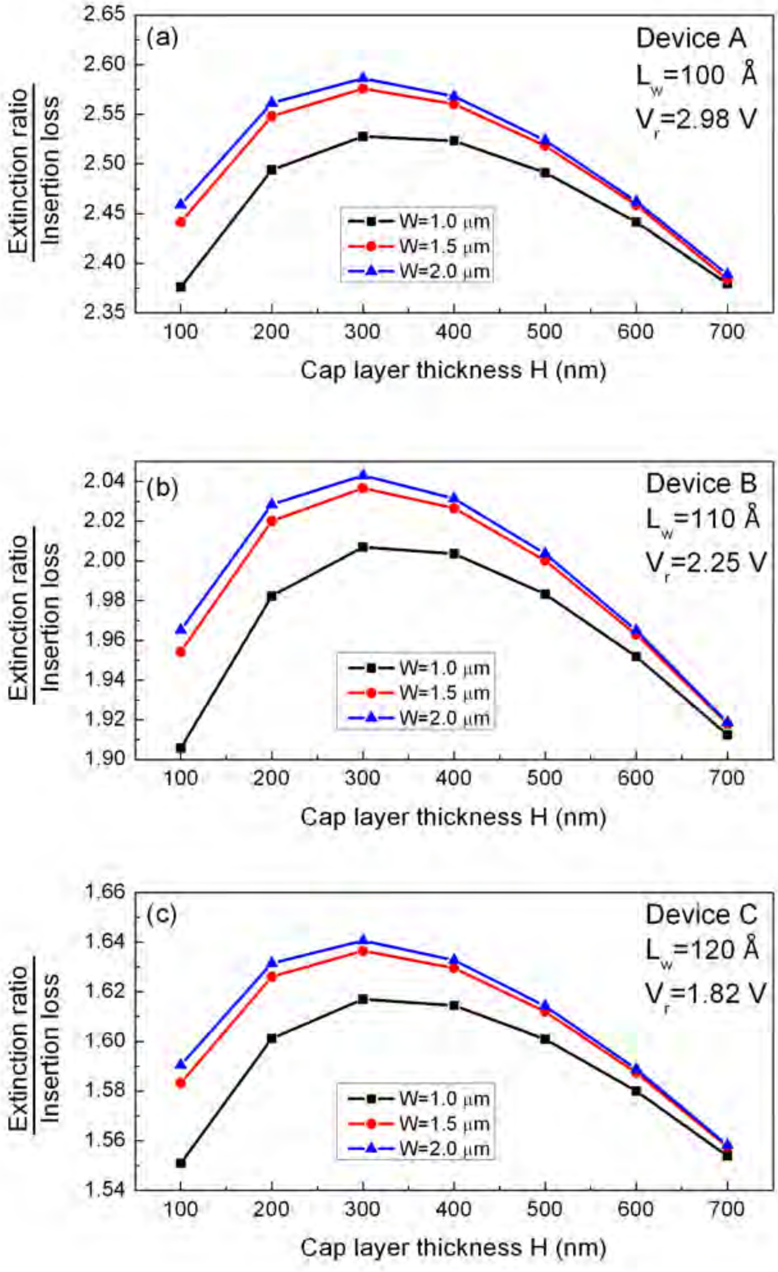

Figure 6.8: Extinction ratio over insertion loss at 1550 nm with different W and H for the strain-free $Ge_{0.996}Sn_{0.004}/Si_{0.26}Ge_{0.665}Sn_{0.075}$ QW waveguide modulator for (a) device A, (b) device B, and (c) device C .

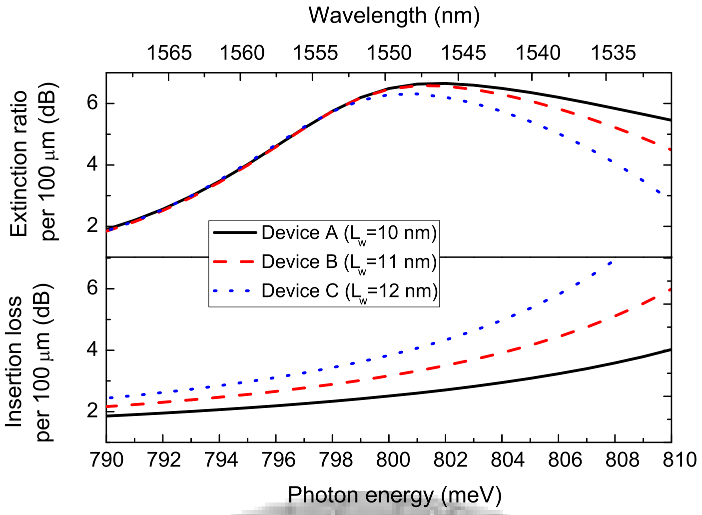

Figure 6.9: Insertion loss and extinction ratio spectra for the modulators with different well width. The waveguide width is 2 μm and the cap layer thickness is 300 nm, respectively.

silicon substrate acts as the bottom cladding layer for the guiding modes. Besides, the position of peak field changes with the thickness of the cap layer. Thus, adjusting the cap layer thickness can position the peak field around the well region to maximize the optical confinement factor for wells. Figure 6.8 shows the ratio of the extinction ratio to the insertion loss at $\lambda = 1550$ nm for devices A, B, and C, respectively, with different W and H. The optimal cap layer thickness and the optimal waveguide width are determined to be 300 nm and 2 μm for the three cases to achieve optimal extinction ratio at 1550 nm. Owing to the absorption losses due to free-carrier absorption in the n- and p-contacts, the maximum absorption contrast for devices A, B, and C are slightly reduced to 2.58, 2.04, and 1.64, respectively. This is owing to that the material absorption in the n-and p-contacts contributes to the modal absorptions.

Figure 6.9 shows the normalized insertion loss and extinction ratio spectra for devices A, B, and C in the spectral range of the telecom C-band. The extinction ratio at 1550 nm are around 6 dB per 100 μm device length for the three cases. Ideal optical modulators should have an extinction ratio more than 10 dB to effectively encoding optical signals, indicating that the device length should be larger than 200 $\mu\mathrm{m}$. Thus we set the waveguide length to 200 $\mu\mathrm{m}$. Device A has a peak extinction ratio of 13.3 dB at 1547.8 nm with an insertion loss of 5.2 dB, meeting the basic requirements of high extinction ratio and low insertion loss for optical modulators. In 1538-1552 nm, the variation of both the extinction ratio and insertion loss are smaller than 1 dB, indicating a 14-nm-wide operation range. For device B, the maximum extinction ratio is 13.16 dB at 1547.8 nm with an insertion loss of 6.64 dB. In the wavelength range of 1543-1553 nm, the variation of the extinction ratio and the insertion loss are smaller than 1 dB. For device C, the optimal extinction is 12.6 dB at 1547.8 nm with a insertion loss of 8.12 dB. Although the extinction ratio for device C is still high, the insertion loss is too large to be acceptable for real applications.

6.4 Summary

In this chapter, we have theoretically analyzed an electroabsorption waveguide modulator employing strain-free $\mathrm{Ge}_z\mathrm{Sn}_{1-z}$/$\mathrm{Si}_x\mathrm{Ge}_y\mathrm{Sn}_{1-x-y}$ QWs operating at 1550 nm. We first show our proposal of strain-free $\mathrm{Ge}_z\mathrm{Sn}_{1-z}$/$\mathrm{Si}_x\mathrm{Ge}_y\mathrm{Sn}_{1-x-y}$ QWs and then analyze its optical properties, such as the polarization-dependent excitonic absorptions and the absorption contrast, to find the required electric field which maximizes the absorption contrast. The optimal waveguide design is also present to determine the optical confinement factors of various regions. The extinction ratio and insertion loss with different well width are also compared. Those results indicates that a 200-$\mu\mathrm{m}$-long waveguide modulator employing five pairs of strain-free $\mathrm{Ge}_{0.996}\mathrm{Sn}_{0.004}$/$\mathrm{Si}_{0.26}\mathrm{Ge}_{0.665}\mathrm{Sn}_{0.075}$ QWs can achieve a high extinction ratio of 13 dB with a low insertion loss of 6.64 dB at 2.25 V reverse bias for real applications.

Bibliography

[1] Y. H. Kuo, Y. K. Lee, Y. Ge, S. Ren, J. E. Roth, T. I. Kamins, D. A. B. Miller, and J. S. Harris, "Strong quantum-confined Stark effect in germanium quantum-well structures on silicon," Nature **437**, 1334–1336 (2005).

[2] J. Xie, J. Tolle, V. R. D'Costa, A. V. G. Chizmeshya, J. Menéndez, and J. Kouvetakis, "Direct integration of active $\mathrm{Ge}_{1-x}(\mathrm{Si}_4\mathrm{Sn})_x$ semiconductors on Si(100)," Appl. Phys. Lett. **95**, 181909 (2009).

[3] M. Bonfanti, E. Grilli, M. Guzzi, D. Chrastina, G. Isella, H. von Känel, and H. Sigg, "Direct gap related optical transitions in Ge/SiGe quantum wells," Physica E **41**, 972 – 975 (2009).

國立臺灣大學

Chapter 7

Conclusions

7.1 Summary

This dissertation described an investigation of fundamental properties of SiGeSn material system, and SiGeSn-based quantum-well lasers and electroabsorption modulators. We began with the investigation of fundamental properties of Si, Ge, and α-Sn as well as their compounds, including their electronic, optical, and mechanical properties in chapter 2. Understanding those fundamental properties is very helpful to explore new possibilities of group-IV photonic and electronic devices based on the novel SiGeSn material system. In chapter 3 we proposed and develop a theoretical model for an n-type doped, tensile-strained Ge/SiGeSn quantum-well laser. With the combination of tensile strain and n-type doping in Ge QWs, population inversion is achievable to provide significant optical gain. In addition, using quantum-well structures can dramatically reduce the required n-type doping concentration and generate high material gain due to the improved density of states. Our calculations show that lasing action at 1550 nm is possible at an achievable threshold current density of $1.922\ \mathrm{kA/cm^2}$. In chapter 4, we analyzed a strain-balanced GeSn/SiGeSn multiple-quantum-well laser. Alloying Ge with α-Sn can produce a direct-bandgap GeSn alloy as a gain medium for laser light sources. The introduce of compressive strain into the GeSn active medium can effectively modify the valence band structure to reduce the threshold current density. The emission wavelength is about 2.88 $\mu\mathrm{m}$ and the threshold current density is $9.78\ \mathrm{kA/cm^2}$, comparable to $10\ \mathrm{kA/cm^2}$ of typical III-V mid-infrared MQW lasers.

In chapter 5, we proposed and analyzed a polarization-insensitive electroabsorption waveguide modulator using tensile-strained Ge/SiGeSn quantum wells for 1550 nm operation. We developed a theoretical model for MQW electroabsorption modulators and our calculated QCSE in Ge/SiGe QWs showed good agreements with the experimental data. We then presented our designed structure of a tensile-strained Ge/SiGeSn MQW electroabsorption waveguide modulator. With optimal designs of MQW material and waveguide geometry, the designed waveguide modulator can achieve 1550 nm operation and remain polarization-insensitive up to a reverse bias of 2.76 V, corresponding to a large extinction ratio of $\sim$11 dB, a low insertion loss of $\sim$4.5 dB, and a 3-dB bandwidth of 27.6 GHz. In chapter 6, we analyzed a strain-free GeSn/SiGeSn QW modulator at 1550 nm wavelength. Alloying Ge with α-Sn provides the opportunity for bandgap engineering to achieve effective modulation at 1550 nm wavelength. The strain-free GeSn/SiGeSn QWs show a high absorption contrast of at least 2.43, leading to a high extinction ratio and low insertion loss.

7.2 Future works

7.2.1 Material growth, device fabrications, device characterizations

Absolutely growing the materials is the next step. After the devices are fabricated, measurements on those devices can give more information and understand more physics for the designed devices. Additionally, the experimental input can verify and improve the developed models. Based on the experimental input and improved models, optimal designs can be carried out.

7.2.2 Photodetectors

Except for laser light sources and modulators, photodetectors are also an important component for electronic-photonic integrated circuits. Currently, Ge photodetectors have achieved a great success. By using the SiGeSn material system, further improvement for Si-based photodetectors is possible.

7.2.3 GeSn and SiGeSn quantum structures

So far only GeSn and SiGeSn quantum wells have been successfully grown on silicon substrates. If other quantum structures, such as quantum-wire and -dot systems can be grown, it will be very interesting to study the physics and design new devices based on those low-dimensional structures.

7.2.4 Quantum-cascade lasers

SiGeSn-based quantum-cascade lasers are also an interesting topic to investigate. SiGe-based quantum cascade lasers have been successfully demonstrated. By using the novel SiGeSn material system, SiGeSn-based quantum cascade lasers may have better performance than the conventional SiGe counterparts. However, it may require lots of effort to grow so many SiGeSn quantum wells.

Although there are still many problems we need to solve before bring our designs to real applications, the fundamental properties and physics of the designed devices are sound. The SiGeSn material system is very promising to realize various high-performance Si-based electronic and photonic devices for electronic-photonic integrated circuits.

Appendix A

Derivation of Hamiltonian for [111] L-valley conduction band

In indirect bandgap semiconductors, the lowest conduction band edge is not at Γ point in k-space, but others such as L point or X (or Δ) point. Figure A1 shows energy surface for Γ-, X-(Δ-), and L-conduction valleys in semiconductors. Unlike the Γ-conduction valley whose energy surface is isotropic, as shown in Fig. A1(a), the L and X(Δ) conduction valleys have anisotropic energy surfaces. For Si, the lowest conduction band edge is at Δ point and there are six (Δ) minima along $\langle 100 \rangle$ direction, as shown in Fig. A1(b). For Ge, the lowest conduction band is at L point. In addition, there are eight equivalent L-conduction valleys in group IV semiconductors, but only four of them are independent due to the periodicity of the Brillouin zone, as shown in Fig. A1(c). For the case of quantum wells grown along the [001] direction, the four L-conduction valleys are degenerate. Thus, one only needs to calculate a particular L-conduction valley, say [111] L-conduction valley. To derive the Hamiltonian for the [111] L-conduction valley, we consider the ellipsoid energy surface of the [111] L-conduction valley with respect to the coordinate systems (k_x, k_y, k_z) and (k'_x, k'_y, k'_z), as shown in Fig. A2. The center of ellipsoid energy surface of the [111] L-conduction valley is located at $\left(\frac{\pi}{a}, \frac{\pi}{a}, \frac{\pi}{a}\right)$. The

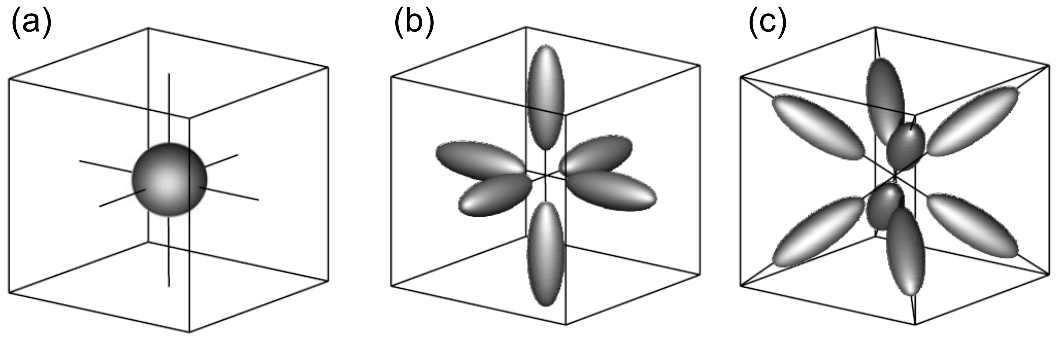

Figure A.1: Ellipsoids of constant energy in the vicinity of the conduction-band minima for (a) GaAs-like valley with its isotropic minimum at Γ-point, (b) Si-like valleys with their minimum at Δ point, and (c) Ge-like valleys with the minimum at L point [1].

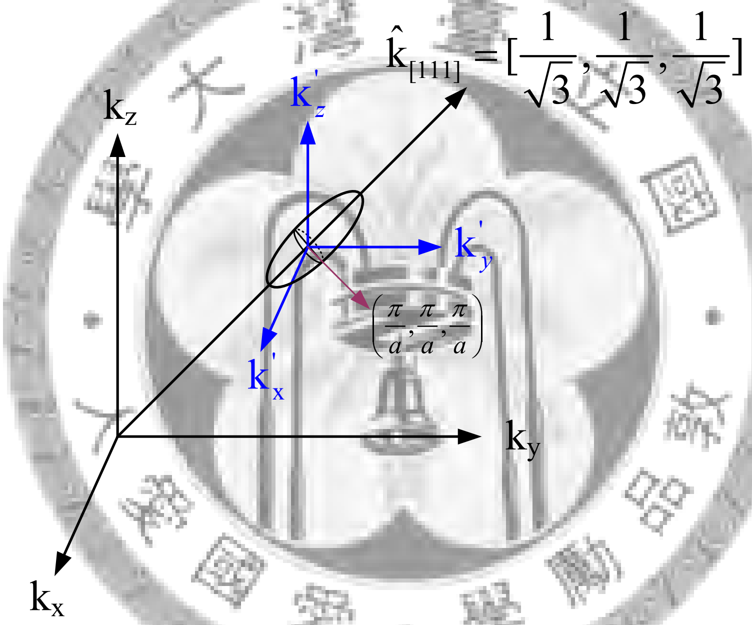

Figure A.2: Constant energy ellipsoid of the [111] L-conduction valley referring to the $\{k_x, k_y, k_z\}$ and $\{k'_x, k'_y, k'_z\}$ coordinate systems.

relationship between the two coordinate systems is

$$\begin{cases} k'_x = k_x - \frac{\pi}{a} \\ k'_y = k_y - \frac{\pi}{a} \\ k'_z = k_z - \frac{\pi}{a} \end{cases} \tag{A.1}$$

For any vector $\mathbf{k} = k_{\mathrm{u}}\hat{\mathbf{k}}'_x + k_{\mathrm{v}}\hat{\mathbf{k}}'_y + k_{\mathrm{w}}\hat{\mathbf{k}}'_z$ originated form $\left(\frac{\pi}{a}, \frac{\pi}{a}, \frac{\pi}{a}\right)$, one can decompose it into two vectors along the longitudinal and transverse directions, that is, $\mathbf{k} = \mathbf{k}_{\mathrm{a}} + \mathbf{k}_{\mathrm{b}}$,

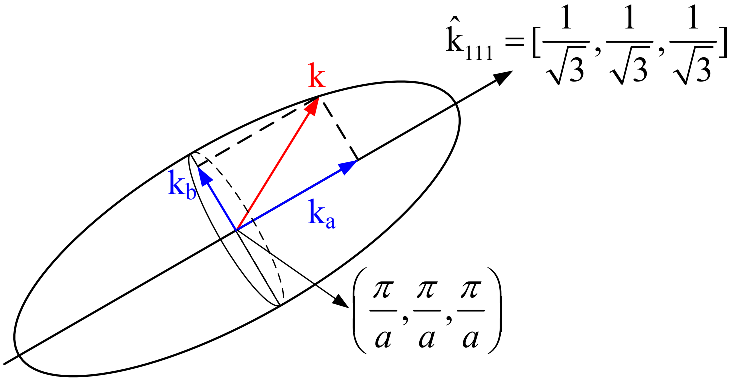

Figure A.3: Ellipsoid energy surface of the [111] L-conduction valley and the wavevector.

where

$$
\begin{aligned}
\mathbf{k}_{\mathrm{a}} &= \left(\mathbf{k} \cdot \hat{\mathbf{k}}_{[111]}\right) \hat{\mathbf{k}}_{[111]} \\
&= \left\{ [k_{\mathrm{u}}, k_{\mathrm{v}}, k_{\mathrm{w}}] \cdot \left[\frac{1}{\sqrt{3}}, \frac{1}{\sqrt{3}}, \frac{1}{\sqrt{3}}\right] \right\} \left[\frac{1}{\sqrt{3}}, \frac{1}{\sqrt{3}}, \frac{1}{\sqrt{3}}\right] \\
&= \left[\frac{k_{\mathrm{u}} + k_{\mathrm{v}} + k_{\mathrm{w}}}{3}, \frac{k_{\mathrm{u}} + k_{\mathrm{v}} + k_{\mathrm{w}}}{3}, \frac{k_{\mathrm{u}} + k_{\mathrm{v}} + k_{\mathrm{w}}}{3}\right], \qquad \text{(A.2)}
\end{aligned}
$$

$$
\begin{aligned}
\mathbf{k}_{\mathrm{b}} &= \mathbf{k} - \mathbf{k}_{\mathrm{a}} \\
&= [k_{\mathrm{u}}, k_{\mathrm{v}}, k_{\mathrm{w}}] - \left[\frac{k_{\mathrm{u}} + k_{\mathrm{v}} + k_{\mathrm{w}}}{3}, \frac{k_{\mathrm{u}} + k_{\mathrm{v}} + k_{\mathrm{w}}}{3}, \frac{k_{\mathrm{u}} + k_{\mathrm{v}} + k_{\mathrm{w}}}{3}\right]. \qquad \text{(A.3)}
\end{aligned}
$$

Therefore, the energy of an electron in the [111] L-conduction band with a wavevector of $\mathbf{k}$ under the effective-mass approximation can be represented by

$$
\begin{aligned}
E_{\mathrm{L},[111]}(\mathbf{k}) &= \frac{\hbar^2}{2m_{\mathrm{l,L}}} \mathbf{k}_{\mathrm{a}}^2 + \frac{\hbar^2}{2m_{\mathrm{t,L}}} \mathbf{k}_{\mathrm{b}}^2 \\
&= \frac{\hbar^2}{2m_{\mathrm{l,L}}} \left[\frac{k_{\mathrm{u}} + k_{\mathrm{v}} + k_{\mathrm{w}}}{3}, \frac{k_{\mathrm{u}} + k_{\mathrm{v}} + k_{\mathrm{w}}}{3}, \frac{k_{\mathrm{u}} + k_{\mathrm{v}} + k_{\mathrm{w}}}{3}\right]^2 \\
&\quad + \frac{\hbar^2}{2m_{\mathrm{t,L}}} \left\{ [k_{\mathrm{u}}, k_{\mathrm{v}}, k_{\mathrm{w}}] - \left[\frac{k_{\mathrm{u}} + k_{\mathrm{v}} + k_{\mathrm{w}}}{3}, \frac{k_{\mathrm{u}} + k_{\mathrm{v}} + k_{\mathrm{w}}}{3}, \frac{k_{\mathrm{u}} + k_{\mathrm{v}} + k_{\mathrm{w}}}{3}\right] \right\}^2 \\
&= \frac{\hbar^2}{6} \left(\frac{1}{m_{\mathrm{l,L}}} - \frac{1}{m_{\mathrm{t,L}}}\right) (k_{\mathrm{u}} + k_{\mathrm{v}} + k_{\mathrm{w}})^2 + \frac{\hbar^2}{2m_{\mathrm{t,L}}} \left(k_{\mathrm{u}}^2 + k_{\mathrm{v}}^2 + k_{\mathrm{w}}^2\right), \qquad \text{(A.4)}
\end{aligned}
$$

where $m_{\mathrm{l,L}}$ and $m_{\mathrm{t,L}}$ are electron effective masses along the longitudinal direction and the transverse direction, respectively. To simplify the expression, we define two wavevectors

$$\mathbf{k}_1 = k_1[100] = \frac{1}{\sqrt{2}}\left(k_x + k_y - \frac{2\pi}{a}\right)[100], \tag{A.5}$$

$$\mathbf{k}_2 = k_2[\bar{1}10] = \frac{1}{\sqrt{2}}\left(-k_x + k_y\right)[\bar{1}10], \tag{A.6}$$

where k_1 and k_2 are the magnitudes of the wavevectors along the $[100]$ and $[\bar{1}10]$ directions, respectively. Obviously, $\mathbf{k}_1$ and $\mathbf{k}_2$ are orthogonal to each other. By substituting Eq. (A1) into Eq. (A5), one can obtain

$$k_{\mathrm{u}} = \frac{1}{\sqrt{2}}\left(k_1 - k_2\right), \tag{A.7}$$

$$k_{\mathrm{v}} = \frac{1}{\sqrt{2}}\left(k_1 + k_2\right), \tag{A.8}$$

Then substituting Eqs. (A.7) and (A.8) into Eq. (A.4) gives the dispersion relation of the ellipsoid energy surface in terms of k_1, k_2, and k_{w}

$$\begin{aligned} E_{\mathrm{L},[111]}(k_1, k_2, k_{\mathrm{w}}) &= \frac{\hbar^2}{6}\left(\frac{1}{m_{\mathrm{l,L}}} - \frac{1}{m_{\mathrm{t,L}}}\right)\left(\sqrt{2}k_1 + k_{\mathrm{w}}\right)^2 + \frac{\hbar^2}{2m_{\mathrm{t,L}}}\left(k_1^2 + k_2^2 + k_{\mathrm{w}}^2\right) \\ &= k_{\mathrm{w}}^2\left(\frac{1}{3m_{\mathrm{l,L}}} + \frac{2}{3m_{\mathrm{t,L}}}\right) + \frac{\sqrt{2}}{3}k_1\left[\left(\frac{1}{m_{\mathrm{l,L}}} - \frac{1}{m_{\mathrm{t,L}}}\right)\right]k_{\mathrm{w}} \\ &\quad + \left(\frac{1}{3m_{\mathrm{l,L}}} + \frac{2}{3m_{t,L}}\right)k_1^2 + \frac{k_2^2}{2m_{\mathrm{t,L}}}, \end{aligned} \tag{A.9}$$

If the quantum well is grown along the z direction, the Hamiltonian of the [111] L-conduction band can be obtained by replacing k_w by the operator $-i\frac{\partial}{\partial z}$

$$
\begin{aligned}
&H_{\mathrm{L},[111]}\left(k_1, k_2, k_\mathrm{w} = -i\frac{\partial}{\partial z}\right) \\
&= -\frac{\hbar^2}{2}\frac{\partial^2}{\partial z^2}\left(\frac{1}{3m_{\mathrm{l,L}}} + \frac{2}{3m_{\mathrm{t,L}}}\right) \\
&\quad - i\frac{\sqrt{2}\hbar^2}{6}k_1\left[\frac{\partial}{\partial z}\left(\frac{1}{m_{\mathrm{l,L}}} - \frac{1}{m_{\mathrm{t,L}}}\right) + \left(\frac{1}{m_{\mathrm{l,L}}} - \frac{1}{m_{\mathrm{t,L}}}\right)\frac{\partial}{\partial z}\right] \\
&\quad + \left(\frac{2}{3m_{\mathrm{l,L}}} + \frac{1}{3m_{\mathrm{t,L}}}\right)\frac{\hbar^2 k_1^2}{2} + \frac{\hbar^2 k_2^2}{2m_{\mathrm{t,L}}},
\end{aligned}
\tag{A.10}
$$

which is the Hamiltonian of the [111] L-conduction valley relative to the minimal point of the [111] L-valley $\left(\frac{\pi}{a}, \frac{\pi}{a}\right)$.

Bibliography

[1] M. Grundmann, *The Physics of Semiconductors: An Introduction Including Devices and Nanophysics* (Berlin Heidelberg: Springer, 2006).

Appendix B

Derivation of strain-balanced condition

With the rapid development of semiconductor epitaxial technology, strained epitaxial multiple-layer systems are of particular interest for electronic and photonic devices. Strain effects in semiconductors can effectively modify band structures, bandgaps, carrier effective masses of semiconductors, such as multiple-quantum-well (MQW) and superlattice (SL) systems, providing a number of advantages over conventional strain-free systems. For example, strained II-V quantum-well (QT) lasers have been shown to have a lower threshold current density than that of conventional strain-free QT lasers [1], and strained Si on SiGe layer have been applied for high-speed complimentary metal-oxide semiconductor devices [2], [3]. However, introducing strain into semiconductors may produce strain-misfit dislocations if the accommodated elastic strain energy in the system is larger than the energy of dislocation formation. Therefore, to ensure pseudomorphic growths of multiple layers, a careful engineering of composition and thickness for each layer as well as those of (virtual) substrates is necessary to reduce the unwanted strain-misfit dislocations and other defects [4].

The principle of strain-balanced structures is proposed for reducing strain misfit dislocations in strained epitaxial layers. By growing alternating compressive-strained and tensile-strained layers with careful choices of the amount of strain and thickness for each

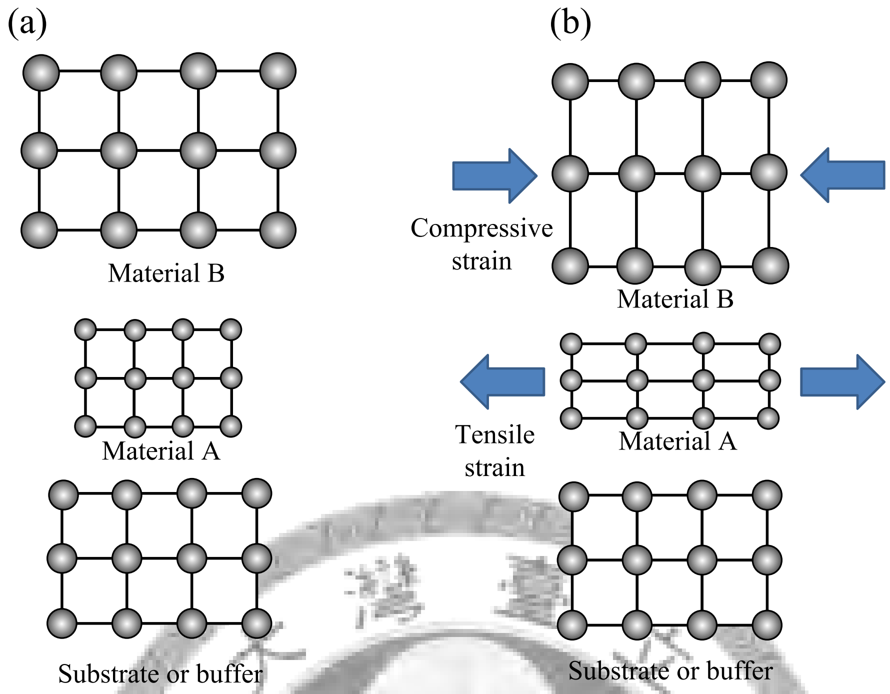

Figure B.1: Schematics of growing lattice-mismatched materials on a substrate. (a) The material A has a lattice constant smaller than that of substrate ($a_{\mathrm{A}} < a_0$) while the material B has a lattice constant larger than that of the substrate ($a_{\mathrm{B}} > a_0$). (b) After the material A and B are pseudomorphically grown on the substrate, the in-plane lattice constants of the epitaxial layers will be forced to equal to that of the substrate. Thus, the material A are tensile-strained and the material B are compressive-strained. In this way, the alternatively growth of tensile-strain layers and compressive-strained layers is called strain-balancing technique.

layer, as shown in Fig B.1, strain-misfit dislocations in strained multiple-layer systems can be reduced. However, common methods to design the strained multiple layer system are average lattice method [4] and thickness weight method [5], [6]. Although they are relatively easy and simple to use, they cannot account for the material properties. Here we use the elasticity theory to develop the strain-balanced condition based on the minimization of total strain energy [7], [8] for designing strained multiple-layer systems. Two material systems will be considered in the derivation of strain-balanced condition, (001)-oriented cubic material system and (0001)-oriented wurtzite material system.

B.1 (001)-oriented cubic system

First, we consider a cubic-based multiple-layer system. If there are N layers pseudomorphically grown on a (001)-oriented (virtual) substrate, the strain field in the ith layer caused by the lattice-mismatch is

$$\varepsilon^i_{xx} = \varepsilon^i_{yy} = \varepsilon^i = \frac{a_0 - a_i}{a_i}, \tag{B.1}$$

$$\varepsilon^i_{zz} = -2\frac{C^{(i)}_{12}}{C^{(i)}_{11}}\varepsilon^i, \tag{B.2}$$

$$\varepsilon^i_{xy} = \varepsilon^i_{yx} = \varepsilon^i_{zx} = \varepsilon^i_{xz} = \varepsilon^i_{yz} = \varepsilon^i_{zy} = 0, \tag{B.3}$$

where a_0 and a_i are the unstrained lattice constants of the substrate and the ith layer, respectively, and $C^{(i)}_{11}$, $C^{(i)}_{12}$, and $C^{(i)}_{44}$ are the stiffness matrix elements of the ith layer. Note that there is no shear strain for a (001)-oriented strained layered system. The corresponding strain energy density in the ith layer is

$$\begin{aligned}
v^i_{\text{cubic}} &= \frac{1}{2}\boldsymbol{\varepsilon}^{\mathrm{T}}\mathbf{C}\boldsymbol{\varepsilon} \\
&= \frac{1}{2}\begin{bmatrix} \varepsilon^i_{xx} \\ \varepsilon^i_{yy} \\ \varepsilon^i_{zz} \\ \varepsilon^i_{yz} + \varepsilon^i_{zy} \\ \varepsilon^i_{zx} + \varepsilon^i_{xz} \\ \varepsilon^i_{xy} + \varepsilon^i_{yx} \end{bmatrix}^{\mathrm{T}}
\begin{bmatrix} C^{(i)}_{11} & C^{(i)}_{12} & C^{(i)}_{12} & 0 & 0 & 0 \\ C^{(i)}_{12} & C^{(i)}_{11} & C^{(i)}_{12} & 0 & 0 & 0 \\ C^{(i)}_{12} & C^{(i)}_{12} & C^{(i)}_{11} & 0 & 0 & 0 \\ 0 & 0 & 0 & C^{(i)}_{44} & 0 & 0 \\ 0 & 0 & 0 & 0 & C^{(i)}_{44} & 0 \\ 0 & 0 & 0 & 0 & 0 & C^{(i)}_{44} \end{bmatrix}
\begin{bmatrix} \varepsilon^i_{xx} \\ \varepsilon^i_{yy} \\ \varepsilon^i_{zz} \\ \varepsilon^i_{yz} + \varepsilon^i_{zy} \\ \varepsilon^i_{zx} + \varepsilon^i_{xz} \\ \varepsilon^i_{xy} + \varepsilon^i_{yx} \end{bmatrix} \\
&= \left(C^{(i)}_{11} + C^{(i)}_{12} - 2\frac{C^{(i)2}_{12}}{C^{(i)}_{11}} \right)(\varepsilon^i)^2,
\end{aligned} \tag{B.4}$$

Thus, the total strain energy stored in the system is

$$\begin{aligned} W_{\text{cubic}} &= \int_V v_{\text{cubic}} \mathrm{d}V \\ &= \sum_i v^i_{\text{cubic}} L_i A \\ &= \sum_i \left(C^{(i)}_{11} + C^{(i)}_{12} - 2\frac{C^{(i)2}_{12}}{C^{(i)}_{11}} \right) (\varepsilon^i)^2 L_i A, \end{aligned} \tag{B.5}$$

where A is the area of the epitaxial layer, and L_i is the thickness of the ith layer. According to the principle of minimum potential energy, which states that the potential energy has a local minimum in the equilibrium configuration if all displacements satisfying the given boundary conditions of an elastic solid, the strain energy of the considered system has a local minimum since the considered system is at equilibrium [9, 10, 11]. Therefore, the variation of the strain energy vanishes

$$\delta W_{\text{cubic}} = 2 \sum_i \left(C^{(i)}_{11} + C^{(i)}_{12} - 2\frac{C^{(i)2}_{12}}{C^{(i)}_{11}} \right) \varepsilon^i \delta\varepsilon^i L_i A = 0. \tag{B.6}$$

However, the variation of strain for each layer is interdependent by

$$(1 + \varepsilon^1) a_1 = (1 + \varepsilon^2) a_2 = \ldots = (1 + \varepsilon^i) a_i. \tag{B.7}$$

Thus, substituting Eq. (B7) into Eq. (B6) gives

$$\begin{aligned} \delta W_{\text{cubic}} = 2 &\left(C^{(1)}_{11} + C^{(1)}_{12} - 2\frac{C^{(1)2}_{12}}{C^{(1)}_{11}} \right) \varepsilon^1 \delta\varepsilon^1 L_1 A \\ &+ 2 \sum_{i=2}^{N} \left(C^{(i)}_{11} + C^{(i)}_{12} - 2\frac{C^{(i)2}_{12}}{C^{(i)}_{11}} \right) \varepsilon^i \frac{a_1 \delta\varepsilon^1}{a_i} L_i A \\ = 0. \end{aligned} \tag{B.8}$$

Dividing a_1 on the both sides of Eq. (B8) yields

$$2A\left[\sum_{i=1}^{N}\left(C_{11}^{(i)}+C_{12}^{(i)}-2\frac{C_{12}^{(i)2}}{C_{11}^{(i)}}\right)\frac{L_i\varepsilon^i}{a_i}\right]\delta\varepsilon^i=0. \tag{B.9}$$

Since $\delta\varepsilon^i$ is arbitrary and A is a constant, we obtain the strain-balanced condition which minimizes the total strain energy of the system

$$\sum_{i=1}^{N}\left(C_{11}^{(i)}+C_{12}^{(i)}-2\frac{C_{12}^{(i)2}}{C_{11}^{(i)}}\right)\frac{L_i\varepsilon^i}{a_i}=0. \tag{B.10}$$

Several important points for the strain-balanced condition should be pointed out: (1) the strain-balanced condition relies on not only the amount of strain and the thickness for each epitaxial layer, but also the stiffness matrix elements of materials. Thus, the strain-balanced condition based on the minimization of total strain energy is more adequate for designing strained multiple-layer system because it can account for the material properties, which are not considered in the average lattice method or thickness weighted method [4]. (2) Since the lattice constants, the layer thicknesses, and the constant $\left(C_{11}^{(i)}+C_{12}^{(i)}-2\frac{C_{12}^{(i)2}}{C_{11}^{(i)}}\right)$ are all greater than zero, the strain-balanced condition only holds when strains in different layers have different signs, that is, some layers are compressive-strained and the others are tensile-strained. Thus, by engineering the thickness and strain of each layer, the strain balanced condition can be achieved to minimize the total strain energy in the system. Besides, if the material and thickness of each epitaxial layer are predetermined, one can also engineer the lattice constant of the (virtual) substrate to achieve the strain balancing condition. By substituting Eq.(B1) into Eq.(B10), after some algebra manipulations one can obtain the required lattice constant of the (virtual) substrate as

$$a_0 = \frac{\sum_{i=1}^{N}\left(C_{11}^{(i)} + C_{12}^{(i)} - 2\frac{C_{12}^{(i)2}}{C_{11}^{(i)}}\right) L_i/a_i}{\sum_{i=1}^{N}\left(C_{11}^{(i)} + C_{12}^{(i)} - 2\frac{C_{12}^{(i)2}}{C_{11}^{(i)}}\right) Li/a_i^2}, \tag{B.11}$$

which is identical with the result in Ref. [8]

B.2 (0001)-oriented wurtzite material system

Similarly, for a wurtzite-based multiple-layer system pseudomorphically grown on a (0001)-oriented (virtual) substrate with the lattice constants of the *i*th layer and the (virtual) substrate being a_i and a_0, respectively, the strain field due to the lattice mismatch in the ith layer is

$$\varepsilon_{xx}^{i} = \varepsilon_{yy}^{i} = \varepsilon^{i} = \frac{a_0 - a_i}{a_i}, \tag{B.12}$$

$$\varepsilon_{zz}^{i} = -2\frac{C_{13}^{(i)}}{C_{11}^{(i)}}\varepsilon^{i}, \tag{B.13}$$

$$\varepsilon_{xy}^{i} = \varepsilon_{yx}^{i} = \varepsilon_{zx}^{i} = \varepsilon_{xz}^{i} = \varepsilon_{yz}^{i} = \varepsilon_{zy}^{i} = 0. \tag{B.14}$$

The strain energy density in the *i*th layer is

$$
\begin{aligned}
v_{\mathrm{hex}}^{i} &= \frac{1}{2}\boldsymbol{\varepsilon}^{\mathrm{T}}\mathbf{C}\boldsymbol{\varepsilon} \\
&= \frac{1}{2}\begin{bmatrix} \varepsilon_{xx}^{i} \\ \varepsilon_{yy}^{i} \\ \varepsilon_{zz}^{i} \\ \varepsilon_{yz}^{i}+\varepsilon_{zy}^{i} \\ \varepsilon_{zx}^{i}+\varepsilon_{xz}^{i} \\ \varepsilon_{xy}^{i}+\varepsilon_{yx}^{i} \end{bmatrix}^{\mathrm{T}}
\begin{bmatrix} C_{11}^{(i)} & C_{12}^{(i)} & C_{13}^{(i)} & 0 & 0 & 0 \\ C_{12}^{(i)} & C_{11}^{(i)} & C_{13}^{(i)} & 0 & 0 & 0 \\ C_{13}^{(i)} & C_{13}^{(i)} & C_{33}^{(i)} & 0 & 0 & 0 \\ 0 & 0 & 0 & C_{44}^{(i)} & 0 & 0 \\ 0 & 0 & 0 & 0 & C_{44}^{(i)} & 0 \\ 0 & 0 & 0 & 0 & 0 & \frac{1}{2}\left(C_{11}^{(i)}-C_{12}^{(i)}\right) \end{bmatrix}
\begin{bmatrix} \varepsilon_{xx}^{i} \\ \varepsilon_{yy}^{i} \\ \varepsilon_{zz}^{i} \\ \varepsilon_{yz}^{i}+\varepsilon_{zy}^{i} \\ \varepsilon_{zx}^{i}+\varepsilon_{xz}^{i} \\ \varepsilon_{xy}^{i}+\varepsilon_{yx}^{i} \end{bmatrix} \\
&= \left(C_{11}^{(i)}+C_{12}^{(i)}-2\frac{C_{13}^{(i)2}}{C_{11}^{(i)}}\right)(\varepsilon^{i})^{2}. \qquad \text{(B.15)}
\end{aligned}
$$

Thus, the total strain energy stored in the system is

$$
\begin{aligned}
W_{\mathrm{hex}} &= \int_{V} v_{\mathrm{hex}}\mathrm{d}V \\
&= \sum_{i} v_{\mathrm{hex}}^{i} L_{i} A \\
&= \sum_{i}\left(C_{11}^{(i)}+C_{13}^{(i)}-2\frac{C_{12}^{(i)2}}{C_{11}^{(i)}}\right)(\varepsilon^{i})^{2} L_{i} A. \qquad \text{(B.16)}
\end{aligned}
$$

Similarly, the strain energy stored in this system also has a local minimum because the system is at equilibrium. Thus the variation of the total strain energy vanishes

$$
\delta W_{\mathrm{hex}} = 2\sum_{i}\left(C_{11}^{(i)}+C_{13}^{(i)}-2\frac{C_{13}^{(i)2}}{C_{11}^{(i)}}\right)\varepsilon^{i}\delta\varepsilon^{i} L_{i} A = 0. \qquad \text{(B.17)}
$$

Thus, one can obtain the strain-balanced condition for (0001)-oriented wurtzite-based material system as

$$\sum_{i=2}^{N}\left(C_{11}^{(i)}+C_{13}^{(i)}-2\frac{C_{13}^{(i)2}}{C_{11}^{(i)}}\right)\frac{L_i\varepsilon^i}{a_i}=0. \tag{B.18}$$

In addition, if the materials and thicknesses of the epitaxial layers are predetermined, the lattice constant of the substrate which satisfies the strain-balanced condition is

$$a_0=\frac{\sum_{i=1}^{N}\left(C_{11}^{(i)}+C_{13}^{(i)}-2\frac{C_{13}^{(i)2}}{C_{11}^{(i)}}\right)L_i/a_i}{\sum_{i=1}^{N}\left(C_{11}^{(i)}+C_{13}^{(i)}-2\frac{C_{13}^{(i)2}}{C_{11}^{(i)}}\right)L_i/a_i^2}. \tag{B.19}$$

Bibliography

[1] P. Thijs, L. Tiemeijer, P. Kuindersma, J. Binsma, and T. Van Dongen, “High-performance 1.5 μm wavelength InGaAs-InGaAsP strained quantum well lasers and amplifiers,” IEEE J. Quantum Electron. **27**, 1426 –1439 (1991).

[2] D. K. Nayak, J. C. S. Woo, J. S. Park, K. L. Wang, and K. P. MacWilliams, “High-mobility p-channel metal-oxide-semiconductor field-effect transistor on strained Si,” Appl. Phys. Lett. **62**, 2853–2855 (1993).

[3] K. Rim, J. Hoyt, and J. Gibbons, “Fabrication and analysis of deep submicron strained-Si n-MOSFET’s,” IEEE Trans. Electron Devices, **47**, 1406 –1415 (2000).

[4] J. Matthews and A. Blakeslee, “Defects in epitaxial multilayers: III. preparation of almost perfect multilayers,” J. Cryst. Growth **32**, 265 – 273 (1976).

[5] E. Kasper, H. Kibbel, H. Jorke, H. Brugger, E. Friess, and G. Abstreiter, “Symmetrically strained Si/Ge superlattices on Si substrates,” Phys. Rev. B **38**, 3599–3601 (1988).

[6] D. C. Houghton, “Strain relaxation kinetics in $\mathrm{Si}_{1-x}\mathrm{Ge}_x$/Si heterostructures,” J. Appl. Phys. **70**, 2136–2151 (1991).

[7] V. D. Jovanović, Z. Ikonić, D. Indjin, P. Harrison, V. Milanović, and R. A. Soref, “Designing strain-balanced GaN/AlGaN quantum well structures: Application to intersubband devices at 1.3 and 1.55 μm wavelengths,” J. Appl. Phys. **93**, 3194–3197 (2003).

[8] N. J. Ekins-Daukes, K. Kawaguchi, and J. Zhang, “Strain-balanced criteria for multiple quantum well structures and its signature in X-ray rocking curves,” Cryst. Growth Design **2**, 287–292 (2002).

[9] H. Reismann and P. S. Pawlik, *Elasticity Theory and Applications* (John Wiley, New York, 1980).

[10] I. S. Sokolnikoff, *Mathematical Theory of Elasticity* (McGraw-Hill, New York, 1956).

[11] M. H. Sadd, *Elasticity: Theory, Applications, and Numerics* (Elsevier, Burlington, 2005).